Dynamic characterization of sandwich beams using a LASER Vibrometer

Simão Pedro Lima Carvalho

Thesis to obtain the Master of Science Degree in

Aerospace Engineering

Supervisor(s): Prof. Marco Gherlone
Prof. Fernando José Parracho Lau
Dr. Matteo Sorrenti

December 2023

Dedicated to my parents, Elisabete and Joaquim, my grandparents Silvino and Rosa, and my girlfriend Leonor.

Declaration

I declare that this document is an original work of my own authorship and that it fulfills all the requirements of the Code of Conduct and Good Practices of the Politecnico di Torino.

Acknowledgments

First and foremost, I would like to express my gratitude to Professor Marco Gherlone, Professor Fernando Lau and Engineer Matteo Sorrenti for their invaluable guidance and support in the development of this work.

I also want to emphasize the crucial role played by my parents, sister, and maternal grandparents throughout my journey. Without their support and contributions to my education, completing this journey would have been impossible.

Furthermore, I'd like to extend my thanks to my aunts and uncles, with special mention of my aunt Silvia, my first teacher, and my aunt Amélia, who not only ignited my passion for mathematics but also provided unwavering support throughout my journey.

I am also grateful to Teacher Susana and her husband, Pedro, who were invaluable contributors to my success at various stages of this journey. Moreover, I would like to express my appreciation to my cousins André and Mafalda, who not only welcomed me into their home, providing me with the opportunity to study at Instituto Superior Técnico, but also offered valuable advice and support as I embarked on my journey as a university student.

Additionally, I want to underscore the role of all my friends in completing this journey. I would like to begin by expressing my gratitude to my longtime friends Eduardo, Leo, and Paulo, who have been a part of my life for many years. I'm also thankful to my friends Gonçalo, Miguel, and Pedro, who provided significant support throughout my time at Instituto Superior Técnico. Special thanks go to my friends Filippo and Davide, without whom it would have been impossible to complete my final year at Politecnico di Torino.

Last but certainly not least, I want to extend a special thank you to my girlfriend, Leonor, whom I met during my second year at Instituto Superior Técnico and who also played a crucial role in the successful completion of this journey. Therefore, I hope you can tolerate me for many more years.

Abstract

Nel mondo odierno, basandosi sulle conoscenze acquisite finora, si sa che le risorse sono limitate e la loro sfruttamento talvolta non è giustificato, poiché il bilancio complessivo tra prodotto finale e materia prima, che comprende tutti gli aspetti del processo, non è rispettato, causando così danni significativi all'ambiente [1]. Di conseguenza, c'è stata una crescente preoccupazione nella comunità scientifica nel trovare soluzioni che ottimizzino le risorse esistenti.

In effetti, grazie ai significativi progressi tecnologici che si sono verificati nel secolo scorso, gli scienziati e gli ingegneri hanno scoperto di poter creare materiali con caratteristiche desiderabili, che hanno chiamato materiali compositi [2]. In realtà, la scoperta di tali materiali risale al tempo degli Egizi, che utilizzavano un tipo di malta e mattoni che combinavano argilla rinforzata con paglia per costruire le loro piramidi. Tuttavia, lo sviluppo dei materiali compositi ha preso slancio dagli anni '30, in particolare durante la Seconda Guerra Mondiale, principalmente nelle applicazioni militari, come la produzione di parti per aeromobili.

Inoltre, con il progresso tecnologico raggiunto, è diventato possibile costruire strumenti sempre più precisi e sicuri, consentendo così studi sperimentali più realistici e affidabili. È, infatti, la capacità umana di applicare la conoscenza scientifica combinata con nuove scoperte a "alimentare" il progresso scientifico e portare alla creazione di strumenti e oggetti in grado di soddisfare meglio le proprie esigenze. In realtà, si tratta di un ciclo iterativo di processi, ma la loro spinta al progresso consente al punto di partenza di ciascuna fase di diventare il punto di arrivo della fase precedente.

Alla luce dell'incremento dell'accuratezza degli studi di analisi modale condotti in precedenza con accelerometri [3], la tesi attuale ha cercato di effettuare la caratterizzazione dinamica delle travi sandwich (facce in alluminio e cuore in schiuma di polimero) utilizzando un **vibrometro LASER**.

Per confrontare e valutare se i risultati ottenuti dalle misurazioni della risposta del **vibrometro LASER** sono effettivamente accurati, è stato condotto anche una studio numerico. Pertanto, la tesi sviluppata è stata suddivisa in due parti distinte: una parte sperimentale, in cui una trave con condizioni di bordo libere è stata dinamicamente eccitata utilizzando uno **Shaker** e un **Hammer**; e una parte numerica, in cui le stesse condizioni sono state introdotte nel software **Patran/Nastran** per simulare ciò che accade nella parte sperimentale e confrontare i risultati.

Infine, dopo aver ottenuto le prime frequenze naturali e le relative forme modali, verranno tratte delle conclusioni e saranno analizzate le possibilità per lavori futuri.

Parole chiave: Structural Analysis, Modal Testing, LDV, Resonance, FEM.

Abstract

In today's world, based on the knowledge acquired so far, it is known that resources are limited and their exploitation is sometimes not justified, as the overall final product-raw material balance, encompassing all aspects of the process, does not compensate, thereby causing significant damage to the environment [1]. As a result, there has been an increasing concern among the scientific community to find solutions that optimize existing resources.

In fact, through the significant technological advancements witnessed in the last century, scientists and engineers have discovered that they could create materials with more desirable characteristics, which they termed composite materials [2]. In truth, the discovery of such materials dates back to the time of the Egyptians, who used a type of mortar and brick that combined reinforced clay with straw to build their pyramids. However, the development of composite materials gained momentum from the 1930s, especially during World War II, primarily in military applications, such as aircraft parts manufacturing.

Furthermore, with the technological progress achieved, it has become possible to build increasingly precise and secure instruments, thereby enabling more realistic and reliable experimental studies. Indeed, it is the human capacity to apply scientific knowledge combined with new discoveries that ”fuels” scientific progress and leads to the creation of tools and objects capable of better satisfying their needs. In reality, this is an iterative cycle of processes, but their drive for progress allows the starting point of each stage to become the endpoint of the previous one.

In light of the improved accuracy of previous modal analysis studies conducted with accelerometers [3], the current thesis sought to perform the dynamic characterization of sandwich beams (aluminium faces and polymer foam core) using a **LASER vibrometer**.

To compare and evaluate whether the results obtained from the **LASER vibrometer** response measurement are indeed accurate, a numerical study was also conducted. Thus, the developed thesis was divided into two distinct parts: an experimental part, where a beam under free boundary conditions was dynamically excited using a **Shaker** and a **Hammer**; and a numerical part, where the same conditions were introduced in the **Patran/Nastran software** to simulate what occurs in the experimental part and compare the results.

Finally, after obtaining the first natural frequencies and corresponding vibration modes, conclusions will be drawn, and possibilities for future work will be extrapolated.

Keywords: Structural Analysis, Modal Testing, LDV, Resonance, FEM.

Contents

List of Tables

List of Figures

Nomenclature

Greek symbols

β	Frequency ratio
γ^2	Coherence function
Δ	Damping dissipation function
ζ	Damping factor
ρ	Mass density
υ	Poisson's ratio
$[\phi]$	Modal matrix
$\{\phi\}$	Eigenvectors
φ	Phase delay
$\left[\Omega^2\right]$	Diagonal matrix with natural frequencies
ω	Angular frequency
ω_d	Angular frequency of damped vibration
ω_n	Natural angular frequency

Roman symbols

$[C]$	Damping matrix
C	Damping
c	Speed of light
c_c	Critical damping
$[D_M]$	Diagonal mass matrix
$[D_k]$	Diagonal stiffness matrix
D	Dynamic Amplification factor

dif	Differences between frequencies
D_{max}	Maximum Dynamic Amplification Value
E	Young module
E_k	Kinetic energy
E_p	Potencial energy
E_{TOT}	Eletric field
F	External force
f	Frenquency
f_d	Frequency of damped vibration
f_n	Natural frequency
G	Shear modulus
H	Transfer function
$[I]$	Identity matrix
I	Incident radiation
Im	Imaginary part of a number
$[K]$	Stiffness matrix
K	Stiffness
L_e	Work done by external forces
$[M]$	Mass matrix
m	Mass
N	Noise function
Re	Real part of a number
T	Period
u	Displacement vector
$\dot{u}$	Velocity vector
$\ddot{u}$	Acceleration vector
u_f	Homogeneous solution
u_p	Particular solution

Subscripts

x, y, z	Cartesian components
$\nu, \dot{\nu}, \ddot{\nu}$	Modal components
j	Imaginary part
EXP	Experimental frequencies
FE	Numerical model frequencies
XY	Cross
XX	Input
YY	Output

Supercripts

*	Conjugate Complex
-1	Inverse
T	Transpose

Glossary

LT	Laplace Transform
LDV	Laser Doppler Vibrometer
FE	Finite Element
FEA	Finite Element Analysis
FEM	Finite Element Model
FT	Fourier Transform
FRF	Frequency Response Function
MAC	Modal Assurance Criterion
MDOF	Multiple degrees of freedom
PBS	Polarizing beam splitter
SDOF	Single degree of freedom
SLDV	Scanning Laser Doppler Vibrometer
SNR	Signal-to-Noise Ratio

Chapter 1

Introduction

1.1 Motivation

Throughout generations, Humanity has witnessed technological advancement that has been driven by the need to satisfy its various requirements. However, as technological demands increased, particularly in the aerospace and automotive industries, conventional materials started to exhibit limitations in terms of performance. Consequently, in order to address these needs, researchers realized that by combining different materials, they could achieve a final product with optimized properties [1].

Based on this premise, many studies have been conducted in the field of composite materials to understand how certain combinations of materials can result in a material that encompasses the best qualities of each component involved in the process [2, 4, 5].

One of the industries that has greatly benefited from the technological advancements in this field of study is the aerospace industry [6]. A notable example is the Boeing 787 aircraft, which began commercial operations in 2007. Approximately half of its total weight is made up of composite materials, and it is about 20% lighter than the earlier Boeing 777 model, which was introduced in 1993 with only 20% of its total weight as composite materials [7, 8]. This demonstrates the increasing utilization of these materials by the industry due to their ability to develop lighter and highly durable structures. As a result, this contributes to reduced energy consumption, improved efficiency, and sustainability across various industries [6, 9].

That being said, this work aimed to perform experimental modal analyses under a Free-Free boundary condition using less conventional tools, such as a Laser Doppler Vibrometer (LDV), for conducting these experimental activities [3, 10–13]. Therefore, given the observed importance of composite materials, the focus of this analysis was on the study of composite materials. Consequently, four composite beams from the Laboratory of the Department of Mechanical and Aerospace Engineering at Politecnico di Torino were selected for this work. All of these beams had 7075 aluminium faces and a core of polymer foam WF-110. However, the thickness of these materials varied from beam to beam, which also led to variations in stiffness and distributed mass for each of these beams. Consequently, this variation in stiffness resulted in different resonant frequencies when external forces were applied using a Shaker, as will be observed.

It is worth noting that when the frequency of external excitation coincides with one of the natural frequencies of a structure, it can lead to vibration amplification, potentially causing structural failures, ruptures, or even collapse, as seen in the example of the Tacoma Narrows Bridge collapse in 1940 [14]. This phenomenon is known as resonance and is more likely to occur when a structure is subjected to external forces like wind, earthquakes, turbulence, or other dynamic loads. Therefore, it is essential to predict the natural frequencies of certain structures and their vibration modes in order to prevent potential failures by avoiding them under service and ensure the safety, integrity, and durability of structures over time [15, 16].

1.2 Topic Overview

The main topic addressed in this work is experimental modal testing. To ensure a good understanding of this subject, it is important to define this concept and explain how modal testing will be applied in this specific work.

Hence, modal testing serves as a fundamental tool for constructing reliable models that capture the dynamic behaviour exhibited by structures [17]. By conducting these types of experimental activities, it becomes possible to determine specific modal characteristics of each structure, such as natural frequencies, modal shapes, and damping. Knowledge of these characteristics will subsequently enable predictions of structural behaviour under dynamic loads [18, 19].

It is evident that in the aerospace industry, these tests play a crucial role, as aircraft are susceptible to significant dynamic loads, such as turbulence. Therefore, to ensure the safety of these vehicles when exposed to such phenomena, it is necessary to conduct modal tests on all their components beforehand [20, 21].

Having said that it's worth noting that before conducting any modal test, it is customary to create a preliminary Finite Element Model (FEM) that accurately represents the structure under investigation [22, 23]. This practice stems from the fact that conducting a numerical analysis allows for an initial estimation of the dynamic behaviour of the structure under study, providing valuable insights for the modal test. With this estimation, it becomes possible to identify the optimal locations for excitation and measurement within the structure, predict the natural frequencies to be obtained in the modal test, reduce resource consumption, and, early on, determine whether the structure will meet the necessary requirements [23, 24]. Subsequently, following the execution of the modal test, the quality of these numerical models should be evaluated by comparing them to the experimentally obtained results. This evaluation will determine if the models are indeed representative of the realities under study. All these procedures were implemented in this work and will be comprehensively discussed further [18].

That being said, to perform a modal analysis engineers frequently employ methods that require measuring the structure's response using accelerometers [3, 10–13]. However, it is essential to be aware of potential errors associated with this methodology. The introduction of these devices imposes a small mass on the structure under examination, which can significantly affect the characteristics of some structures. Consequently, a limited number of accelerometers can be applied to structures, as the additional mass becomes considerable beyond a certain number. Furthermore, improper installation of accelerometers, such as small positioning or fixation errors, may result in imprecise measurements. Additionally, these sensors are more susceptible to capturing noise and interference, potentially impacting and distorting the analysis results [18, 25].

To enhance the precision and reliability of results, technological advancements have given rise to an alternative method utilizing LDV for data acquisition [26, 27]. This approach involves directing a laser beam at the structure's surface and capturing the reflected light with a sensor. Subsequently, the technology measures the frequency shift of the reflected light, which is then used to determine the structure's modal characteristics. Therefore, instead of using traditional piezoelectric accelerometers, an LDV was employed in this work to perform the experimental modal tests.

1.3 Objectives and Deliverables

As previously mentioned, one of the main objectives of this work is to conduct modal testing on four beams under **Free-free boundary conditions**. However, given that suspending a beam in the air without any support is not feasible, a solution that approximates the free-condition scenario had to be devised. For this purpose, a configuration with metal beams and elastic supports was conceptualized and subsequently used, as will be observed.

As previously mentioned, another objective is to create FEM models for each of the four beams that accurately predict the dynamic behaviour of the structures under study. Despite the availability of various software, these numerical models were developed and executed using the Patran/Nastran software. This choice was made because of the ease with which Politecnico di Torino (the university where this experimental activity took place) could obtain a license for this software. Subsequently, using MATLAB programs created for the purpose of collecting and analyzing all data from both numerical and experimental models (see Appendices A and B), the level of correlation between these two models was determined, allowing for an assessment of the validity of the numerical models.

Finally, another aim of this work was to evaluate the LDV technology in conducting modal testing. As a result, the potential advantages and disadvantages of this technology in carrying out these activities will be discussed further.

That being said, the detailed objectives of this study are as follows:

- Develop FEM models for the four beams;
- Obtain the numerical results from the FEM models;
- Devise a mechanism that best approximates the free-condition scenario for the beams;
- Determine the laser measurement positions to accurately represent the modal shapes;
- Assess whether the use of LDV technology can provide significant advantages compared to more conventional solutions for modal testing;

- Acquire the experimental frequencies and modal shapes;
- Create programs to collect and analyze all obtained data to determine the level of correlation between the two models;
- Compare the experimental results with the numerical results and assess their similarity;
- Verify if it is possible to validate the previously developed FEM models.

1.4 Thesis Outline

The structure of the thesis has been divided into 8 chapters, ensuring coherence and a logical flow of the topics to be addressed throughout the work.

Chapter 1 serves as a brief introduction, providing context to the problem under study and outlining the objectives and steps to be analyzed throughout the research.

In Chapter 2, essential theoretical concepts about the dynamics of discrete systems will be discussed to enhance the understanding of the subsequent analyses.

Chapter 3 will present a literature review and some fundamental concepts regarding the evolution and application of the Finite Element Method, allowing the reader to become familiar with the concepts related to this topic.

Chapter 4 will delve into the numerical aspect, explaining how the numerical model was obtained. It will cover all parameters introduced into the Patran/Nastran software and the relevant steps that were applied.

Chapter 5 will cover all concepts related to modal testing in the first part, while in the second part, the operation of the LDV and its advantages will be explained, along with the strategies that can be applied to obtain accurate results.

Chapter 6 will focus on the experimental procedure used, including the selection of the measurement points configuration, the instruments used, and the entire experimental setup.

Chapter 7 will present the experimental results obtained and compare them with the previously acquired numerical results.

Finally, in Chapter 8, a conclusion will be drawn regarding the achievements of this work, and suggestions for future work will be proposed.

Chapter 2

Dynamics of discrete systems

In this chapter, the essential theoretical foundations of the dynamics of discrete systems are covered for a thorough understanding of this work. The exploration begins with the presentation of basic concepts in vibration theory. Following this introduction, an examination of the various possibilities that a Single Degree of Freedom (SDOF) system can assume is conducted. Upon gaining insight into the functioning of such systems, the focus shifts towards the transition from a time-domain response to a frequency-domain response – a form of response widely employed in this field of study [28]. With these topics addressed, the study of systems with multiple degrees of freedom (MDOF) is introduced, revealing increased complexity in their analysis.

2.1 Basic concepts of vibration theory

Firstly, it is important to begin by defining the concept of vibration. Vibration (or oscillation) refers to any motion within a certain time interval, such as the simple swinging of a pendulum. Furthermore, it should be noted that the theory of vibrations extends beyond the study of body movements; it also encompasses the examination of the forces associated with these movements.

Typically, the representation of a vibratory system includes at least one device capable of storing potential energy and another device capable of storing kinetic energy. When only these two elements are represented, energy conservation is assumed. To account for the dissipation that occurs in reality, often represented by a damper (as will be used in the cases studied), it is added to the system. Thus, vibratory systems can be classified according to various parameters, such as [29, 30]:

- **Undamped or Damped:** If the energy transformation process is conservative, meaning that energy losses can be considered negligible, the system is classified as **Undamped**, and no devices capable of dissipating energy are represented. For cases where it is too unrealistic to assume that the system does not dissipate energy during the transformation process, the system is characterized as **Damped**, and typically one or more dampers are introduced in its representation;
- **Free or Forced: Free systems** consist of systems that, after an initial disturbance, will vibrate on their own, meaning they will continue to vibrate without the action of any external force after that

first impact. On the other hand, **Forced systems** are systems that are continuously subjected to an external force;

- **Deterministic or Random:** As the name suggests, **Deterministic systems**, unlike **Random systems**, are subject to an external force that acts on the system under study and is known for a certain interval of time. However, due to the difficulty of studying **Random vibratory systems**, such as turbulence, sometimes from data collection, a statistical regularity can be found for a certain interval of time. Consequently, for these cases, it is possible to simplify the study of these systems by approximating them as **Deterministic systems**.

Finally, it is also important to mention that harmonic functions are typically used for representing vibrations, especially for deterministic systems (which are the subject of study in this work). This approach is widely used because it not only allows obtaining simple numerical expressions but also proves to be quite useful in obtaining frequency domain responses by applying the Fourier transform [31].

Thus, any harmonic function is characterized by the following parameters:

- **Period:** represented by the letter T, it is the time required to complete one full oscillation;
- **Frequency:** represented by the letter f, it is the inverse of the **Period**, and physically represents the number of oscillations that a particular harmonic function completes in one second;
- **Angular frequency:** represented by the letter ω, it is a vector quantity that measures the speed at which a body moves along a circular path and is widely used for harmonic functions. It can be calculated by multiplying $2 * \pi$ by f ($\omega = 2\pi \cdot f$).

Given this, it is important to note that harmonic functions can also be interpreted, as shown in Figure 2.1, as the result of adding two vectors: one corresponding to the vertical projection in the imaginary plane and another corresponding to the horizontal projection. It is important to note that the system can be expressed, as you will see in Equations 2.1, 2.2, and 2.3, using only an imaginary exponential (the imaginary part in this work will be denoted by the letter j).

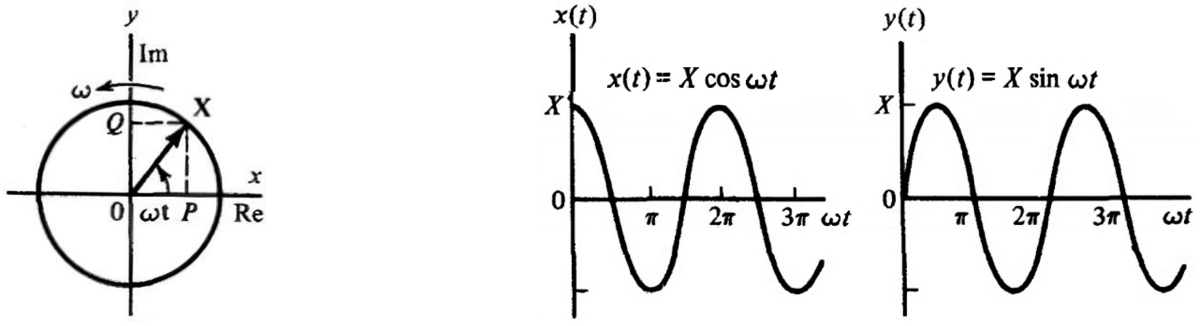

(a) Vectorial representation

(b) Harmonic motions

Figure 2.1: Harmonis motions represented by rotating vector [31].

Taking this into account, and considering X as any amplitude, the following equations can be written for displacement (u), velocity ($\dot{u}$), and acceleration ($\ddot{u}$), respectively:

$$u = X\cos(\omega_n t) + jX\sin(\omega_n t) = Xe^{j\omega_n t} \tag{2.1}$$

$$\dot{u} = j\omega_n X e^{j\omega_n t} = j\omega_n u \tag{2.2}$$

$$\ddot{u} = -\omega_n^2 X e^{j\omega_n t} = -\omega_n^2 u \tag{2.3}$$

The Figure 2.2 illustrates the result obtained from the previous equations:

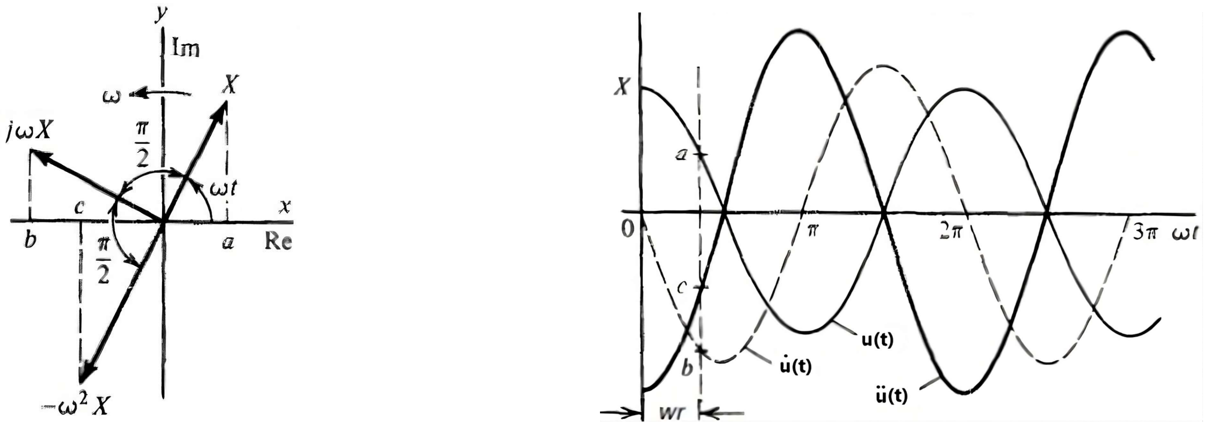

(a) Vectorial representation (b) Harmonic motions

Figure 2.2: Displacement. velocity and acceleration vectors [31].

2.2 SDOF systems

As previously mentioned, the analysis will commence with SDOF systems, which are systems that only require one coordinate to fully describe all positions of their motion [29]. Although these systems may not represent the beams that will be the subject of study in this work, they provide a solid understanding of the basic concepts of structural dynamics. Therefore, as illustrated in Figure 2.3, an SDOF system is typically represented by a mass, a spring and a damper.

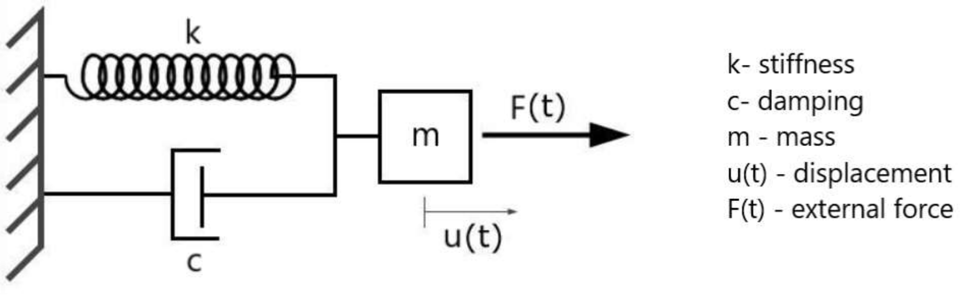

Figure 2.3: Spring-Mass-Damper System [32].

It should be noted that for the sake of simplification in certain equations, $u(t)$ (displacement) and

$F(t)$ (external force) will be represented simply as u and F, respectively. That being said, applying the Lagrange Equation,

$$\frac{d}{dt}\left(\frac{\partial E_k}{\partial \dot{u}_i}\right)+\left(\frac{\partial \Delta}{\partial \dot{u}_i}\right)+\left(\frac{\partial E_p}{\partial u_i}\right)=\left(\frac{\partial L_e}{\partial u_i}\right) \tag{2.4}$$

where,

- E_k represents the kinetic energy, defined by the following expression:

$$E_k=\frac{1}{2}m\dot{u}^2 \tag{2.5}$$

- Δ represents the damping dissipation function, defined by the following expression:

$$\Delta=\frac{1}{2}c\dot{u}^2 \tag{2.6}$$

- E_p represents the potential energy, defined by the following expression:

$$E_p=\frac{1}{2}ku^2 \tag{2.7}$$

- L_e represents the work done by external forces, defined by the following expression:

$$L_e=Fu \tag{2.8}$$

Applying these expressions yields the following equation of motion:

$$m\ddot{u}+c\dot{u}+ku=F \Leftrightarrow \ddot{u}+\frac{c}{m}\dot{u}+\frac{k}{m}u=\frac{F}{m} \tag{2.9}$$

With this in mind, it becomes evident that, based on Equation 2.9, various cases can be studied:

Table 2.1: Different cases for SDOF systems.

	$c=0$	$c\neq 0$
$F=0$	Free vibrations for undamped systems **(first case)**	Free vibrations for damped systems **(second case)**
$F\neq 0$	Force vibrations for undamped systems **(fourth case)**	Force vibrations for damped systems **(third case)**

Considering Table 2.2, a separate study will now be conducted for each of these different cases.

2.2.1 Free vibrations for undamped systems

It is observed that for the **first case** in Table 2.2, Equation 2.9 can be simplified as follows:

$$\ddot{u} + \frac{k}{m}u = 0 \tag{2.10}$$

Hence, recalling Equation 2.3, the following is obtained:

$$\omega_n^2 = \frac{k}{m} \tag{2.11}$$

Therefore, assuming that the solution to Equation 2.10 (where M represents any constant) will be of the following form:

$$u(t) = Me^{\omega t} \tag{2.12}$$

Applying Equation 2.12 to the Equation of motion 2.10, the following result is obtained:

$$\omega^2 = -\omega_n^2 \Leftrightarrow \omega = \pm j\omega_n \tag{2.13}$$

Thus, it can be observed that for this case, in addition to the conservation of energy, $f = f_n$, and its solution can be written as follows:

$$u(t) = Me^{\pm j\omega_n} \tag{2.14}$$

2.2.2 Free vibrations for damped systems

For the **second case** in Table 2.2, Equation 2.9 can be simplified to the following homogeneous differential equation:

$$\ddot{u} + \frac{c}{m}\dot{u} + \frac{k}{m}u = 0 \tag{2.15}$$

From Equation 2.15 and assuming the solution in Equation 2.12, the following is derived:

$$\omega_{1,2} = -\frac{c}{2m} \pm \sqrt{\left(\frac{c}{2m}\right)^2 - \frac{k}{m}} \tag{2.16}$$

In addition, it is important to define the **Critical Damping**, c_c. This constant takes the value of the damping constant c that makes the root of Equation 2.16 equal to zero, i.e.:

$$c_c = 2m\sqrt{\frac{k}{m}} = 2m\omega_n \tag{2.17}$$

The **Damping factor**, ζ, is equal to the ratio of c to c_c. Thus, it is expressed as:

$$\frac{c}{m} = \frac{c}{c_c} \cdot \frac{c_c}{m} = 2\zeta\omega_n \tag{2.18}$$

Consequently, applying Equation 2.18, the solution to Equation 2.12 takes the following expression:

$$u(t) = M_1 e^{\left(-\zeta\omega_n + \omega_n\sqrt{\zeta^2-1}\right)t} + M_2 e^{\left(-\zeta\omega_n - \omega_n\sqrt{\zeta^2-1}\right)t} \tag{2.19}$$

From the previous equation, it is evident that, as expected, for the case of $\zeta = 0$, the solution obtained would be the same as the one obtained in 2.14, i.e., the undamped system **first case**. However, for the case $\zeta \neq 0$, three different scenarios arise.

To understand each of these cases, it is first necessary to define ω_d, which corresponds to the **angular frequency of damped vibration**, i.e., the pseudo-angular frequency of a system with damping. Thus, ω_d takes the following expression:

$$\omega_d = \omega_n\sqrt{\zeta^2 - 1} \tag{2.20}$$

Note that, with the help of Figure 2.1, ω_d represents the imaginary part. Therefore, for the case $0 < \zeta < 1$, ω_d will always be less than ω_n. However, for cases where $\zeta \geq 1$, the system will no longer oscillate around an equilibrium configuration as ω_d ceases to be an imaginary number. It is also noted that for the case of $\zeta = 1$, the system will have critical damping. Consequently, the system will reach the equilibrium configuration more quickly, as for situations where $\zeta > 1$, $\omega_d > \omega_n$.

Since ω_d is greater than ω_n, the roots of Equation 2.19 will be located on both sides of the root for the $\zeta = 1$ situation, as depicted in Figure 2.4, resulting in a slower approach to the equilibrium configuration. Physically, this case can be interpreted as if the object were immersed in a viscous fluid, thus experiencing resistance to motion. All cases for different values of ζ are covered in Figure 2.5.

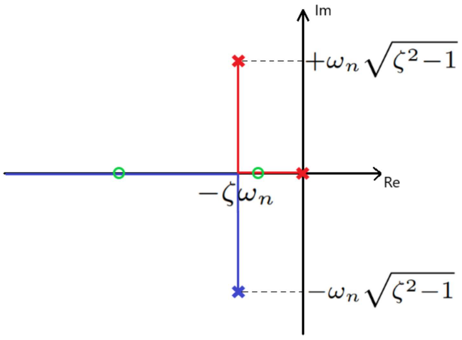

Figure 2.4: Representation of the possible roots of Equation 2.19.

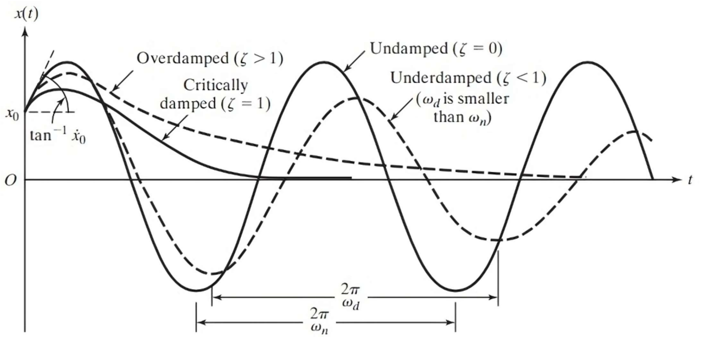

Figure 2.5: Comparison of motions with different types of damping [29].

2.2.3 Force vibrations for damped systems

Now, for the **third case** in Table 2.2, Equation 2.9 corresponds to the simplified version. However, since the differential equation in question is non-homogeneous, its solution will be given by the sum of a solution to the associated homogeneous equation, $u_f(t)$, and a particular solution to the complete equation, $u_p(t)$ [33].

$$u(t) = u_f(t) + u_p(t) \tag{2.21}$$

Thus, the following system of equations can be represented:

$$\begin{cases} \ddot{u_f} + \frac{c}{m}\dot{u_f} + \frac{k}{m}u_f = 0 \\ \ddot{u_p} + \frac{c}{m}\dot{u_p} + \frac{k}{m}u_p = \frac{F}{m} \end{cases} \tag{2.22}$$

By observing the System of Equations 2.22, it becomes evident that $u_f(t)$ will take the form of Equation 2.19 (the equation deduced for the **second case**), as it is a homogeneous equation. However, since for this **third case**, $u(t)$ results from the sum of two terms, the constants M_1 and M_2 will necessarily be different because the initial conditions are applied to the system as a whole:

$$\begin{cases} U_0 = u_f(0) + u_p(0) \\ \dot{U}_0 = \dot{u}_f(0) + \dot{u}_p(0) \end{cases} \tag{2.23}$$

For $u_p(t)$, it is essential to define $F(t)$ as the response is associated with the force acting on any system. Assuming that $F(t)$ behaves as a periodic function (see Equation 2.24) and that F_0 is a constant, it can be written as a linear combination of harmonic functions.

$$F(t) = F_0 e^{j\omega t} \tag{2.24}$$

It should be noted that the ω in Equation 2.24 corresponds to the angular frequency of the force itself and is thus different from ω_n and ω_d. Therefore, assuming that $F(t)$ is described by a harmonic function, the response (in this case $u_p(t)$) must also be written as a linear combination of harmonic functions, where its angular frequency will necessarily be the same as that of the force, but with a phase delay φ (see Equation 2.25).

$$u_p(t) = u_0 e^{j\omega t + \varphi} \tag{2.25}$$

Hence, by substituting Equations 2.24 and 2.25 into the equation for $u_p(t)$ in System 2.22 and knowing that β corresponds to the **Frequency Ratio** ($\beta = \frac{\omega}{\omega_n}$), the Equation 2.26 can be deduced::

$$u_0 e^{-j\varphi} = \frac{F_0}{k} \cdot \frac{(\beta^2) - j2\zeta\beta}{(1-\beta^2)^2 + 4\zeta^2\beta^2} \tag{2.26}$$

Thus, it is expressed as follows:

$$u_0 = \sqrt{Re^2 + Im^2} = \frac{F_0}{k} \cdot \frac{1}{\sqrt{(1-\beta^2)^2 - 4\zeta^2\beta^2}} \tag{2.27}$$

$$\varphi = -\arctan\frac{Im}{Re} = \arctan\frac{2\zeta\beta}{1-\beta^2} \tag{2.28}$$

After determining the expressions for the constants in the solution of $u_p(t)$ (Equation 2.25), the following equation can be written:

$$-\omega^2 m u_0 e^{j(\omega t - \varphi)} + cj\omega u_0 e^{j(\omega t - \varphi)} + k u_0 e^{j(\omega t - \varphi)} = F_0 e^{j\omega t} \tag{2.29}$$

This simplification is useful as it allows for the geometric interpretation shown in Figure 2.6 regarding the particular solution $u_p(t)$. Here, it is observable that the initial term in Equation 2.29 corresponds to the inertial force, the second term to the damping force, the third term to the elastic force and the last term to the external force.

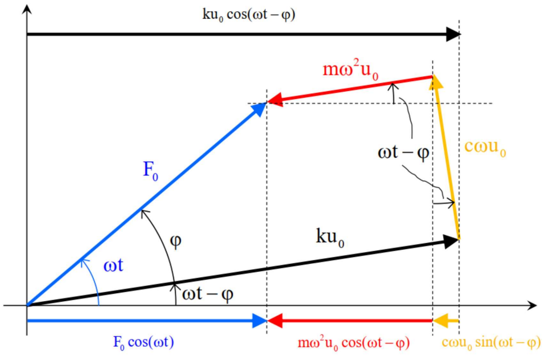

Figure 2.6: Geometric representation of Equation 2.29 [22].

With that said, it is now important to introduce the concept of **Dynamic Amplification Factor**, $D(t)$. This factor is highly relevant as it allows us to assess how much the dynamic response is amplified compared to the static response, $u_{st}(t)$, which represents the response when the system under study does not need to vibrate to adapt. Thus, it is expressed as:

$$D(t) = \frac{u_p(t)}{u_{st}(t)} = \frac{e^{j(\omega t - \varphi)}}{\sqrt{\left(1-\beta^2\right)^2 - 4\zeta^2\beta^2}} \tag{2.30}$$

Once again, it should be emphasized that the dynamic response $u_p(t)$ will be periodic, whereas $u_{st}(t)$ will represent a static response. For this reason, to calculate the maximum value of $D(t)$, it is only necessary to determine when $u_p(t)$ is at its maximum. Thus, D_{max} takes the following algebraic expression:

$$D_{max} = \frac{1}{\sqrt{\left(1-\beta^2\right)^2 - 4\zeta^2\beta^2}} \tag{2.31}$$

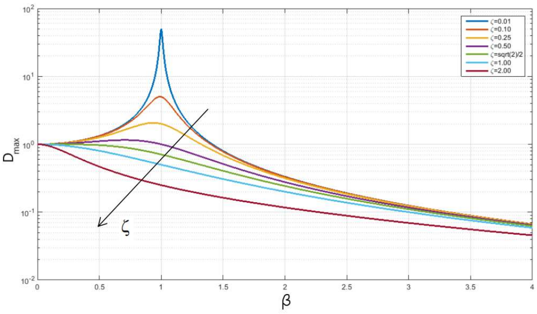

Figure 2.7: Variation of D_{max} with β for different values of ζ [22].

From Equation 2.31 and Figure 2.7, it is important to note that for $\zeta \geq \frac{\sqrt{2}}{2}$, the function D_{max} will not have any absolute maximum value. However, for values of $\zeta < \frac{\sqrt{2}}{2}$, the function D_{max} will always have an absolute maximum value occurring at $\beta = \sqrt{1-2\zeta^2}$, which means it will be very close to $\beta = 1$. As ζ increases, the value of β at which the peak in D_{max} occurs decreases, as confirmed by Figure 2.7.

Indeed, from Equation 2.28, it can be observed that for low values of β, the angle φ will take values very close to zero for any ζ. In this case, by adjusting the value of φ in Figure 2.8, it is evident that the response will be dominated by the elastic force, meaning the contributions of mass and damping are negligible compared to the contribution of the spring.

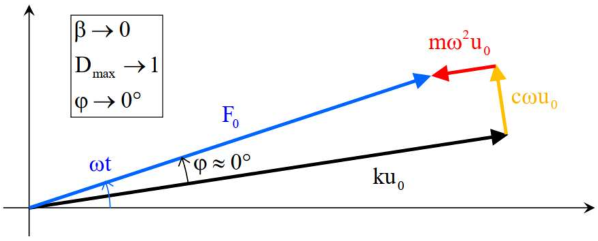

Figure 2.8: Geometric representation of Equation 2.29 as $\beta \to 0$ [22].

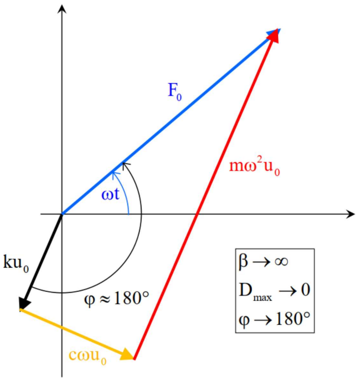

Figure 2.9: Geometric representation of Equation 2.29 as $\beta \to \infty$ [22].

Exactly, for high values of β, the angle φ will take values very close to $180°$. In this case, by adjusting the value of φ in Figure 2.9, it can be observed that the response will be dominated by the inertial force, meaning the contributions of the spring and damping are negligible compared to the contribution of the mass.

Lastly, for values of β very close to 1, it can be observed from Equation 2.28 that the angle φ will take values very close to $90°$. In this case, by adjusting the value of φ in Figure 2.10, it is evident that the response will be dominated by the damping force, meaning the contributions of the spring and mass are negligible compared to the contribution of damping.

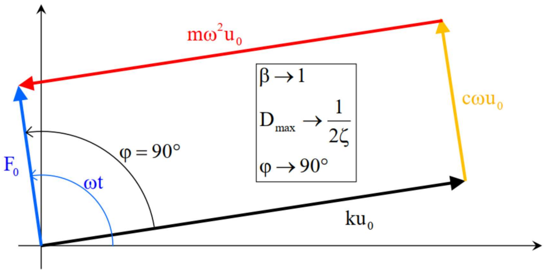

Figure 2.10: Geometric representation of Equation 2.29 as $\beta \to 1$ [22].

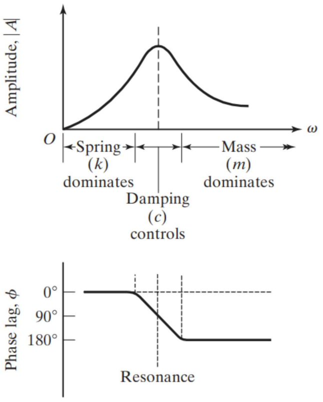

Figure 2.11: Representation of all situations for the different values of β [29].

This situation is referred to as **Resonance**, and as mentioned before, this phenomenon is particularly important when $\zeta < \frac{\sqrt{2}}{2}$, where the function D_{max} reaches its absolute maximum. In this case, the dynamic response is significantly amplified compared to the static response of the system, and as will be seen later, this situation will be the main focus of study in this work. All these situations are well represented in Figures 2.11.

2.2.4 Force vibrations for undamped systems

Finally, for the **fourth case** from Table 2.2, it is observed that this situation is quite similar to the **third case**. However, since $\zeta = 0$, the function D_{max} (as perceived from Equation 2.31) will have a vertical asymptote at $\beta = 1$. Thus, for this value of β, the function D_{max} will tend to infinity, making the system necessarily unstable in the resonance condition. It is also worth noting that the angle φ (from Equation 2.28) for this situation will be exactly $90°$.

2.3 Frequency response

In many cases, analysing the response in the time domain proves to be a very complicated task, involving significant computational costs or even being impossible to perform. To overcome this issue, the adopted strategy is to transform the time-domain response into the frequency domain. To achieve this conversion between domains, structural analysis utilizes the **Fourier Transform** (FT):

$$F(\omega) = T\left[f(t)\right] = \frac{1}{\sqrt{2\pi}} \int_{-\infty}^{+\infty} f(t) e^{-j\omega} dt \tag{2.32}$$

Indeed, the Fourier Transform (FT) is a specific case of the Laplace Transform (LT) [34], as unlike the latter, it only involves an imaginary exponential (see Equation 2.32). This detail is quite relevant because, as mentioned in Chapter 2.1, the equations related to the systems under study can be written using imaginary exponentials. For this reason, FTs hold significant importance in this field of study, as they enable the direct transformation from the time domain to the frequency domain.

It is important to note that the FT, unlike the LT, is only valid when initial conditions are zero. This detail is of particular importance in experimental analyses, as ensuring this requirement is fulfilled is necessary to obtain reliable results. Additionally, it is essential to understand that, as shown in Figures 2.12(a) and 2.12(b), a harmonic function in the time domain results in peaks at the frequencies of that harmonic function in the frequency domain and, if a Dirac delta function (a unit impulse with zero initial conditions) exists in the time domain, it will result in a horizontal line of unit value in the frequency domain [22, 35]

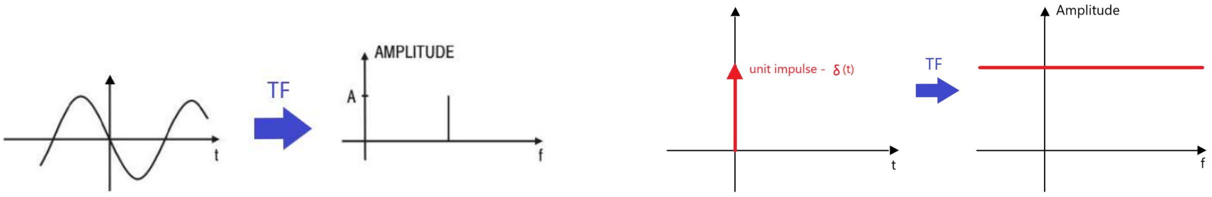

(a) Fourier transform of a Dirac Delta Function [35]

(b) Fourier transform of a Harmonic Function [36]

Figure 2.12: Examples of the application of the Fourier Transform.

After applying the FT to Equation 2.9, the ensuing result is as follows:

$$T\left[\ddot{u} + \frac{c}{m}\dot{u} + \frac{k}{m}u\right] = T\left[\frac{F}{m}\right] \Leftrightarrow T\left[\ddot{u} + 2\zeta\omega_n\dot{u} + \omega_n^2 u\right] = T\left[\frac{F}{m}\right] \Leftrightarrow$$

$$-\omega^2 T\left(u\right) + 2\zeta\omega_n j\omega T\left(u\right) + \omega_n^2 T\left(u\right) = \frac{1}{m} T\left[F\right] \tag{2.33}$$

With $T(u) = U(\omega)$ and $T[F] = F(\omega)$, the obtained expression is:

$$U(\omega) = \frac{\omega_n^2}{m\omega_n^2\left(-\omega^2 + \omega_n^2 + j2\zeta\omega_n\omega\right)} \cdot F\left(\omega\right) \tag{2.34}$$

Considering Equation 2.34, it is possible to define the **Transfer Function** ($H(\omega)$), which, through a simple multiplication with the function $F(\omega)$, allows obtaining the function corresponding to the system's response, $U(\omega)$, in the frequency domain.

$$U(\omega) = H(\omega) \cdot F(\omega) \tag{2.35}$$

Where:

$$H(\omega) = \frac{U(\omega)}{F(\omega)} = \frac{\omega_n^2}{m\omega_n^2\left(-\omega^2 + \omega_n^2 + j2\zeta\omega_n\omega\right)} = \frac{1}{k \cdot \left[\left(1-\beta^2\right) + \left(j2\zeta\beta\right)\right]} \tag{2.36}$$

Examining the function $H(\omega)$ more closely, the assumption is made that this function can be expressed in the following form:

$$H(\omega) = Me^{-j\varphi} \tag{2.37}$$

Thus, it can be observed that the amplitude M of $H(\omega)$ has the following expression:

$$M = \sqrt{\left(Re\right)^2 + \left(Im\right)^2} = \frac{1}{k} \cdot \frac{1}{k\sqrt{\left(1-\beta^2\right)^2 + 4\zeta^2\beta^2}} = \frac{1}{k} \cdot D_{max} \tag{2.38}$$

Therefore, from Equation 2.38, it is evident that the amplitude of $H(\omega)$ is directly proportional to D_{max}. It is thus proven that the frequency peaks of $H(\omega)$ will occur when the function D_{max} reaches its maximum value, in other words, as mentioned earlier, the peaks of $H(\omega)$ will occur at the resonance condition (when there is damping for $\beta \approx 1 \Rightarrow \omega_n \approx \omega$).

It should also be noted that $F(\omega)$ will have a frequency peak at ω, which corresponds to the angular frequency of the external force applied to the system. Since $U(\omega)$ is the result of the multiplication of $H(\omega)$ by $F(\omega)$, this function may exhibit two peaks, one at ω_n and another at ω, or it may have a single dominant peak when $\omega = \omega_n$.

Furthermore, regarding $H(\omega)$, it is important to mention that in many cases, especially in laboratory activities, it is more convenient to measure the response in terms of velocity or acceleration rather than displacement. In such cases, to maintain the validity of the previous expressions, one simply needs to multiply Equations 2.34 and 2.36 by $j\omega$ if the response is measured in terms of velocity or by $(j\omega)^2$ if the response is measured in terms of acceleration. It is also worth noting that $H(\omega)$ can also be referred to as the **Frequency Response Function** (FRF).

Taking all this into account, it is evident that the TF possesses three significant advantages, which are as follows:

- ω has a well-defined physical meaning, making the analysis of the studied systems more accessible;
- While in the time domain, it was necessary to solve a differential equation, using the TF only requires solving a simple multiplication, as shown in Equation 2.35;
- With the application of the TF, it is possible to estimate the values of ζ and ω_n, which are often unknown initially. Typically, in a laboratory context, the response and external force are measured in the time domain. Then, the TF is applied to the response and the applied force. Next, from Equation 2.35, the experimental values of $H(\omega)$ are obtained. Finally, by using software such as *PolyMax* [37, 38], which compares these experimental values of $H(\omega)$ with its theoretical expression (Equation 2.36), the unknowns ζ and ω_n can be estimated.

2.4 MDOF systems

SDOF systems, despite their conceptual relevance in understanding essential theoretical concepts, have limited applicability to real-world scenarios. Consequently, the study of MDOF systems is of utmost importance, as many practical systems possess multiple or even infinite degrees of freedom. The challenge with these systems lies in the fact that, unlike SDOF systems, the structures under investigation have multiple natural frequencies, requiring the examination of various resonance scenarios.

Hence, similar to SDOF systems, the equations of motion will be derived using Lagrange's equation. However, since it involves M degrees of freedom, the resulting equation will be in matrix form. Therefore, assuming that $[M]$, $[C]$, and $[K]$ represent the matrices for mass, damping, and stiffness, respectively, the following expression is obtained:

$$[M]\{\ddot{u}\} + [C]\{\dot{u}\} + [K]\{u\} = \{F\} \tag{2.39}$$

Given Equation 2.39, it is possible to analyse the different cases presented in Table 2.2 for this type of system as well. However, for reasons that will be explained, it is only useful to address the cases of **free vibrations for undamped systems**, **force vibrations for undamped systems**, and finally, **force vibrations for damped systems**, in that order.

2.4.1 Free vibrations for undamped systems

For this case, Equation 2.39 can be simplified as follows:

$$[M]\{\ddot{u}\} + [K]\{u\} = \{0\} \tag{2.40}$$

Considering that:

$$\{u\} = \{\phi\}\, e^{j\omega_n t} \tag{2.41}$$

One has:

$$\left([k]-\omega_n^2\,[M]\right)\{\phi\}\,e^{j\omega_n t}=\{0\} \tag{2.42}$$

Thus, upon analysing Equation 2.42, it is evident that it can only be solved in two ways. However, the solution $\{\phi\}=0$ is a trivial solution, meaning that it would not provide any additional information about the system under study. Therefore, since the term related to the exponential will never be zero, this problem becomes an eigenvalue problem, that is:

$$det\left([K]-\omega_n^2\,[M]\right)=0 \tag{2.43}$$

By solving the above determinant, one can obtain all the values of ω_n for the system. It is noted that some of the ω_n values may be equal to zero, as they correspond to rigid body modes, where the potential energy is zero. For example, if an airplane were being analysed, the first 6 values of ω_n would be equal to zero since an airplane has 6 rigid body modes - 3 related to translational directions and another 3 related to rotational directions. Thus, only the 7^{th} mode would have a non-zero ω_n, corresponding to a deformable mode where the potential energy is not zero.

Once the values of ω_n (eigenvalues) are obtained, they are substituted back into Equation 2.42 to obtain the eigenvectors, that is, the $\{\phi\}$ vectors corresponding to each ω_n value. Thus, by performing this substitution, a known vector $\left\{\hat{\phi}\right\}$ is obtained, which is then multiplied by an unknown constant A_i.

$$\{\phi\}_i=A_i\cdot\left\{\hat{\phi}\right\}_i \tag{2.44}$$

With all the vectors $\{\phi\}_i$, it is possible to build a modal matrix $[\phi]$, which will be an $M\times M$ square matrix. This modal matrix proves to be highly useful because it enables the diagonalisation of the stiffness and mass matrices ($[K]$ and $[M]$, respectively), significantly simplifying the calculations to be performed:

$$[\phi]^T\,[K]\,[\phi]=[D_K] \tag{2.45a}$$

$$[\phi]^T\,[M]\,[\phi]=[D_M] \tag{2.45b}$$

There are three different ways to define the unknown constant A_i, namely:

- Normalise with respect to the **maximum value** of the vector $\left\{\hat{\phi}\right\}_i$, that is, consider the unknown constants to take values such that the maximum value of the vector $\{\phi\}_i$ becomes equal to 1;

- Normalise with respect to the **mass matrix**, which means defining the unknown constants in such a way that the modal matrix becomes equivalent to the mass matrix in the identity matrix;

$$\left[\tilde{\phi}\right]^T[M]\left[\tilde{\phi}\right]=[D_M]=[I] \tag{2.46}$$

- Normalise with respect to the **stiffness matrix**, which means defining the unknown constants in such a way that the modal matrix becomes equivalent to the stiffness matrix in the identity matrix;

$$\left[\breve{\phi}\right]^T [K] \left[\breve{\phi}\right] = [D_K] = [I] \tag{2.47}$$

Nevertheless, as will be understood later, the use of this type of normalization can lead to significant problems and, therefore, it is not very common.

Furthermore, it is important to highlight that the modal vectors enjoy the property of orthogonality, i.e., $\{\phi\}_i^T \cdot \{\phi\}_j = 0$ if $i \neq j$ [39]. From this property, a very useful conclusion can be drawn in the future, namely, that both the elastic forces and the inertial forces will only do work in their direction. Therefore, it can be stated that in a multi-degree-of-freedom system, its vibration can be obtained by summing all the vibrations of the different modes.

Finally, it is also observed that for MDOF systems, the following expression is valid:

$$\omega_{n_i}^2 = \frac{\{\phi\}_i^T [K] \{\phi\}_i}{\{\phi\}_i^T [M] \{\phi\}_i} \tag{2.48}$$

This expression is quite similar to the one verified for SDOF systems (Equation 2.11). However, it is not very practical because to apply it, one needs to determine the vectors (ϕ), which, as shown earlier, requires prior knowledge of the eigenvalues ω_{n_i}.

2.4.2 Force vibrations for undamped systems

For this case, Equation 2.39 can be simplified as follows:

$$[M]\{\ddot{u}\} + [K]\{u\} = \{F(t)\} \tag{2.49}$$

Analysing Equation 2.49, it is evident that if the matrices $[M]$ and $[K]$ are not diagonal, solving this system can entail significant computational costs. Therefore, it is common to transform the physical coordinates into modal coordinates to make these matrices diagonal, as previously mentioned. To achieve this, the following transformation will be applied:

$$\{u(t)\} = [\phi] \cdot \{\nu(t)\} \tag{2.50}$$

Therefore, applying Transformation 2.50 to Equation 2.49 and multiplying it by $[\phi]^T$ results in:

$$[\phi]^T [M] [\phi] \{\ddot{\nu}(t)\} + [\phi]^T [K] [\phi] \{\nu(t)\} = [\phi]^T \{F(t)\} \tag{2.51}$$

Also, for this case, the three types of normalizations mentioned earlier can be conducted. Thus, assuming that $F_m(t) = [\phi]^T \{F(t)\}$ represents the modal force, depending on the chosen normalization type, Equation 2.51 can be simplified as follows:

- **Normalisation with respect to the maximum value**

$$[D_M]\{\ddot{\nu}(t)\} + [D_K]\{\nu(t)\} = \{F_m(t)\} \tag{2.52}$$

- **Normalisation with respect to the mass matrix**

$$[I]\{\ddot{\nu}(t)\} + \left[\Omega^2\right]\{\nu(t)\} = \{F_m(t)\} \tag{2.53}$$

Where $\left[\Omega^2\right]$ corresponds to a diagonal matrix that contains, in a sorted order, all the squared natural angular frequencies of the system under study.

- **Normalization with respect to the stiffness matrix**

$$\left[\frac{1}{\Omega^2}\right]\{\ddot{\nu}(t)\} + [I]\{\nu(t)\} = \{F_m(t)\} \tag{2.54}$$

Where $\left[\frac{1}{\Omega^2}\right]$ corresponds to a diagonal matrix with its diagonal elements orderly containing the inverse of all the squared angular frequencies of the system under study. Therefore, if the system has any rigid-body modes, meaning any $\omega = 0$, performing this normalisation will lead to an indeterminate result. Hence, the reason why this normalisation is uncommon is now clarified.

Given the ease of working in modal coordinates, as they allow the system to be diagonalised and solve M individual equations (as if M-SDOF systems were considered), the Transfer Function (TF) will be applied, as previously done for SDOFs systems. For this purpose, it is important to note that:

$\{\nu(t)\} \overset{TF}{\to} \{\nu(\omega)\}$ (2.55a) $\{\ddot{\nu}(t)\} \overset{TF}{\to} \{\ddot{\nu}(\omega)\}$ (2.55b) $\{F_m(t)\} \overset{TF}{\to} \{F_m(\omega)\}$ (2.55c)

Thus, applying the TF to Equation 2.51, the result is:

$$-\omega^2 [D_M]\{\nu(\omega)\} + [D_K]\{\nu(\omega)\} = \{F_m(\omega)\} \Leftrightarrow$$

$$\{\nu(\omega)\} = \left([D_K] - \omega^2 [D_M]\right)^{-1}\{F_m(\omega)\} \tag{2.56}$$

Expanding Equation 2.56 from modal coordinates to physical coordinates yields the following expression:

$$\{U(\omega)\} = [\phi]\left([D_K] - \omega^2 [D_M]\right)^{-1}[\phi]^T\{F(\omega)\} \Leftrightarrow \tag{2.57}$$

$$\{U(\omega)\} = [H(\omega)]\{F(\omega)\} \tag{2.58}$$

Hence, the function $H(\omega)$ for undamped MDOF systems takes the following expression:

$$[H(\omega)] = \frac{[\phi][\phi]^T}{([D_K] - \omega^2 [D_M])} \tag{2.59}$$

Typically, Equation 2.58 is written in the following form:

$$U_\alpha(\omega) = \sum_{\eta=1}^{N} H_{\alpha\eta}(\omega)F_\eta(\omega) \tag{2.60}$$

Nevertheless, in this case, $H_{\alpha\eta}(\omega)$ takes the following expression:

$$H_{\alpha\eta}(\omega) = \sum_{k=1}^{N} \frac{\hat{\phi}_{k\alpha}\hat{\phi}_{k\eta}}{M_k\left(\omega_{n_k}^2 - \omega^2\right)} \tag{2.61}$$

It is important to mention that the letter α refers to the point where the response is measured, while the letter η refers to the point where the structure is excited. Therefore, this way of writing the transfer function proves to be very useful as it allows for studying the response of the system at the selected points. It can also be noted that if the variable N in the summation of Equation 2.60 is equal to 1, meaning that the system under study is excited by a single external force, this formula will be the same as the one derived for SDOF systems using the TF (Equation 2.35).

Moreover, the term $\hat{\phi}_{k\alpha}\hat{\phi}_{k\eta}$ in Equation 2.61 measures the intensity with which a particular modal shape contributes to the response of the structure when subjected to external excitation.

In conclusion, it is also important to highlight that modal shapes often have nodes, which are points where the structure does not vibrate at the relative frequency of that modal shape. Thus, analysing Equation 2.61, it can be seen that if the response is measured at a node of a modal shape, k, $\hat{\phi}_{k\alpha}$ will be zero, or if the structure is excited at a node of a modal shape, k, $\hat{\phi}_{k\eta}$ will also be zero. Therefore, it can be stated that, when this occurs, the function $H_{\alpha\eta}(\omega)$ will lose the frequency peak corresponding to that modal shape. This is why, when performing an experimental activity, it is important to estimate the positions of the nodes of the modal shapes to be studied beforehand and, if one wishes to visualize all the frequency peaks, avoid exciting or measuring the response at those points.

2.4.3 Force vibrations for damped systems

This case has not been considered until now because the matrix $[C]$ in Equation 2.39, unlike the matrices $[M]$ and $[K]$, often proves to be non-diagonalizable when multiplied by the modal shape matrices. Therefore, to consider this matrix, there are two distinct ways to do it [22, 29].

- The first possibility consists of writing the matrix $[C]$ as a linear combination of the diagonalisable matrix $[D_M]$ and the diagonalisable matrix $[D_K]$.

  $$[C] = \delta\,[D_m] + \varrho\,[D_K] \tag{2.62}$$

  By following this procedure, it ensures that the sum of two diagonalisable matrices will always result in a diagonalisable matrix. Moreover, with the values of δ and ϱ, one can estimate the values of ζ as follows:

  $$\delta + \varrho\omega_{n_k}^2 = 2\zeta_k\omega_{n_k} \tag{2.63}$$

  Indeed, this procedure is not always feasible and advisable because in these cases, there must be a prior guarantee that $[C]$ is a diagonalisable matrix, meaning that for each natural frequency, there is only one unique value of ζ.

- **The second possibility**, although more complex, proves to be more useful. Similar to what was explained for the SDOF case, this approach involves determining the response and excitation in the frequency domain and then obtaining the experimental values of $H(\omega)$. Subsequently, the theoretical expression of $H(\omega)$ is compared with the experimental values using appropriate software. However, the obtained expression for the function $H(\omega)$ for MDOF systems does not include the damping term (see Equation 2.61), as it was derived for the situation of **force vibrations for undamped systems**. Therefore, to obtain the expression of $H(\omega)$ that accounts for damping, an analogy with the **Force vibrations for damped systems** situation of SDOF systems (see Equation 2.36) must be made. By making this analogy, the following expression is obtained:

  $$H_{\alpha\eta}(\omega) = \sum_{k=1}^{N} \frac{\hat{\phi}_{k\alpha}\hat{\phi}_{k\eta}}{M_k\left(\omega_{n_k}^2 - \omega^2 + j2\zeta_k\omega_{n_k}\omega\right)} \tag{2.64}$$

  In this way, it is important to consider that all FRF plots in Chapter 7 were obtained by applying Equation 2.64.

Chapter 3

Numerical analysis of structural systems with FEM

In this chapter, a literature review will be presented regarding the evolution and application of the primary numerical method employed across various industries for structural analyses, with particular emphasis on the aerospace industry, namely the Finite Element Method (FEM).

3.1 Introduction to numerical methods used in structural analyses

The FEM, as mentioned earlier, is a widely employed numerical technique for solving differential equations of complex structures. It is noteworthy that this method, which was developed through the contributions of several mathematicians, particularly in the early second half of the 20th century [40], can be regarded as an evolution of a preceding numerical method, specifically the Rayleigh-Ritz method [41]. The latter was formulated based on the works of mathematicians and physicists Lord Rayleigh and Walter Ritz in the early 20th century [42]. Despite its diminished practical utility in contemporary times, it will now be addressed, as comprehending its properties and limitations will facilitate a deeper understanding of the FEM approach.

Therefore, this method involves approximating the response by summing the product of two functions: a known spatial function ($p_{ui}(x, y)$) and an unknown temporal function ($\eta_{ui}(t)$), as depicted in Equation 3.1 [22].

$$u(x, y, t) \approx \sum_{i=1}^{M} p_{ui}(x, y)\eta_{ui}(t) = [p_u(x, y)]\{\eta_u(t)\} \tag{3.1}$$

It is worth noting that for $u(x, y, t)$ to actually yield a good approximation, at least the geometric boundary conditions must be satisfied. Consequently, this numerical method possesses four properties that render its application a considerably intricate task, or even impossible in certain structures. Thus, these very properties are as follows [15, 22]:

- The unknown function lacks any physical significance, rendering the physical understanding of the problem more intricate;

- Since the temporal function is unknown, it is easier to apply geometric boundary conditions to the spatial function. However, given that the mass, stiffness, and force matrices (indispensable for this type of study and which will be discussed in greater detail downstream) are associated with this spatial function. So, any alteration of the problem's conditions necessitates recalculating these matrices, thereby leading to an increase in computational cost;
- The obtained solution is as accurate as the value of M in the summation of Equation 3.1 is larger. In other words, for $u(x, y, t)$ to represent a better approximation, it is necessary to use more terms, which may also result in a significant increase in computational cost.
- Furthermore, the spatial function must be defined over the global domain of the structure, which can be a highly limiting issue when dealing with structures of high associated complexity.

In this manner, all of these challenges were overcome through the FEM. This method is considered an advancement from the Rayleigh-Ritz method, as it conceptually represents a "kind of change of variables" from this former numerical approach. Similar to the Rayleigh-Ritz method, FEM also approximates the response by summing the product of two functions: an unknown temporal function $(q_{ui}(t))$ and a known spatial function ($N_{ui}(x, y)$), the latter of which is also known as a shape function. However, the functions N_{ui} are derived from modifications of the functions p_{ui} in such a way that the temporal unknown functions acquire specific physical significance. Consequently, the functions q_{ui} will represent the variables under study in the problem, such as axial displacements, transverse displacements, and so on. These transformations that enable a parallel between these two numerical methods can be observed in Equation 3.2 [29].

$$u(x, y, t) \approx \sum_{i=1}^{M} p_{ui}(x, y)\eta_{ui}(t) \Rightarrow \sum_{i=1}^{M} N_{ui}(x, y)q_{ui}(t) = [N_u(x, y)]\,\{q_u(t)\} \tag{3.2}$$

Taking this into consideration, it is possible to emphasize that one of the advantages of FEM lies in the fact that the unknown functions possess specific physical significance, rendering the comprehension of obtained results more accessible [15, 22].

It is also noteworthy that, given these unknown functions have physical significance in the FEM approach, in contrast to the Rayleigh-Ritz method, geometric boundary conditions can be directly applied to these very functions. Consequently, the second issue previously mentioned ceases to exist, as applying boundary conditions to the temporal function ensures that the spatial functions N_{ui} will always assume the same algebraic expression regardless of the boundary conditions of the problem at hand. Therefore, altering the boundary conditions will not necessitate the recalculation of matrices related to mass, stiffness, and force, matrices which, as mentioned earlier, solely depend on the spatial function [22].

Furthermore, it is evident that for the application of the FEM method, the analyzed domain is discretized into multiple subdomains, with each of these subdomains subject to the resolution of the relevant differential equations. These subdomains are referred to as Finite Elements (FE), and each of these FE has nodes (points that serve as connections to other FE in the structure). The entirety of these subdomains is referred to as the MESH. An illustration of this discretization can be seen in Figure 3.1.

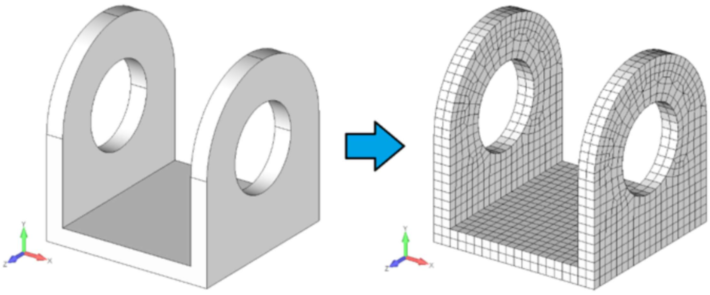

Figure 3.1: Example of a discretisation of a mechanical part using FEM [43].

Having said this, this strategy is feasible and proves effective because the shape functions consistently maintain the same algebraic expressions. To enhance result accuracy, contrary to the Rayleigh-Ritz method (where it's necessary to employ more terms in Equation 3.1), in the FEM approach, increasing the number of Finite Elements (FEs) suffices, ensuring mathematical continuity of the differential equations at the nodes of these FEs [22].

Finally, the last advantage of FEM over the Rayleigh-Ritz method lies in the fact that applying this method doesn't require defining shape functions across the global domain of the structure. Therefore, for more complex structures, it's common to compute shape functions within a local domain and subsequently algebraically transform these functions into a global reference system [22].

Having clarified the conceptual advantages of the FEM method over the Rayleigh-Ritz method, the properly sequenced methodology followed by this numerical approach will now be outlined, namely:

- Structure modeling and definition of all boundary conditions and other significant parameters using specific software for this purpose (such as Patran);
- Discretization of the structure - a process also referred to as Meshing;
- Calculation of the mass, stiffness, and force matrices in a local reference system through the differential equations using specific software for this purpose (such as Nastran);
- Transformation of the local reference system used to define these matrices into a global reference system;
- Assembly of all these matrices;
- Attainment of the final solution, often followed by Post Processing of the obtained results to generate graphs, animations, and other analyses.

3.2 Advantages and disadvantages of the FEM

After providing a brief historical introduction to the FEM and its functioning, it is now crucial to delineate its actual primary advantages and disadvantages. This will serve to elucidate the pitfalls that must be circumvented to attain a solution congruent with the reality under examination.

Commencing with the advantages attributed to this method, it is noteworthy to observe that [23]:

- The FEM can be applied to a wide range of situations, encompassing linear, nonlinear, static, and dynamic problems. Furthermore, as previously mentioned, it is feasible to analyze structures with highly intricate geometries and to impose various boundary conditions on said structures;

- By employing the FEM, it becomes possible to obtain a reliable estimation of the properties under investigation without the necessity of constructing a preliminary physical model. Consequently, the utilization of FEM can lead to resource savings;

- Parametric analyses can be conducted through the application of FEM, facilitating the identification of parameters that, when altered, exert a significant impact on the studied system (sensitivity analysis);

- FEM analyses allow for the adaptation of the mesh according to the obtained results. Thus, in cases where specific interest lies in comprehensively studying a certain area of a structure, it is feasible to refine the mesh exclusively in those areas, thereby achieving a more accurate approximation.

Turning to the drawbacks, it is evident that [23] elucidates the following:

- At times, contingent on the complexity of the given problem, the application of FEM may entail substantial computational costs. This issue gains prominence, particularly when the necessity arises to conduct studies involving three-dimensional models or perform nonlinear analyses;

- In certain instances, inadequate construction of the mesh can yield results that poorly reflect reality;

- The presence of singularities or uncommon boundary conditions might necessitate the utilization of specialized numerical techniques within FEM. Such circumstances can incur high computational costs or lead to less reliable approximations;

- The utilization of overly fine meshes (meshes with a high number of finite elements) can also lead to imprecise solutions. This arises due to the potential amplification of minor errors associated with any approximate numerical method, such as FEM, within this type of mesh.

Given the multitude of errors arising from human factors and inherent approximations employed by FEM, the outcomes yielded by this numerical method do not invariably align with the reality under examination. Consequently, validation of these outcomes through experimental means or alternative numerical techniques is imperative in the analysis of any structure. Thus, the next section will delve more comprehensively into the subject of validating FEM results.

3.3 Validation of FEM results

Typically, and in line with the approach used to validate the attained outcomes, it is common to compare the results derived from Finite Element Analysis (FEA) with those obtained through experimental testing. Following this comparison, should it be determined that FEA has failed to yield results congruent with the reality being studied, the recourse is invariably towards enhancing or rectifying any aspect of the FEA that engenders this disparity with reality. This iterative process, as depicted in Figure 3.2, persists until the observed discrepancy ceases to manifest as a significant phenomenon [44].

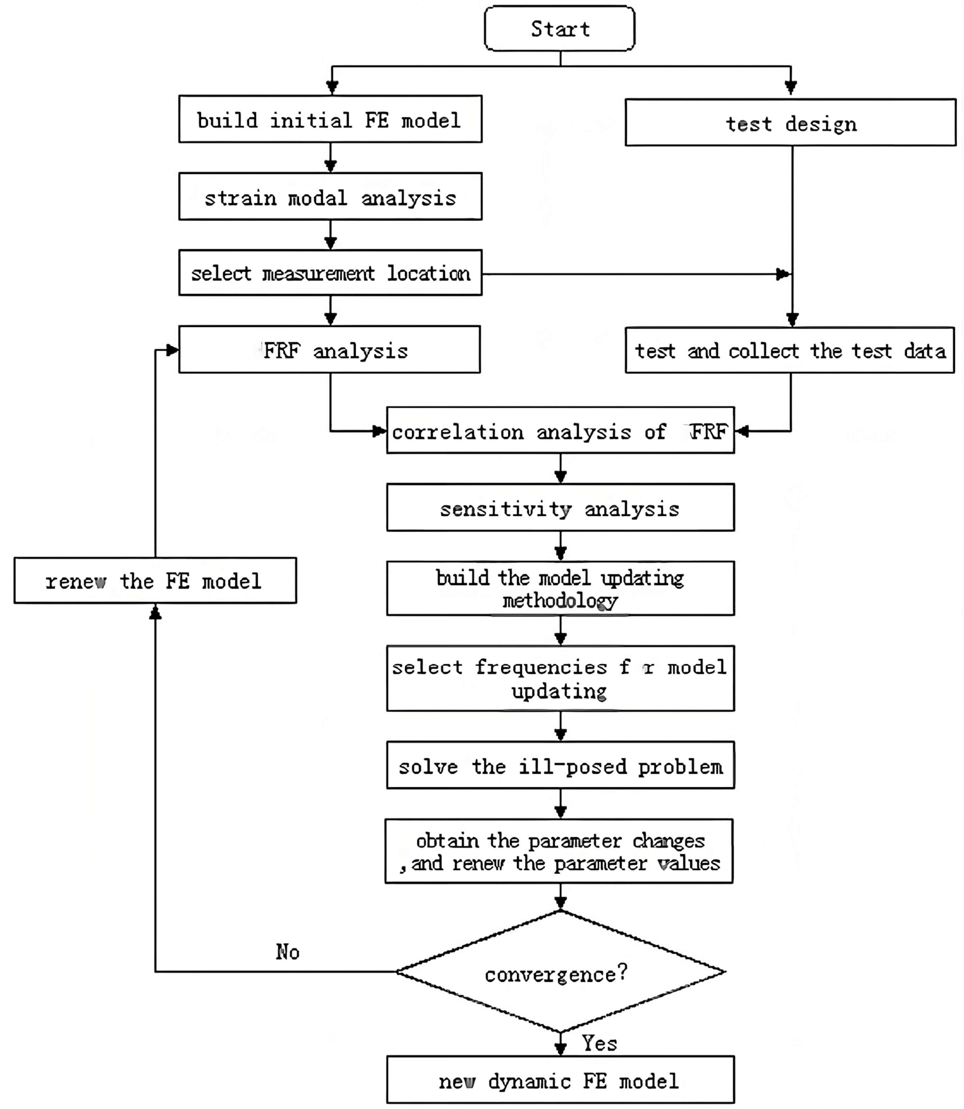

Figure 3.2: Flow chart of model updating using correlation analysis of FRFs [44].

Furthermore, it is known that the data processing facilitating the execution of this comparison of results can assume various formats, with the most common (employed in this work) being the frequency response graph.

Lastly, it is customary to quantify the level of correlation in the obtained results, and this quantification also aids in determining whether the FEA should be reiterated to yield more coherent outcomes.

Chapter 4

Construction and Analysis of Numerical Models

This chapter will begin with enunciating all the necessary physical and geometrical characteristics for constructing the numerical model. Subsequently, the results obtained after applying the Finite Element Method to the constructed numerical models will be presented and analyzed.

4.1 FEM Modelling

As previously mentioned in Chapter 1, all four beams under study are composite beams. Therefore, it's important to highlight that each of these beams, as illustrated in Figure 4.1, is composed of **two aluminium faces** - *AL 7075* - and a core consisting of a **polymer foam** - *WF 110*. These two materials are isotropic, which means they exhibit consistent mechanical behaviour in all three dimensions. Consequently, it is known that material constants related to Young's modulus (E), shear modulus (G), and Poisson's ratio (ν) will remain the same for different directions:

$$E_x = E_y = E_z = E \;\; ; \;\; G_{xy} = G_{xz} = G_{yz} = G \;\; ; \;\; \nu_{xy} = \nu_{xz} = \nu_{yz} = \nu$$

Thus, it is possible to write the Equation 4.1 for isotropic materials.

$$G = \frac{E}{2(1+\nu)} \tag{4.1}$$

From Equation 4.1, it is easily understood that to define such materials, it's only necessary to input the values of two out of the three unknowns: E, G, and ν. Additionally, it's also essential to provide the value of the mass density (ρ) for each of these materials, as knowledge of this constant is imperative for conducting modal analyses. It's worth noting that the values of all these constants were determined experimentally by Engineer Matteo Sorrenti and are also presented in Table 4.1 [45].

Table 4.1: Values of the physical constants of the materials that make up the beams under study.

material	E [MPa]	G [MPa]	ν	ρ [kg/m^3]
AL 7075	67545.6	25393.1	0.33	2750.6
WF 110	194.1	66.9	0.45	109.5

Furthermore, it should be highlighted that, as expected, for constructing the computational model, it was also necessary to input the values of all the geometric dimensions of both materials composing the beams under study. These values were measured using a ruler and a digital calliper (see Table 4.2). Lastly, it should be mentioned that due to the lack of experimental data and the difficulty in predicting the mechanical behaviour of the adhesive used by the beam manufacturer to bond the AL 7075 faces to the WF 110 core, it was not considered in the numerical model.

Table 4.2: Geometric properties of the beams under study.

	Length [mm]	**Width [mm]**	**Thickness [mm]**	**Thickness of each aluminum faces [mm]**	**Thickness of core [mm]**
Beam 1	5000± 0.5	800± 0.5	43.32± 0.01	2	39.32± 0.01
Beam 2	5000± 0.5	800± 0.5	41.18± 0.01	1	39.18± 0.01
Beam 3	5000± 0.5	800± 0.5	33.53± 0.01	2	29.53± 0.01
Beam 4	5000± 0.5	800± 0.5	31.54± 0.01	1	29.54± 0.01

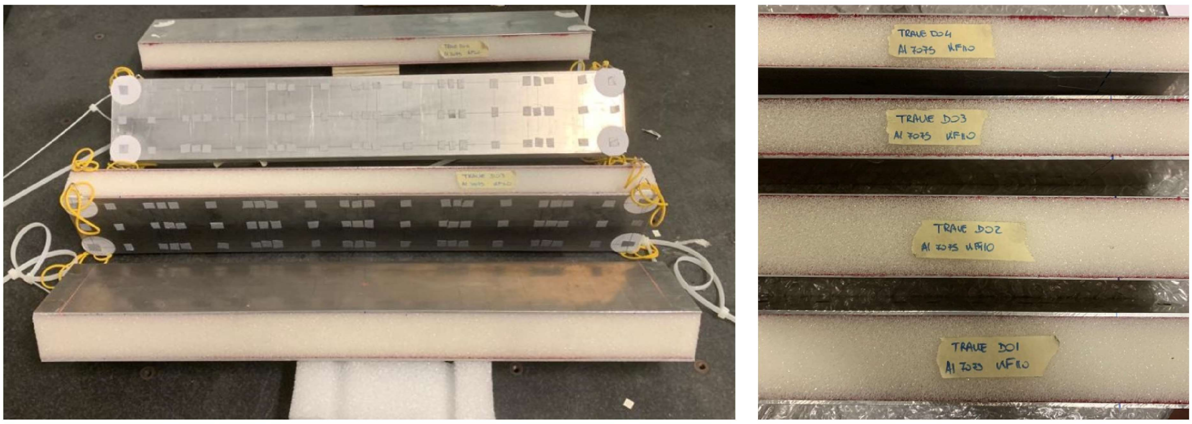

Figure 4.1: Composition of the 4 beams under study.

Taking all of this into account, it is important to begin by stating that the software used to perform these numerical analyses were Patran, for modelling the beams and visualizing the results, and Nastran for obtaining the results. Additionally, in order to optimize the numerical analyses, the `.ses` files were parameterized to only change the thickness values of their components, which as can be seen in Table 4.2 is the only geometric dimension that varies from beam to beam.

With that said, it should be noted that the meshes for all beams were created in the same manner. In this regard, Solid elements **Hexa8** (3D elements with 8 nodes per element) were used for the core and Shell elements **Quad4** (2D elements with 4 nodes per element) were used for the aluminium faces. In terms of subdivisions, the same configuration was applied to all the beams under study, meaning the length was divided into 250 FE, the width into 20 FE, and the thickness into 10 FE. Thus, each of the beams was subdivided into a total of 42579 FE (see Figure 4.2). The convergence of this mesh was previously ensured by engineer Matteo Sorrenti [45].

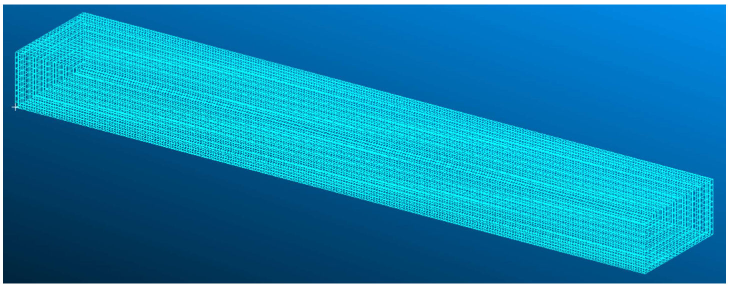

Figure 4.2: Mesh of one of the beams under study.

Before revealing the numerically obtained results for each of the beams, it is important to note that for this analysis, the SOL 103 option in Patran was used because it is the option that enables modal analyses to be performed, and it was previously defined that Nastran should only calculate all normal frequencies between 10 Hz and 4000 Hz. The lower limit (10 Hz) is justified by the fact that it is not intended to study the 6 rigid body natural frequencies, which contrary to what was mentioned in Chapter 2.4.1 do not assume values equal to zero, given the fact that FEM is an approximate numerical method. The upper limit (4000 Hz) is justified by the decision to study all modal shapes up to and including the 5^{th} flexural modal shape. In the following section (see Chapter 4.2), it is noted that none of the beams under study exceeds 3060 Hz for this modal shape. Therefore, by conducting the experimental activities up to 4000 Hz, it should be possible to observe all the desired modal shapes.

4.2 FEA Results

Prior to presenting the numerical results obtained through the application of the FEM method, it is important to note that, as the structures under study do not exhibit significant geometric complexity (they are simply rectangular beams), the resonance frequencies will correspond to specific modal shapes. These modal shapes (which are the same for all the beams, since they all have the same length and width), as shown in Figure 4.3, can correspond to flexural modes relative to the x-axis, torsional modes relative to the x-axis, and flexural modes relative to the y-axis. Depending on the number of transverse nodal lines, these modal shapes assume different orders. For instance, in the case of flexural modal shapes, the corresponding order of the flexural mode will be the sum of the number of transverse modal lines plus 1, whereas, for torsional modal shapes, their order will correspond to the number of transverse modal lines present. In addition, it is important to note that, as explained in Chapter 6, it is not feasible to experimentally measure flexural modes relative to the y-axis. For this reason, these modal shapes were disregarded.

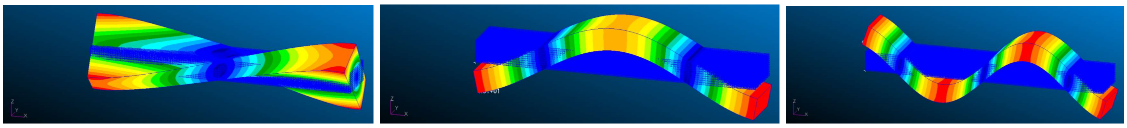

(a) 1^{st} torsional modal form around x (b) 1^{st} flexural modal form around z (c) 2^{nd} flexural modal form around z

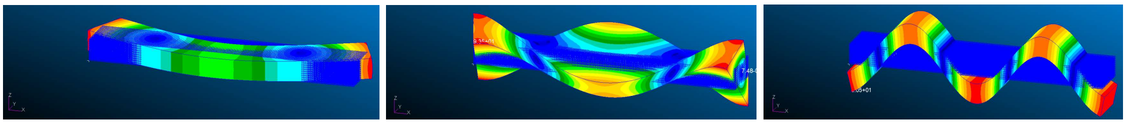

(d) 1^{st} flexural modal form around y (e) 2^{nd} torsional modal form around x (f) 3^{rd} flexural modal form around z

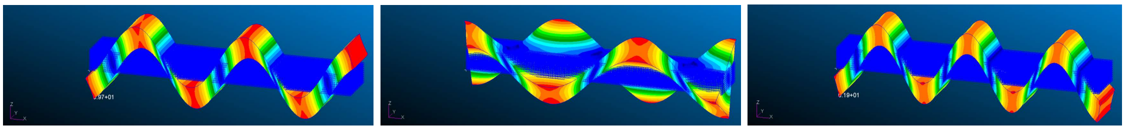

(g) 4^{th} flexural modal form around z (h) 3^{rd} torsional modal form around z (i) 5^{th} flexural modal form around x

Figure 4.3: Graphical representation of the modal shapes of all the beams under study.

As previously mentioned, the numerical analyses conducted enabled the estimation of all resonance frequencies ranging from 10 Hz to 4000 Hz. However, for a better understanding of the potential for resonance frequency measurements using LDV, it was established that, for all beams, only the results of experimental measurements up to the 5^{th} flexural modal shape would be considered. This decision was made due to the complexity associated with this modal shape (it has 6 transverse nodal lines). Thus, the numerical results obtained from the execution of the equations for MDOF systems for force vibrations and undamped systems (see Chapter 2.4.2) are presented in Table 4.3:

Table 4.3: Numerical results obtained for each of the beams under study.

1^{st} Beam	1^{st} **torsional** 704.97 Hz	1^{st} **flexural** 715.22 Hz	2^{nd} **flexural** 1169.4 Hz	2^{nd} **torsional** 1602.4 Hz	3^{rd} **flexural** 1669.8 Hz	4^{th} **flexural** 2101.5 Hz	3^{rd} **torsional** 2538.1 Hz	5^{th} **flexural** 2589.2 Hz
2^{nd} Beam	1^{st} **flexural** 753.14 Hz	1^{st} **torsional** 846.32 Hz	2^{nd} **flexural** 1344.4 Hz	2^{nd} **torsional** 1798.5 Hz	3^{rd} **flexural** 1947.3 Hz	4^{th} **flexural** 2489.8 Hz	3^{rd} **torsional** 2795.3 Hz	5^{th} **flexural** 3055.9 Hz
3^{rd} Beam	1^{st} **flexural** 620.64 Hz	1^{st} **torsional** 693.14 Hz	2^{nd} **flexural** 1052.6 Hz	2^{nd} **torsional** 1508.7 Hz	3^{rd} **flexural** 1511.8 Hz	4^{th} **flexural** 1925.3 Hz	3^{rd} **torsional** 2310.5 Hz	5^{th} **flexural** 2373.5 Hz
4^{th} Beam	1^{st} **flexural** 647.61 Hz	1^{st} **torsional** 827.48 Hz	2^{nd} **flexural** 1208.3 Hz	2^{nd} **torsional** 1712.7 Hz	3^{rd} **flexural** 1770.5 Hz	4^{th} **flexural** 2289.5 Hz	3^{rd} **torsional** 2583.7 Hz	5^{th} **flexural** 2815.7 Hz

Finally, a crucial point to emphasize is that the obtained results were compared with those derived from engineer Matteo Sorrenti's 2D numerical analysis of the studied beams [45]. The similarity between the outcomes in both numerical models suggests that errors in the construction of these models were highly unlikely.

Chapter 5

Experimental modal analysis

In this chapter, the exploration of two important topics in experimental modal analysis will commence. The first topic will focus on the relevant systems and concepts associated with experimental tests conducted in this area of study. The second topic will discuss metric correlations and common procedures for the comparison of the obtained results.

After that, an introduction to the physics underlying the technology of LDVs will be provided. The discussion will then cover the various types of LDVs and their key characteristics. Subsequently, the details of Polytec LDVs (the type used in this study) will be explored, along with an examination of the limitations and strategies that can be implemented in these devices to minimize experimental errors.

5.1 Modal testing

Now, all the concepts and instruments traditionally associated with modal testing will be addressed. First, mention will be made of the instruments commonly used to excite the system under study (input). Subsequently, the device typically employed to measure the response and the challenges associated with it will be discussed. Next, different types of boundary conditions will be covered, with a particular focus on the **Free-free condition**. Lastly, the coherence function will be explored, which, as will be demonstrated, is one of the functions that may allow the assessment of the quality of the experimental results obtained.

5.1.1 Excitation Input

It is known that to induce vibrations in a system for experimental modal testing, typically two devices are used, namely, a **Imapct Hammer** and/or a **Shaker**. Therefore, it is important to explain each of these instruments, mentioning their main advantages and disadvantages [46, 47].

Beginning with the enumeration of the primary advantages of the **Impact Hammer**, they include:

- This device has a simple and practical setup. In fact, it only requires connecting the hammer's cable to the computer, which will then collect the information from the impact and process the data accordingly;

- With this device, it is easy to excite multiple points on the structure. Therefore, using this device allows obtaining various FRF graphs, enabling a more comprehensive study of the structure;
- Compared to other devices, this is indeed a less expensive alternative.

However, it should be noted that this device has the following disadvantages:

- Given that a structure is struck with a hammer, there is always a risk of damaging it during this process;
- As mentioned earlier in Section 2.3, in order to study a wide range of frequencies from a single impulse, the hammering applied to the structure must approximate a Dirac delta function. This means that the hammer strike should start from zero initial conditions and not extend over time. However, it is practically impossible to achieve a perfect Dirac delta function, so the FRF graphs obtained will only allow the study of a limited frequency range.

Regarding the **Shaker**, it has the following advantages:

- The **Shaker** allows for the study of a wide range of frequencies because it is capable of applying sinusoidal excitation. As mentioned in Section 2.3, a sinusoidal force in the time domain corresponds to a peak in the frequency domain. Therefore, the **Shaker** applies multiple sinusoidal forces at different frequencies within a specified range defined by the user. By doing so, it becomes possible to observe the response of the system under study for each of the sinusoidal frequencies applied;
- As the force excitation is applied by a machine, and despite any machine or instrument always having some associated uncertainty, the amplitude of all vibrations will be quite precise when using such devices. It also prevents any potential damage to the structure under study.

Concerning the drawbacks of this device, the following points are notable:

- This device is more challenging to install, and for this reason, unlike the **Hammer**, it is more difficult to apply excitations at different points of the structure;
- It is generally more expensive than other instruments;
- Since this device needs to be connected to the structure under study, its application can introduce stiffness into the system, biasing the results.

Given the advantages of the **Shaker**, including its precision and ability to study a wide range of frequency values, most of the main studies in this work were conducted using this device. However, as will be observed, one of the bars under study was also excited using a **Hammer** to assess whether the **Shaker** introduced significant stiffness and mass into them.

Having said that it is also important to mention that both for the LDV and the Shaker, a Hanning window was used to reduce leakage effects [48].

5.1.2 Traditional response measurement

Typically, the traditional method for measuring responses involves the use of small piezoelectric accelerometers. These accelerometers are made of materials with piezoelectric properties, meaning that they can convert mechanical deformation into an electrical signal, which can be further analysed using dedicated software. When conducting tests on a structure, these accelerometers are placed at specific points on the structure, and their readings provide the data needed to generate the desired FRF plots [18].

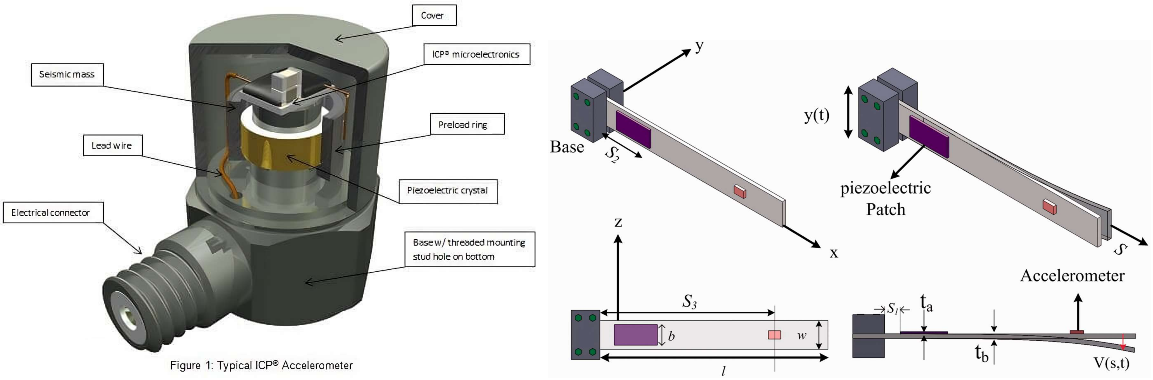

(a) Example of an accelerometer piezoelectric [49]

(b) Beam with piezoelectric accelerometers [50]

Figure 5.1: Experimental structural analyses.

However, the use of such devices can introduce a significant amount of experimental errors. This is mainly due to the fact that despite being relatively small, the mass of these devices may not be completely negligible. This effect, known as **Mass loading**, becomes particularly relevant in lightweight structures and in structures made of non-linear materials with high damping (such as rubber) [25]. To illustrate this effect, let's consider an SDOF system, for which Equation 5.1 can be expressed. It should be emphasized that f_0 represents the natural frequency of the system without the implementation of the accelerometers, while f_n represents the natural frequency of the system with the accelerometers in place. The difference between these two frequencies, denoted as Δf ($\Delta f = f_0 - f_n$), and the mass variation caused by the implementation of accelerometers, denoted as Δm, are also considered in the Equation 5.1.

$$\Delta f = f_0 - f_n \Leftrightarrow \frac{\Delta f}{f_0} = 1 - \frac{f_n}{f_0} = 1 - \sqrt{\frac{\frac{K}{m+\Delta m}}{\frac{K}{m}}} = 1 - \sqrt{\frac{m}{m+\Delta m}} \tag{5.1}$$

As shown in Equation 5.1, the use of piezoelectric accelerometers necessitates accounting for the effect of **Mass loading**, leading to the consideration of significant uncertainty and potentially affecting the accuracy of the results obtained [51]. Furthermore, the use of these devices can also alter the center of mass of the structure under study, which becomes particularly important when investigating forced vibrations [18].

5.1.3 Boundary conditions

Indeed, systems can be computationally analyzed by applying different boundary conditions, such as fixing one or more sides of the object (**Fixed-Free**), or they can be **Simply supported**, or no fixation can be applied (**Free-free condition**). However, despite both situations being possible to simulate computationally, in reality, it is impossible to experimentally study any system in a perfect **Free-free condition**, as it is physically impossible to suspend the object in mid-air without any support. Furthermore, it is important to mention that one of the reasons for conducting experimental tests through an approximate configuration of **Free-free condition** is the fact that it is the easiest way to compare experimental results with those obtained numerically.

Thus, as the objective of this work is to study 4 beams in a **Free-free condition**, there was a need to test various support configurations to determine the best solution. As will be observed, the chosen configuration was the one that allowed for the closest approximation to a perfect **Free-free condition**, meaning the one that introduced the least rigidity into the structures under study.

5.1.4 Quality of experimental results

When performing an experimental activity in structural dynamics, it is always necessary to assess the quality of results obtained. This process is commonly done using the **Coherence function**, γ^2. To derive this function, the process begins by recalling Equation 2.35, which is derived from the Transfer Function.

Considering that during such tests, multiple measurements are taken, and the final result is an average of all these measurements (for example, the LDV used in this work performs between 30 to 50 measurements for each of the points it measures) and multiplying it by the conjugate (represented by *) of the system's input in Equation 2.35, the result is obtained:

$$\frac{1}{N}\sum_{n=1}^{N} U_n(\omega)F_n^*(\omega) = H(\omega)\frac{1}{N}\sum_{n=1}^{N} F_n(\omega)F_n^*(\omega) \tag{5.2}$$

Simplifying the expression from the aforementioned equation results in:

$$G_{FU}(\omega) = H(\omega)G_{FF}(f) \Leftrightarrow H(\omega) = \frac{G_{FU}(\omega)}{G_{FF}(\omega)} \tag{5.3}$$

Traditionally, the functions $G_{FF}(\omega)$ and $G_{FU}(\omega)$ are referred to as the **Average Auto-Spectrum of F** and **Averaged Cross Spectrum between input F and output U**, respectively.

To obtain the coherence function, it is necessary to deduce the expression for $H(\omega)^{-1}$. By carrying out this deduction, it is known that:

$$U(\omega) = H(\omega)\cdot F(\omega) \Leftrightarrow U(\omega)\cdot H(\omega)^{-1} = F(\omega) \tag{5.4}$$

Multiplying each term of Equation 5.4 by the complex conjugate of the system output, and considering that in experimental tests multiple measurements are commonly performed, the result is obtained:

$$\left(\frac{1}{N}\sum_{n=1}^{N} U_n(\omega)U_n^*(\omega)\right)\cdot H(\omega)^{-1} = \frac{1}{N}\sum_{n=1}^{N} F_n(\omega)U_n^*(\omega) \tag{5.5}$$

Simplifying the preceding equation results in:

$$G_{UU}(\omega)H(\omega)^{-1} = G_{UF}(\omega) \Leftrightarrow H(\omega)^{-1} = \frac{G_{UF}(\omega)}{G_{UU}(\omega)} \tag{5.6}$$

With the two previous derivations, it is known, by definition, that the γ^2, results from the multiplication of $H(\omega)$ by $H(\omega)^{-1}$. Therefore, it follows that:

$$\gamma^2 = H(\omega)\cdot H(\omega)^{-1} = \frac{G_{FU}(\omega)\cdot G_{UF}(\omega)}{G_{FF}(\omega)\cdot G_{UU}(\omega)} = \frac{\frac{1}{N}\left(\sum_{n=1}^{N} U_n(\omega)F_n^*(\omega)\right)\cdot\frac{1}{N}\left(\sum_{n=1}^{N} F_n(\omega)U_n^*(\omega)\right)}{\frac{1}{N}\left(\sum_{n=1}^{N} F_n(\omega)F_n^*(\omega)\right)\cdot\frac{1}{N}\left(\sum_{n=1}^{N} U_n(\omega)U_n^*(\omega)\right)} \tag{5.7}$$

Having derived this function, it is now important to explain its physical significance. Therefore, coherence is a function used to compare, through multiplication by conjugates, a hypothetical round trip of the input signal. If this hypothetical round trip were perfect, the coherence function would assume a value of 1. However, if the signal were subject to any perturbations (noise), the γ^2 would assume a positive value, but less than 1.

Therefore, coherence is a dimensionless parameter that varies between 0 and 1 and evaluates the quality of the results obtained, i.e., whether the system under study has noise and whether it is capable of significantly perturbing the results obtained.

Taking all this into account, it is now easy to understand why it is necessary to perform more than one measurement for each of the points. Thus, in the scenario of making only one measurement, where N would be equal to 1, Expression 5.7 would take the following form:

$$\gamma^2 = \frac{U_1(\omega)F_1^*(\omega)\cdot F_1(\omega)U_1^*(\omega)}{F_1(\omega)F_1^*(\omega)\cdot U_1(\omega)U_1^*(\omega)} = 1 \tag{5.8}$$

As observed in 5.8, γ^2 would always be equal to 1, and thus it would not be possible to evaluate, in this particular case, the existence of any possible noise that may exist both at the input and output of the system.

The **Coherence Function** can also be interpreted as the introduction of two noise functions, one at the input and one at the output of the system, as shown in Figure 5.2:

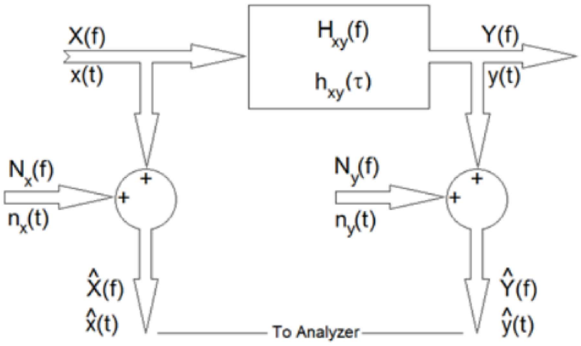

Figure 5.2: Representation of a system with the noise functions [52].

Considering that the input noise function is denoted as $N_{\text{X}}(f)$ and the output noise function as N_{Y}(f), the system's input will be symbolized by the variable X̂(f) (which represents the sum of N_{X}(f) and X(f), as depicted in Figure 5.2) and the system's output will be denoted as Ŷ (f) (which represents the combination of N_{Y}(f) and Y(f), as shown in Figure 5.2). Consequently, the cross-spectrum functions of this system will be identified as $\hat{G}_{\text{XX}}(\omega)$, $\hat{G}_{\text{YY}}(\omega)$, and $\hat{G}_{\text{XY}}(\omega)$, which can be expressed as follows:

$$\hat{G}_{\text{XX}}(\omega) = G_{\text{XX}}(\omega) + G_{N_{\text{X}}\text{X}}(\omega) + G_{\text{X}N_{\text{X}}}(\omega) + G_{N_{\text{X}}N_{\text{X}}}(\omega) \tag{5.9a}$$

$$\hat{G}_{\text{YY}}(\omega) = G_{\text{YY}}(\omega) + G_{N_{\text{Y}}\text{Y}}(\omega) + G_{\text{Y}N_{\text{Y}}}(\omega) + G_{N_{\text{Y}}N_{\text{Y}}}(\omega) \tag{5.9b}$$

$$\hat{G}_{\text{XY}}(\omega) = G_{\text{XY}}(\omega) + G_{\text{X}N_{\text{Y}}}(\omega) + G_{\text{Y}N_{\text{X}}}(\omega) + G_{N_{\text{X}}N_{\text{Y}}}(\omega) \tag{5.9c}$$

Since the input noise only relates to the input signal function (X̂(f)) and the output noise only relates to the output signal function (Ŷ(f)), the cross-spectrum functions can be simplified as follows:

$$\hat{G}_{\text{XX}}(\omega) = G_{\text{XX}}(\omega) + G_{N_{\text{X}}N_{\text{X}}}(\omega) \tag{5.10a}$$

$$\hat{G}_{\text{YY}}(\omega) = G_{\text{YY}}(\omega) + G_{N_{\text{Y}}N_{\text{Y}}}(\omega) \tag{5.10b}$$

$$\hat{G}_{\text{XY}}(\omega) = G_{\text{XY}}(\omega) \tag{5.10c}$$

The following conclusion is reached:

$$\gamma^2 = \frac{\hat{G}_{\text{XY}}(\omega)\hat{G}^*_{\text{XY}}(\omega)}{\hat{G}_{\text{XX}}(\omega)\hat{G}_{\text{YY}}(\omega)} = \frac{G_{\text{XY}}(\omega)G^*_{\text{XY}}(\omega)}{\left(G_{\text{XX}}(\omega) + G_{N_{\text{X}}N_{\text{X}}}(\omega)\right)\left(G_{\text{YY}}(\omega) + G_{N_{\text{Y}}N_{\text{Y}}}(\omega)\right)} \leq \frac{G_{\text{XY}}(\omega)G^*_{\text{XY}}(\omega)}{G_{\text{XX}}(\omega)G_{\text{YY}}(\omega)} \leq 1 \tag{5.11}$$

Thus, the reason why the coherence function cannot exceed 1 is now exemplified and demonstrated [53, 54].

5.2 Metric correlations

Obtaining the modal shapes through experimental modal tests (see Chapter 7), it is necessary to determine whether they indeed provide a good approximation of the actual behaviour of the structure under study. To achieve this, Structural Dynamics commonly employs various correlation metrics to validate the experimentally obtained modal shapes. One of the most well-known correlations used in this work is the **Modal Assurance Coefficient** (MAC), which allows assessing the similarity between any two modal shapes. Thus, this correlation is expressed numerically as follows [22, 47, 55]:

$$MAC_{rs}^{AB} = \frac{\left|\{\phi_r^A\}\{\phi_s^B\}\right|^2}{\left(\{\phi_r^A\}^T \cdot \{\phi_r^A\}\right)\left(\{\phi_s^B\}^T \cdot \{\phi_s^B\}\right)} \tag{5.12}$$

Where:

- The indices **A** and **B** represent the models under study that will be compared. Thus, the letters **A** and **B** can represent any numerical or experimental model or even different versions of the same model, with varying levels of simplicity or complexity. It is also noteworthy that if **A** and **B** represent models with a different number of modes, the resulting MAC matrix, obtained by applying Equation 5.12, will not be square;

- ϕ_r^A - is the modal shape r calculated by model A;
- ϕ_s^B - is the modal shape s calculated by model B;

It is also important to mention that the MAC can take any value between 0 and 1. When it approaches 1, the compared modal shapes exhibit a high degree of similarity, whereas values close to zero indicate significant differences between the compared modal shapes. Therefore, if models A and B have the same number of modes and model A is the experimental model of the reliable numerical model B, the diagonal of the MAC matrix will have higher values.

5.3 Introduction to LDV

In order to obtain better and more consistent experimental results reflecting reality, Yeh and Cummins developed the first laser vibrometer in 1964 [51]. Initially, this technology was quite rudimentary due to its low sensitivity, and it could only be used on very diffuse surfaces. However, in the 1980s, it underwent significant software development, leading to the mass marketing of different and distinctive LDVs in the 1990s. The success of this technology is explained by its non-invasiveness (as it does not damage the structures being studied) and its ability to solve the Mass Loading problem.

Therefore, nowadays, it is already possible to see that these devices are used in an even more extensive list of applications, ranging from biomedical to quality control. They can even be employed in the implementation of modal analysis and resonance frequencies [26, 27].

It is worth mentioning the existence of a variation of this technology, namely the Scanning Laser Doppler Vibrometer, SLDV. Instead of measuring displacements or velocities, this technology enables the scanning of real structures, thereby allowing the creation of even more accurate numerical models. However, for the purpose of this activity, only an LDV will be used, and thus, it will be the technology explored in greater detail [26, 51].

Thus, to understand how to proceed to obtain acceptable results and to be aware of the necessary precautions during the experiment, it is essential to grasp the operation and theory behind a LDV. With this in mind, it is important to mention that an LDV is a device utilized for measuring vibrations using a laser light source, and the underlying theory that governs this technology is the Doppler effect [26].

5.3.1 Explanation for the use of laser light

It is important to begin by explaining why this sportive device utilizes a laser as its radiation source. This choice is attributed to the laser's emission of electromagnetic radiation, which operates based on the mechanism of ”stimulated emission.” This type of radiation source possesses the following characteristics [56]:

- The laser light beam is **Coherent and Monochromatic**;
  - **Coherent**: The emitted light has a constant wavelength (or frequency) and phase in time and space;
  - **Monochromatic**: The emitted light is characterized by a single wavelength or a set of properly defined wavelengths.
- Laser light is **Collimated**: This means that laser light consists of rays that are approximately parallel. Laser light can be easily manipulated by lenses and mirrors, which align the emitted rays coherently with each other. Consequently, the collimated nature of laser light ensures high accuracy associated with the vibrometer, enabling measurements of small volumes and precise positioning of the laser beam in the desired location.
- Laser light can be **Linearly polarized**: This fact is of great importance because when a light beam is linearly polarized, the plane containing the electric field and the direction of propagation of the wave remains constant. This property plays a significant role in the occurrence of interference phenomena between electric fields that lie in the same plane. Serving as the foundational principle behind the operation of any interferometer, this aspect will be explored later.

Given that Laser light possesses all these essential characteristics, crucial for the proper functioning of a laser vibrometer, this will be discussed later, the decision to use a laser source in the development of an interferometer such as the LDV is therefore justified [56].

5.3.2 Theory of the Doppler effect

Before anything else, it is imperative to comprehend the nature of the Doppler effect to understand how an interferometer operates in conjunction with the LDV. Taking this into account, it is noted that this effect was discovered by Christian Doppler in 1842 [56]. Thus, this physicist arrived at the theoretical formulation of the effect by placing a set of professional trumpeters in an open car of a moving train passing through the same station. He then asked these two groups to play the same note and hold it for a certain period of time. When the moving train passed by the station, Christian noticed that the notes of both groups did not match.

Disregarding the hypothesis that one of the groups made a mistake while playing the note, as they were two sets of professional trumpeters, Christian Doppler recognized that the sound of a given note is defined by the frequency of the note's wave. Based on this observation, he theorized that the frequency (physical property that defines the tone of any note on any musical instrument) of emitted waves changes when the source or receiver of any wave is in motion (see Figure 5.3) [56].

This principle was later demonstrated, generalized and is nowadays widely used in various devices. Through this effect, the explanation encompasses not just the change in the sound of a siren from a moving ambulance as one approaches or moves away from it but also how Edwin Hubble demonstrated the expansion of the universe [27, 51, 58].

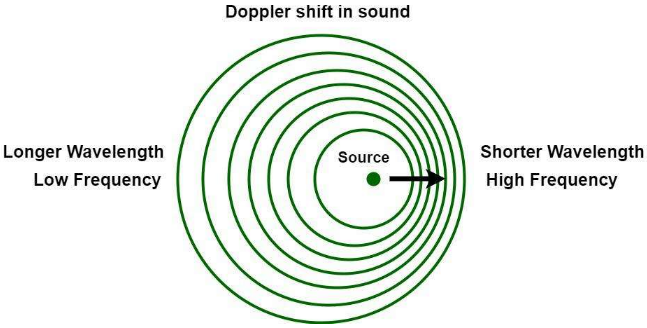

Figure 5.3: Representation of Doppler effect [57].

5.3.3 Application of the effect Doppler effect in LDV

Now, applying the Doppler effect to an LDV, representation starts with a fixed laser radiation source, denoted by the letter S, and a vibrating sandwich beam denoted by the letter P (in our case, set to vibrate by a Shaker with an LDV). As expected, when the radiation contacts the surface P, a change in its frequency will be observed. Furthermore, although this is not the case in reality, the assumption is made for simplicity that the photodetector, represented by the letter O, is positioned at a different location from the light source (see Figure 5.4) [56].

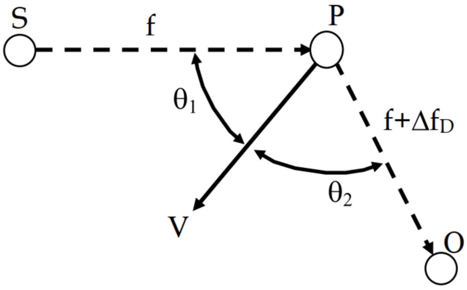

Figure 5.4: Doppler effect with source S and observer O in different locations [56].

Thus, knowing that the frequency is given by the expression:

$$f = \frac{c}{\lambda} \tag{5.13}$$

Where c is the speed of light and λ is the wavelength.

Consequently, the frequencies at the point P and O will be given by the following expressions, respectively:

$$f_P = \frac{(c + |v|\cos(\theta_1))}{\lambda} \tag{5.14a}$$

$$f_O = \frac{(c + |v|\cos(\theta_2))}{\lambda} \tag{5.14b}$$

Given the previous expressions, it can be seen that the frequency shift of the *SP* segment (Δ_{f_P}) and the frequency shift of the *PO* segment (Δ_{f_O}), will be defined by the following mathematical expressions:

$$\Delta f_P = \frac{|v|\cos(\theta_1)}{\lambda} \tag{5.15a}$$

$$\Delta f_O = \frac{|v|\cos(\theta_2)}{\lambda} \tag{5.15b}$$

Hence, in this particular case, the total frequency shift caused by the Doppler effect (f_D) can be expressed by the following mathematical expression:

$$\Delta f_D = \Delta f_P + \Delta f_S = \frac{|v|\left[\cos(\theta_1) + \cos(\theta_2)\right]}{\lambda} = \frac{|v|\left[\frac{\cos(\theta_1+\theta_2)}{2\cos(\theta_1-\theta_2)}\right]}{\lambda} \tag{5.16}$$

However, as already mentioned, this situation is not a faithful depiction of what happens in an LDV. To achieve a more accurate representation, it should be considered that the source and receiver are in the same position, as indicated in Figure 5.5.

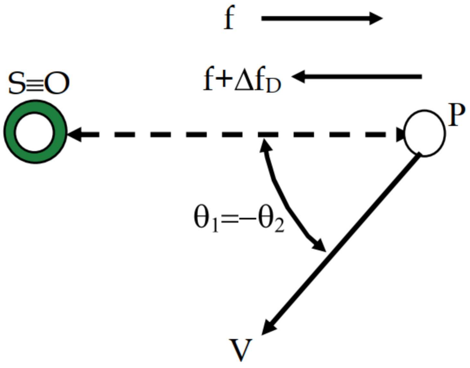

Figure 5.5: Doppler effect with source S and observer O in the same location: back-scattering [56].

Therefore, $\theta_1 = \theta_2 = \theta$. Thus, the total frequency shift caused by the Doppler effect can be expressed as follows:

$$\Delta f_D = \frac{2v_B}{\lambda} \tag{5.17}$$

Furthermore, as demonstrated, the Doppler effect is easily verifiable acoustically. This is due to the speed of sound at the earth's surface, which is approximately 340 m/s. For instance, considering a train traveling at 100 km/h and emitting a sound with a frequency of 200 Hz, the frequency shift caused by the Doppler effect will be approximately 8 Hz. Consequently, there would be a frequency difference of about 8.2%, a value easily measurable by any measuring device [56].

However, this is no longer true for light. The reason is that the speed of light is equal to 2,99792458$\times 10^8$ m/s. Considering the same train moving at the same speed of 100 km/h and measuring the frequency shift of the light emitted from its headlights (assuming the light has a normal wavelength, i.e., λ = 632,8 nm), the resulting value would be approximately 43.89 MHz. Although this value is relatively high in absolute terms, it is quite small in relative terms compared to the frequency of the light exiting the headlamp, which is approximately 474,68$\times 10^9$ Hz. As a result, the measuring apparatus would have to be capable of measuring a frequency difference of approximately 9$\times 10^{-4}$ % Hz, which is challenging to achieve, because it is difficult for a device to measure such a small frequency difference.

Thus, to enable the measurement of the Doppler effect of the laser light emitted by LDVs, these devices incorporated various strategies. All these different strategies will be discussed below, with a specific focus on the strategy present in the LDV to be used for this activity [56].

5.3.4 Different LDVs

There are several existing LDVs that can be used. However, the three most widespread are the Michelson's interferometer, the Mach-Zehnder interferometer and the Polytec LDV, as given in Figure 5.6 [51, 59].

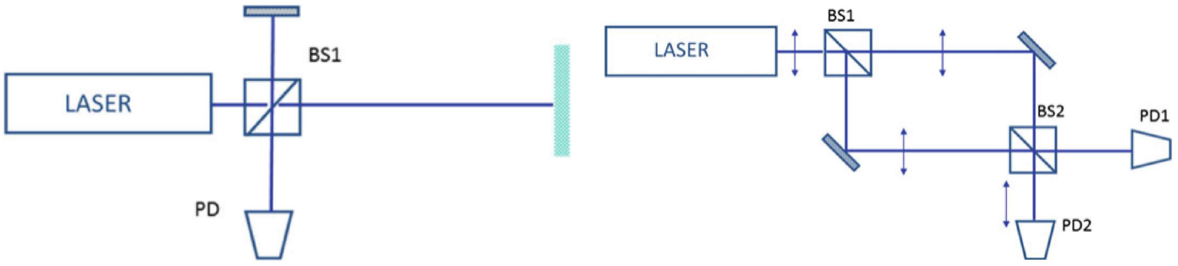

(a) Michelson's interferometer (b) Mach-Zehnder interferometer

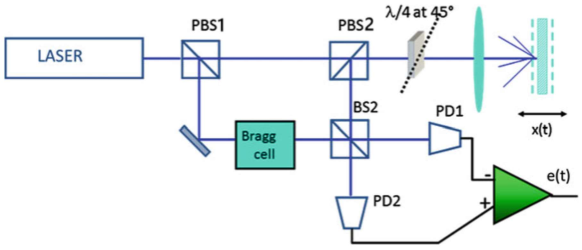

(c) Polytec LDV

Figure 5.6: The schemes of the different interferometers [56].

In particular, the Michelson's interferometer device introduces a fixed target to overcome the problem previously reported. This approach allows for an easier comparison of the frequency shift of two altered beams (one of these alterations is known since the frequency shift caused by the fixed target in the radiation is previously determined). However, this laser vibrometer has a major drawback as ensuring the two arms in the device's scheme are exactly symmetrical can be quite challenging. It has been found that even a small inclination in one of the arms or a slight deviation in the used beam splitter (which will be analyzed in more detail later) can seriously compromise the results obtained with this device, as can be seen in Figure 5.7 [59].

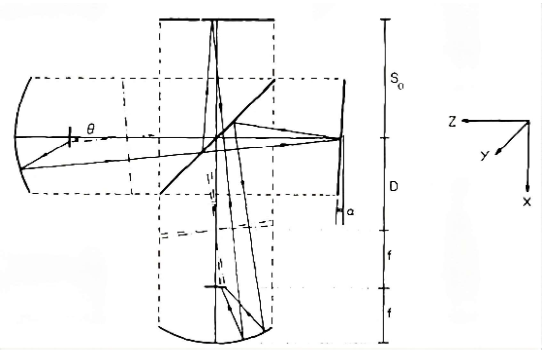

Figure 5.7: Representation of the possible Michelson's interferometer problem[59].

To circumvent this problem, the Mach-Zehnder interferometer opts to implement a Rotating Diffraction Grating as a rotating component (see Figure 5.8). Consequently, while the issues of component inclination and arm symmetry present in the Michelson's interferometer are not as preponderant in the results obtained, the drawback of this vibrometer lies in the fact that it uses a component that vibrates. Using this vibrating component requires ensuring that the speed remains constant and that all its various parts are always in perfect condition. However, this can be challenging to maintain, particularly over time, as normal wear and tear may affect its components.

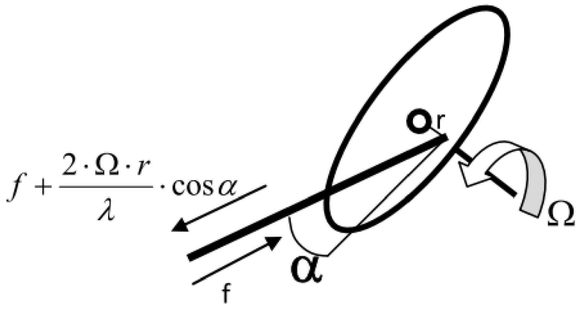

Figure 5.8: Frequency shift through a Rotating Diffraction Grating [56].

Finally, the Polytec LDV stands out. These vibrometers, in practice, are modified Mach-Zehnder vibrometers that use an electronic component called an Acousto-optic modulator instead of a Rotating Diffraction Grating. The use of this electronic component has resulted in more reliable results, and with advancements in technology, the component has become much more accessible. As a result, the Polytec LDV has become the most widespread vibrometer nowadays and is the one used for this experimental activity. In the following section, a more detailed discussion of this vibrometer will be provided [51].

5.4 Introduction of Polytec LDV

Considering that the Polytec LDV (see Figure 5.6(c)) will be the vibrometer used to conduct this activity, the analysis will begin with an individual examination of all its components to thoroughly understand its operation. Following this detailed analysis, the primary precautions to be taken will then be addressed while using it and discuss the main strategies to adopt in order to achieve better results.

5.4.1 Components of Polytec LDV

As you would expect, a Polytec LDV comprises several components, each serving a specific function. Below, the function of each component of this type of vibrometer will be explained:

- **Optical fiber**

  The Polytec LDV uses fibre optics to transmit the radiation emitted by the laser source. As can be seen in Figure 5.9, this material usually has a layer of glass fibre at its core.

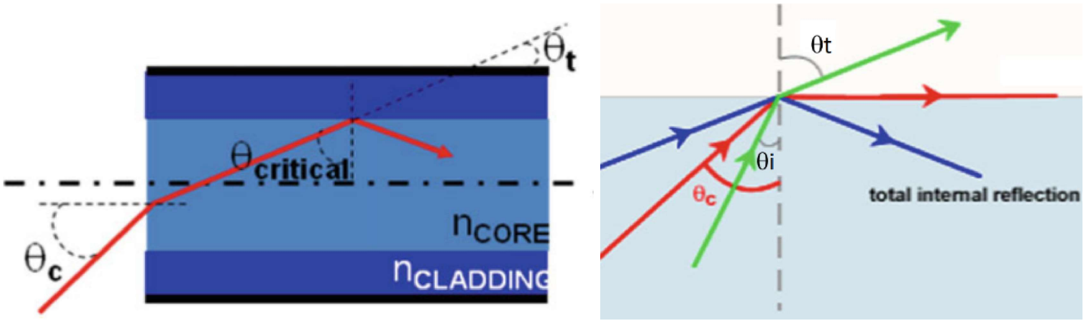

(a) Light propagation in a step-index optical fibre (b) Total internal reflection in optical fibre

Figure 5.9: Optical fibre representations[56].

This is the layer through which the radiation transmission occurs. The core is coated with a cylindrical layer of a material with a lower refractive index than the material used in the core. This detail is fundamental, because, as it is easy to understand, it is very important to ensure that all radiation leaving the light beam is reflected, i.e., that no portion of the emitted radiation is refracted. For this to happen, according to the equation of Snell-Descartes the refractive index of the second layer (n_t) must be lower than the refractive index of the core (n_i).

$$n_i \sin\theta_i = n_t \sin\theta_t \tag{5.18}$$

Given that $\theta_i = critical$ and that $\theta_t = 90°$:

$$\theta_{critical} = \arcsin\frac{n_t}{n_i} \tag{5.19}$$

Thus, if the radiation is emitted at an angle higher than $\theta_{critical}$, all the radiation emitted by the source will be reflected. Finally, it is worth noting the existence of a third layer, a layer whose sole purpose is to protect and coat the optical fibre itself [56].

- **Polarizing beam splitter (PBS)** e **Quarter wave plates ($\lambda/4$ plates)**

As mentioned earlier, the linear polarization of laser light is a phenomenon that ensures the dependence between the electric field and the wave itself, facilitating interference between the waves compared in the photodetector. Radiation sources with this characteristic often utilize Polarizing beamsplitters (PBS) and Quarter wave plates ($\lambda/4$ plates), as shown in Figure 5.10(b).

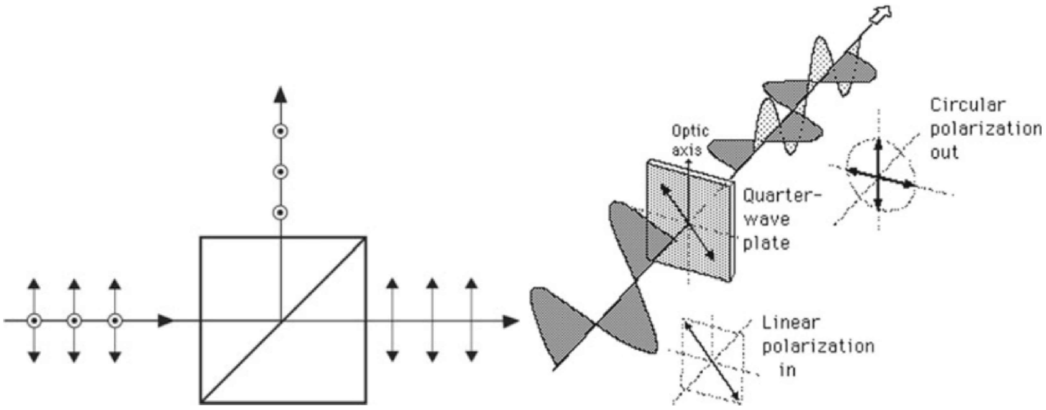

(a) Polarizing beam splitter (b) Quarter wave plate

Figure 5.10: Devices used when the radiation source is linearly polarized [56].

Starting by explaining the function of PBSs, these are peculiar radiation beam splitters, since as can be seen in Figure 5.10(a) the S part of the wave (orthogonal part) will always be reflected, while the P part of the wave (parallel to the plane) will always be emitted. Both parts will continue with the same amplitude.

The wave plates ($\lambda/4$) are used as optical isolators to prevent the light reflected by the target from taking the opposite path. These plates change the phase of the transmitted beam at $45°$ in relation to the beam parallel to the plane, as it passes through PBS_2 (see Figure 5.12), resulting in a circular configuration. When this beam collides with the vibrating beam and strikes the object under study, the reflected beam experiences a Doppler-induced frequency change and passes through the wave plate $\lambda/4$ once again. This time, the beam's phase undergoes a further shift, becoming $90°$ in relation to the incoming radiation at PBS_2. As a result, the beam passing through PBS_2 is now orthogonal to the plane and is reflected, ensuring that the radiation does not return. A schematic of the process is shown in Figure 5.11 [51, 56].

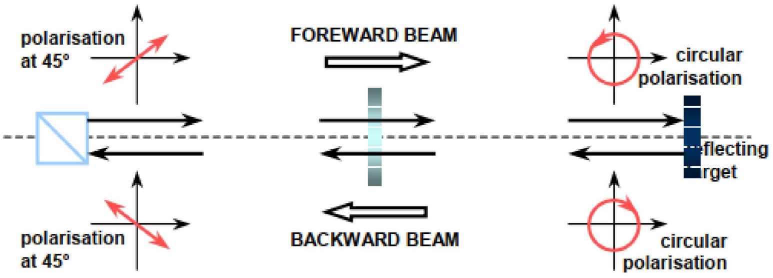

Figure 5.11: Quarter wave plate working principle [51].

- **Lens**

  Another component of great relevance that is present in the Polytec LDV is the front lens. This is true because the vast majority of surfaces are not specular, but rather diffuse, that is, the reflected radiation has a non-zero reflection angle. Thus, by using the front lens it becomes possible to collect radiation that had been scattered when the radiation was reflected.

Thus, it should be noted that with the introduction of this device, not only is it not necessary to pay special attention to the alignment of the laser with the vibrating surface under study, but the signal collected is significantly improved when studying objects with diffuse surfaces. However, with the use of front lenses, the amplitude of the beam passing through them will be smaller. Therefore, when the phenomenon of interference between the two beams occurs, this must be taken into account so that the final result is not compromised [56].

- **Acousto-optic modulator**
  This component is used to solve the problem already mentioned, namely that of the difficulty of measuring the almost negligible frequency shift caused by the Doppler effect of the radiation. Thus, this component, also called Bragg Cell (see Figure 5.12), applies a frequency shift of value f_B in the radiation that is reflected in the first PSB, which allows, as will be seen, to solve the problem in question.

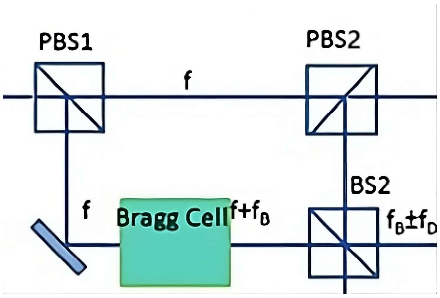

Figure 5.12: Radiation circuit with the introduction of a Bragg Cell [56].

Hence, in order to demonstrate that the introduction of this device solves the mentioned problem, let's start by noting that the electric field (E_{TOT}) observed in one of the photodetectors is obtained by the following expression:

$$E_{TOT} = R \cdot e^{j[(\omega+\omega_B)t-\theta_1]} + S \cdot e^{j[(\omega\pm\omega_D)t-\theta_2]} \tag{5.20}$$

It should be noted that R and S represent the values of the amplitudes of the two beams and that these amplitudes will assume different values. This variation occurs because the Polytec LDV uses a front lens, as previously mentioned, which decreases the amplitude of the radiation passing through it. It is important to note that the output of a photodetector is proportional to the square modulus of the electric field of the incident radiation (Re represents the real part and Im represents the imaginary part):

$$I \propto \left|E_{TOT}^2\right| = (Re)^2 + (Im)^2 \Leftrightarrow$$

$$\Leftrightarrow \left|E_{TOT}^2\right| = \left\{[R\cos\left((\omega+\omega_B)\,t-\theta_1\right) + S\cos\left((\omega\pm\omega_D)\,t\right)-\theta_2]^2\right\} +$$

$$+\left\{[R\sin\left((\omega+\omega_B)\,t-\theta_1\right) + S\sin\left((\omega\pm\omega_D)\,t\right)-\theta_2]^2\right\} \Leftrightarrow$$

$$\Leftrightarrow I \propto \left|E_{TOT}^{2}\right| = \left\{\left[R^{2} + S^{2} + 2RS\cos\left(\left(\omega_B \pm \omega_D\right)t + \theta_2 - \theta_1\right)\right]\right\} \tag{5.21}$$

As can be observed, the angular frequency of the wave emitted in the radiation source, has disappeared. Thus, it can be seen that the photodetectors will be able to analyse these angular frequencies because ω_B and ω_D assume significantly lower values compared to ω.

Finally, it is worth noting that, if the speed of the object under study is positive, the frequency is given by $f = f_B + f_D$, and if it is negative, the frequency is given by $f = f_B - f_D$. Thus, it is then proven that introducing a Bragg Cell in the circuit of the Polytec LDV can overcome the problem mentioned above [56].

- **Photodetectors** and **Differential Amplificator**

The presence of two other components in the Polytec LDV must be highlighted: the photodetectors and the differential amplifier (refer to Figure 5.13) [51, 56].
Starting with the photodetectors, it should be noted that it is in these components that the phenomenon of interference between the two radiation waves occurs, allowing for the measurement of the desired physical magnitude. The outputs of these devices can be written as follows:

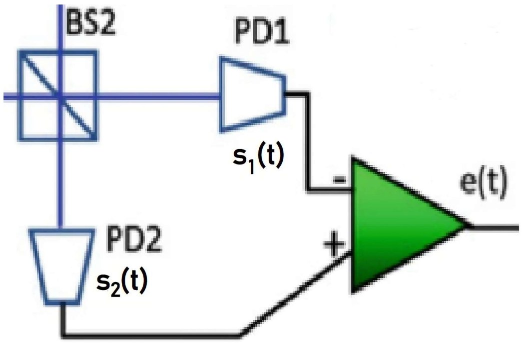

Figure 5.13: Photodetectors and Amplifier scheme [56].

$$PD_1 \quad \Rightarrow \quad s_1(t) = \left\{\left[R^{2} + S^{2} - 2RS\cos\left(\left(\omega_B \pm \omega_D\right)t + \theta_2 - \theta_1\right)\right]\right\} \tag{5.22}$$

$$PD_2 \quad \Rightarrow \quad s_2(t) = \left\{\left[R^{2} + S^{2} + 2RS\cos\left(\left(\omega_B \pm \omega_D\right)t + \theta_2 - \theta_1\right)\right]\right\} \tag{5.23}$$

It should also be noted that the Polytec LDV utilizes a differential amplifier, which plays a crucial role in eliminating some of the noise obtained from the photodetectors. As a result, the introduction of this device significantly improves the response obtained, given by the following expression [56]:

$$e(t) = A(s_2 - s_1) = 4RS\cos\left(\left(\omega_B \pm \omega_D\right)t\theta_2 - \theta_1\right) \tag{5.24}$$

5.4.2 Limits of the Polytec LDV

As expected, this technology presents certain inherent uncertainties that warrant attention, even though it typically produces satisfactory results.

One significant uncertainty to be highlighted is related to the laser radiation emission source. Although this uncertainty is generally not considerable, it must be taken into account, and typically, the

LDV manufacturer provides information about the potential wavelength variation. Additionally, the optical components that form the LDV also introduce associated uncertainties, which should not be overlooked, as they collectively impact the wavelength variation of the laser beam [25].

Another noteworthy limitation of this technology, particularly crucial in modal analysis, is the misalignment of the laser beam concerning the component due to velocity. When the object under study exhibits only an out-of-plane velocity component, the beam misalignment issue becomes relatively easier to address, owing to the greater ease of aligning the laser beam, as illustrated in Figure 5.14.

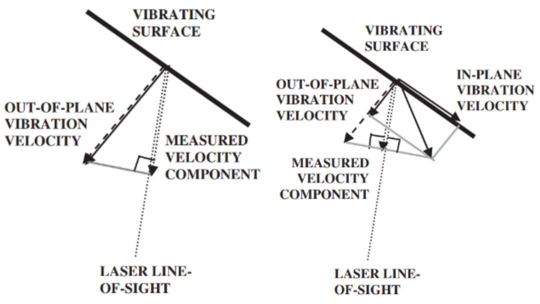

(a) Out-of-plane (b) Partially in-plane

Figure 5.14: Representation of the velocity component measured by an LDV for different types of vibrations [25].

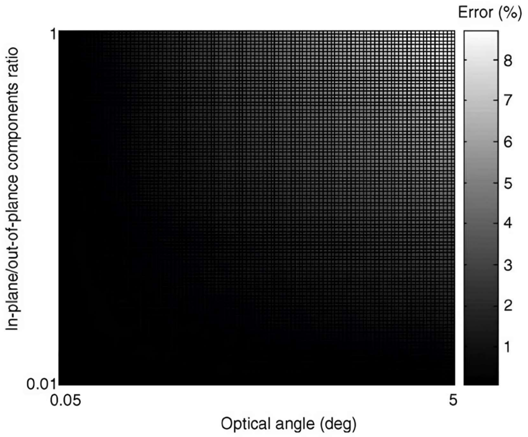

Figure 5.15: Error due to optical path misalignment with respect to surface velocity and ratio between in-plane and out-of-plane components [25].

However, when the structure exhibits in-plane vibration velocity (a common occurrence at various resonance frequencies), this problem becomes more challenging to address and can significantly impact the obtained results, as illustrated in Figure 5.15. Consequently, it is crucial to emphasize the necessity for special attention in studying flexural resonance frequencies along the y axis [25].

It is important to highlight that all Polytec lasers, despite incorporating a front lens, have an optimal measuring distance. This distance is specified by the device manufacturer and must be carefully consulted and strictly adhered to in order to avoid experimental errors. This limitation is particularly critical when studying aeronautical components, as they often feature surfaces with colors that impede light diffusion. However, this can be overcome by applying a reflective coating on the structure's surface that will interact with the laser light [56].

Lastly, it is crucial to mention that the activity should not be conducted in environments with high dust levels. The presence of dust particles can significantly alter the refractive index of the air, leading to substantial experimental errors [60].

5.4.3 Strategies to improve Polytec LDV results

Over time, various strategies have been studied and developed to enhance the outcomes obtained with this technology. As previously mentioned, one of the primary challenges affecting results is the necessity to use LDVs in environments with adverse conditions, resulting in noisy responses. To address this issue, LDV manufacturers have improved the devices' software by implementing windowing techniques [61] and simple interpolation techniques of results [62]. These techniques have proven highly effective in noise reduction. Moreover, it has been observed that longer measurement durations also serve as an effective approach to mitigate such noise [25].

Another effective strategy is ensuring a proper focusing of the light beam before each measurement is essential to enhance the obtained results. Although this process can be time-consuming, it yields significant improvements in response, especially for surfaces that present challenges in light diffusion. In modern LDVs, there is also the option of having the instrument itself perform the focusing task, which proves highly advantageous, as it can achieve more precise focusing compared to relying solely on the human eye.

It is also worth noting that, in order to enhance the obtained response, LDVs often offer the option of measuring the Signal-to-Noise Ratio (SNR) with the device itself. If the SNR obtained is excessively high, the LDV disregards the response and slightly adjusts the beam's position until it achieves a response with a reasonable SNR value. However, this strategy may require spending additional time to obtain a low noise response (with a low SNR value) [25].

It is also important to highlight a strategy that was very well studied at the end of the '90s ([63, 64]) and which is now very well founded and which largely explains the success of the LDV, namely, **Multipoint measurements** (see Figure 5.16). As the name itself indicates, this idea involves measuring a set of points at the same time (usually, the devices in question measure a set of 16 or 32 points). Using this strategy, all transient events can be measured more effectively and with greater accuracy, since 16/32 measurements can be taken in a single instant of time. Also, as expected, utilizing **Multipoint measurements** allows for a significant reduction in the time required to carry out any experimental activity. This factor is crucial because it allows us to minimize the impact of all the other strategies mentioned above, strategies which, as has been mentioned, imply the need to spend more time on their implementation. It should be noted that, as this strategy involves the installation of several optical components, it is not always an economically viable solution. Consequently, not all LDVs, including the one used for this laboratory activity, are able to implement this approach.

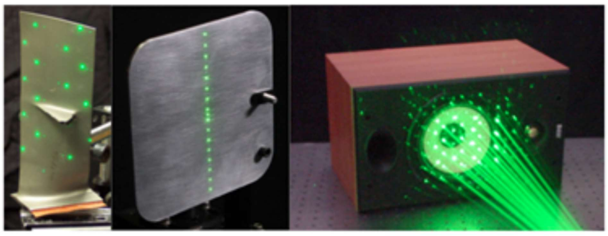

Figure 5.16: Example of multipoint measurements on linear and square pattern [65].

Finally, it is worth mentioning that various studies have shown significant improvements in results when the front part of the LDV (the head of the device) is isolated. This isolation helps mitigate the influence of environmental conditions on the experiment, leading to more accurate and reliable measurements [60].

Chapter 6

Experimental Procedures

Before beginning the experimental analysis, the experiment preparation was carried out. All the procedures, which will now be described, were conducted in the LAQ-AERMEC Aeromechanical Structural Systems, Laboratory of the Department of Mechanical and Aerospace Engineering at Politecnico di Torino.

Thus, the first step was to define the configuration of the measured points on the beams under study. In fact, this task is quite relevant in the study that will be pursued, as explained in the theoretical foundations, the FRF graphs show significant differences and vary from point to point.

Once the configuration of points to be experimentally measured was determined, the beams were prepared for examination using the LDV. Additionally, the emitted light beam from the LDV was verified to ensure proper reflection from the beams under study.

Subsequently, great care was taken during the assembly of all devices involved in conducting this laboratory activity. All procedures adopted for the completion of these assemblies will also be addressed in this current chapter.

6.1 Configuration of points to be measured

Starting by explaining the configuration of the selected points, it was established that to understand the potential of the frequency measurement method using the laser vibrometer, the experimental activity, as mentioned in Chapter 4, should focus on studying all modal forms up to the 5^{th} flexural.

Another aspect taken into consideration when selecting the measurement point configuration is that it should assist the LDV software in representing the modal shapes. Thus, as seen in Figure 4.3, both the flexural and torsional modal shapes exhibit a parabolic behaviour along the x-axis. Consequently, if only the respective maximum and minimum points of each modal shape were selected, it could result in a representation of motion in straight lines, which might not adequately convey the parabolic behaviour of these modal shapes.

Regarding the choice of measurement point configuration, it is worth noting that the laser does not incorporate the aforementioned Multipoint Measuring strategy, which, as mentioned, would allow more than one point to be measured simultaneously, thereby reducing the time required to carry out the experimental activity. Given that there was a limited amount of time available for this laboratory activity and considering that the greater the number of selected points, the more time the laser would require to perform the experimental activity, the choice in question required a compromise between quality and optimization of time for the implementation of the activity at hand.

Taking all of this into account, the chosen measurement point configuration is represented in Figure 6.1

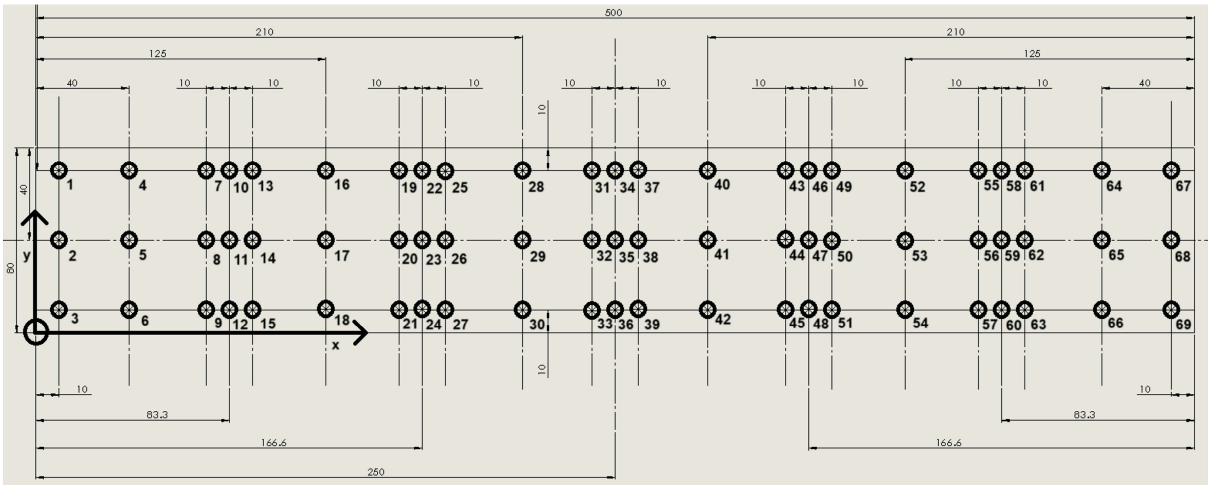

Figure 6.1: Point configuration chosen to take measurements.

This was the point configuration chosen to be implemented, as considering what has been previously mentioned, higher-order modal shapes are more difficult for software to predict. Therefore, since the highest modal frequency studied was the 5^{th} flexural mode, priority was given to this modal shape. Thus, starting on the *y-axis* of symmetry, points were placed to measure the maximum displacements for this specific modal shape, that is, the $11,\ 23,\ 35,\ 47,\ 59$ points. Then, $8,\ 14,\ 20,\ 26,\ 32,\ 35,\ 44,\ 50,\ 56,\ 62$ points were placed near the maximum displacements to assist the software in describing the aforementioned parabolic behaviour of the modal shapes. Two measurement points were also placed at the ends (points 2 and 68), and one intermediate point between each maximum of the 5^{th} flexural modal shape (points $5,\ 17,\ 29,\ 41,\ 53,\ 65$). These last points correspond to the nodes (see Chapter 2.4.2) of this modal shape. In fact, this strategy, as observed downstream, proved to be effective in representing all flexural modal shapes. This occurred because not only some of these 23 points are also minimum and maximum points of previous flexural modal shapes, but also because it is expected that 23 points are already a significant number, capable of representing flexural modal shapes of lower orders.

Having said that it should be noted that, with all the points mentioned so far, it would not be possible to obtain torsional frequencies and their respective modal shapes. This is because these points are on the $y - axis$ of symmetry, which is a nodal line for all torsional modal shapes as can be seen in Figure 4.3. Therefore, to overcome this problem, the same line of points was replicated 30 cm up and 30 cm down. This option solves the mentioned problem because, except for the first torsional modal shape all other torsional shapes share the same transverse nodal line as the lower-order flexural modal shape. For example, the 2^{nd} torsional modal shape shares the same transverse nodal line present in the 1^{st}

flexural modal shape (see Figure 4.3).

Consequently, if that line of points was capable of correctly representing all flexural modal shapes up to and including the 5^{th} order, by reflecting that same line of points upwards and downwards, the correct representation of the first 6 torsional modal shapes could be achieved. This is quite positive because, as observed in the numerical analysis, none of the 4 beams have the 6^{th} torsional shape preceding the 5^{th} modal shape. It should also be noted that it was decided to replicate that line of points both in the positive and negative direction of the $y-axis$ so that the software could more explicitly represent all the torsional modal shapes in question.

The configuration represented in Figure 6.1 was used for all the beams in question because although the frequencies at which the modal forms occur vary from beam to beam, as well as their succession (sometimes the torsional forms precede the flexural forms), because, as mentioned above, the position of all the nodal lines is common to all modal forms of all the beams under study.

6.2 Procedures carried out on the beams

After selecting the point configuration to be used for the experimental analysis, the preparation of the beams themselves was carried out. As these beams were not built exclusively for this experiment and had already been used for other experiments, it was necessary to clean them. After this cleaning, the points in Figure 6.1 were marked on the beams under study.

After marking the point configuration, a simple test was conducted to determine if the aluminium surface would be able to reflect laser light effectively. This concern arose because, as noted in Chapter 5.4, one of the major disadvantages of these methods for acquiring results is that aeronautical surfaces are usually unable to reflect light effectively. Thus, through this simple test, it became apparent that these sandwich beams were no exception. Proceeding with the experiment with the bars in that state would compromise the reliability of the results. Therefore, it was necessary to apply a small reflective tape only at the points where measurements were to be taken. The application of this reflective tape can be seen in Figure 6.2.

With the application of this reflective tape, it was observed that the LDV could capture the signal from the beam satisfactorily, allowing the experiment to proceed (see Chapter 5.4.3).

6.3 Structure assembly

With the bars ready, the process of assembling the structure for this laboratory activity began. This structure, as can be seen in Figure 6.2, is a square metal structure with circular through holes. Using these through holes, the structure was attached to a specific table for this purpose using screws and nuts.

In order to connect the bars under study to this metal structure, various methods were tried. Since the objective of this activity was to study the beams in the **Free-free condition** situation (see Chapter 5.1.3), the most suitable configuration would be the one that introduces the least rigidity into the system under study. In Figure 6.2 it is possible to see the different ways of connecting the bars to the metal structure that were experimented with.

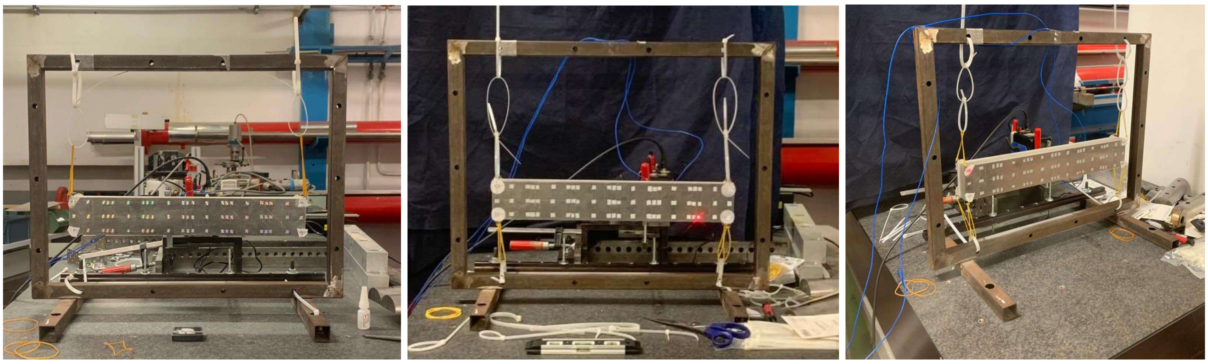

(a) 1^{st} **configuration**- 2 plastic straps and 1 elastic band) (b) 2^{nd} **configuration**- 3 plastic straps and no elastic band (c) 3^{rd} **configuration**- 3 plastic straps and 1 elastic band

Figure 6.2: Different configurations tested for carrying out the experimental activity.

As shown in Figure 6.2, none of the three presented configurations allow the beams under study to move along the y-axis. Thus, due to the impossibility of achieving a perfect study of the beams under **Free-free condition**, it was necessary to disregard flexural modal shapes in that plane.

With this in mind, given this constraint, an effort was made to choose the configuration that minimized stiffness in the directions where the beams could move. Consequently, after experimenting with the different configurations mentioned earlier, it was concluded that the presence of elastics was more beneficial for achieving this goal. Thus, the 1^{st} configuration in Figure 6.2 was excluded. On the other hand, a higher number of plastic straps allowed the elastics to be subjected to lower tension, thereby minimizing stiffness. For this reason, the 3^{rd} configuration in Figure 6.2 was the chosen setup for the execution of this work.

Finally, the last aspect that was ensured in this part of the experimental procedure was the horizontality of the beams under study. This horizontality was verified using an inclinometer and is actually an aspect of great relevance since the lack of this factor could lead to significant discrepancies between the support points of the beams, given that the stiffness would not be equal at these points.

6.4 Shaker assembly

To apply the force to the structures under study, as previously mentioned, a *Model K2007E01* shaker was used, as shown in Figure 6.3. In this way, after assembling the entire structure, the process of connecting the Shaker to the same table where the rest of the structure was located began, using screws and nuts. After that, the tip of the *Model K2007E01* arm was connected to the beam, as can be seen in Figure 6.4. This connection was made at approximately 350 cm from the *x-axis* origin and 25 cm from the *y-axis* origin (see Figure 6.1 for better comprehension), with special care taken to avoid any bending of the shaker arm. Avoiding this bending effect entails avoiding the point where this connection occurs and becomes another point of support, thereby minimizing the additional stiffness that this component could introduce in the structure. Note that this support effect by the Shaker was studied, but both the results obtained and the respective conclusions will be explained in Chapter 7.

Figure 6.3: Shaker *Model K2007E01* that was used in this experiment [66].

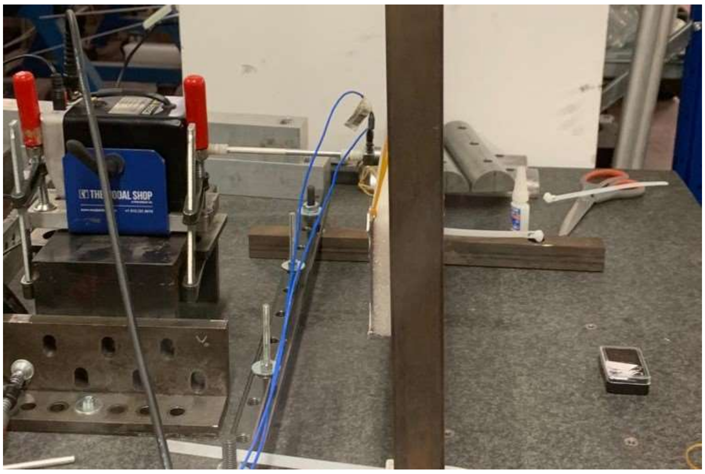

Figure 6.4: Assembly of the shaker in the structure under study.

After the Shaker was mounted, a small verification of its connection to the structure under study was carried out. To perform this verification, a low-frequency sinusoidal force (e.g. 10 Hz) was applied and the input and output signals were analysed. When these signals are perfect sine waves, it means that the connection was successful, and the experiment can continue.

6.5 Laser assembly

The last stage of preparation for this activity involved the assembly and preparation of the laser for the experimental activity.

Firstly, a dark cloth was placed behind the entire structure under study in order to reduce ambient light. Then, the user support document for this device was consulted to determine the optimal distance for positioning the laser [67]. Thus, upon analyzing Figure 6.5, it becomes clear that there are several optimal distances – that is, distances allowing the LDV to capture the laser light beam most effectively. The first occurs at 141 mm, and all other optimal distances follow by adding 204 mm. Therefore, considering the available space in the laboratory, the decision was made to position the LDV at 1365 mm, i.e., at the 7^{th} optimal distance $(141 + 204 \times 7)$. To perform this task with greater precision, a laser distance meter was used.

Once the laser was positioned, the software program for the device was started and the measurement observed with the laser distance meter was entered. After this, the camera optics of the laser were opened in order to visualize, in the software, the beam that was going to be used. Then, there was a need to enter into the software all the points that were to be measured, that is, the points where the adhesive tape was applied.

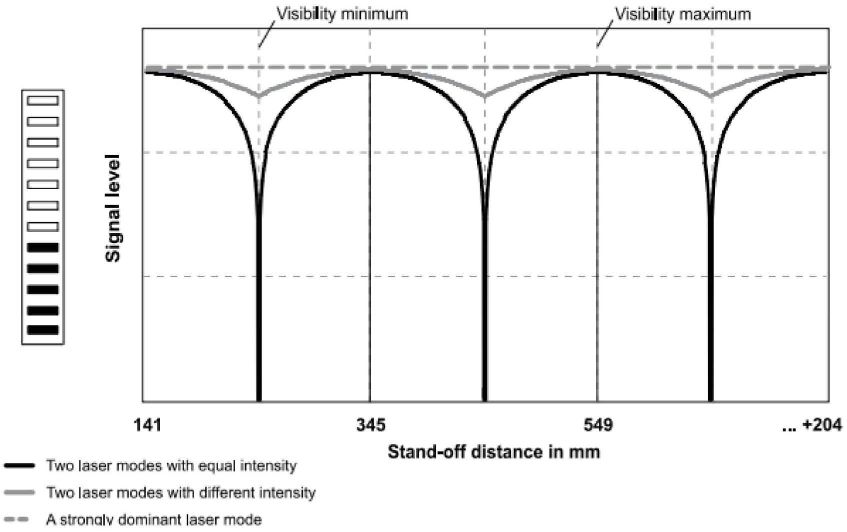

Figure 6.5: Relation between stand-off distance and signal level [67].

For each of the points, care was taken to ensure not only its alignment but also to ensure that the signal that the laser was capturing at each of these points was at its maximum. This was not always possible on the first attempt because although the adhesive tape provided a good reflection of the laser light, it had, in some cases, small deformations that compromised the quality of the signal.

After making these small adjustments, the 2D assignment was carried out, meaning the laser itself was employed to interpret the points intended for measurement so that it could then perform an auto-focusing process in order to improve the results, as described in Chapter 5.4.3.

Finally, to optimize the time required for the execution of each test, a 500 Hz high-pass filter was applied. This choice was influenced by the observation from the numerical analyses that the first frequencies of interest for our numerical study appeared around 700 Hz. Additionally, a low-pass filter of 4000 Hz was applied, as the intention was to study all modal forms up to the 5^{th} flexural modal shape, and the 5^{th} modal shapes appeared around 3000 Hz for all the beams under investigation in our numerical study. As you will observe in Chapter 7, these filtering strategies did not have any negative consequences for this work, because no experimental modal form appeared before 500 Hz, and none of the 5^{th} flexural modes exceeded 4000 Hz.

With this in mind, with the implementation of all these strategies the LDV only required approximately 2 hours to conduct each of the experimental tests.

Chapter 7

Results

In this chapter, all the results obtained will be presented and discussed. In this first part, some fundamental details for understanding the nature of this data and the way it will be treated will also be addressed.

The results obtained regarding the coherence of the experimentally acquired data for each of the studied beams will be disclosed initially. In this way, as was observed in Chapter 5.1.4, this analysis will allow us to draw conclusions about the quality of this data.

After this, an analysis of the obtained modal shapes will be carried out, that is, it will be verified if they resemble those obtained by computational methods. After that, for each of the beams, an analysis of the FRF graphs of some previously selected points will also be carried out. Also in this section, the results obtained regarding the MAC analyses conducted for the different beams will be presented and discussed.

To conclude this chapter, the experiment conducted in parallel with the main experiment using an Impact Hammer (*Model T086C03* [68]) will also be addressed. This will lead to the conclusion of whether the Shaker used to excite the structures under study indeed adds significant stiffness to the structure, and if so, whether this significantly compromises the results obtained.

7.1 Previous considerations

Initially, it's important to recall, as mentioned in Chapter 6.4, that due to the limitations of the structure used to assemble all components of this activity, the Shaker had to be fixed at 350 cm from the origin of the x-axis and 25 cm from the origin of the y-axis (see Figure 6.1). However, after a meticulous examination of the numerically obtained graphical representations (see Figure 4.3), it was found that it is likely that this point is a node for the 4^{th} flexural modal shape. Therefore, if this is confirmed experimentally, and considering what was explained in Chapter 2.4.2, this fact could have a significantly negative impact on the results obtained for this modal shape. Another issue that should be mentioned is the possibility that the beams under study may not be free from deformations or even manufacturing defects. Therefore, this can be another external factor to consider that may negatively influence the results to be presented.

It's also important to note that for each of the selected points (see Figure 6.1), the LDV performed between 30 to 50 measurements, and the final FRF graph for each of these points is the average of all these measurements. To predict the modal shapes, the LDV uses the final FRF graphs from each of the selected points and averages all these graphs. This average representation will be reproduced downstream and is from which the experimental natural frequencies of the structures under study were defined (see Figures 7.2, 7.11, 7.20 and 7.29). It is also from these average transfer functions that coherence functions, analyzed in Chapter 7.2, will be calculated.

In addition, in the analysis of the results, numerical transfer functions will also be compared with other experimental ones from 3 specific points. Thus, in order to study the similarity between these functions, the following points from Figure 6.1 were chosen for this study:

- **Point 1**: From the analysis of the graphical representations in Figure 4.3, it is expected that this point is not a node for any of the modal shapes under study. Therefore, it should be possible to observe all the peaks relative to all the modal shapes under study;
- **Point 2**: From the analysis of the graphical representations in Figure 4.3, it is expected that this point is a node for all the torsional modal shapes. This occurs because all torsional modal shapes have a longitudinal nodal line along the y-axis of symmetry. Thus, it is expected that in the transfer functions related to this point, only the frequency peaks relative to the flexural modal shapes can be visualized;
- **Point 36**: From the analysis of the graphical representations in Figure 4.3, it is expected that this point is a node for all the antisymmetric modal shapes, namely, 2^{nd} and 4^{th} flexural and 1^{st} and 3^{rd} torsional. Therefore, it is expected that in the transfer functions related to this point, only the frequency peaks relative to the symmetric modal shapes can be visualized.

To collect the experimental data in order to proceed with the construction of FRF graphs for these specific points, it was necessary to use a function called *readuff* [69]. The use of this function was essential because it allows MATLAB to read universal files (.unv), which is the file format used by the LDV software to store the calculated data.

To construct numerical FRF graphs for these points, some intermediate steps were required since Patran/Nastran does not provide them directly. Therefore, a file with the modal vectors relative to the displacement of those points was downloaded from this software. Then, a file capable of reading and extracting these values was created using MATLAB (see Appendix A).

Afterward, Equation 2.64 was used. It's important to note that since Patran/Nastran only provides displacement-related responses, and the LDV used measures velocity-related responses, it was necessary to multiply Equation 2.64 by $j\omega$, as explained in Chapter 2.4. It's also worth mentioning that in Equation 2.64, the constant M_k was assumed to be unity since it was decided to normalize the response with respect to mass (see Chapter 2.4.2). As for the values of the constant ζ_k in Equation 2.64, these were estimated through the procedure outlined in Chapter 2.3. However, special attention must be paid to this detail because Nastran calculated these resonance frequency values assuming the condition of Force Vibrations for undamped systems (see Chapter 2.4.2), as initially, this constant is often unknown. Thus, by introducing values for ζ_k, the frequency peaks will be slightly lower, as explained in Chapter 2.2.3 and in cases where the frequency peaks are too close, they may blend together.

To make this comparison more effective, both the numerical and experimental transfer functions were made dimensionless by dividing by their respective maximum values. This results in dimensionless plots, ranging in this particular case from 0 to 1. All the files with the MATLAB codes produced for this work can be found in the Appendices A and B.

Finally, to compare the differences between the frequencies obtained for the modal shapes in numerical and experimental models (dif), Equation 7.1 was utilized. Here, f_{FE} denotes the frequencies from the numerical model, and f_{Exp} denotes the frequencies from the experimental model.

$$dif = \frac{f_{FE} - f_{Exp}}{f_{FE}} \times 100 \tag{7.1}$$

This difference between models, as can be observed from Equation 7.1, was calculated concerning the results obtained numerically. This is because only numerically can the free-condition be simulated, a strategy observed in other modal analyses [3].

7.2 Evaluation of the quality of results

That being said, the coherence plots obtained for the tests that will be used for data analysis can be observed in Figure 7.1.

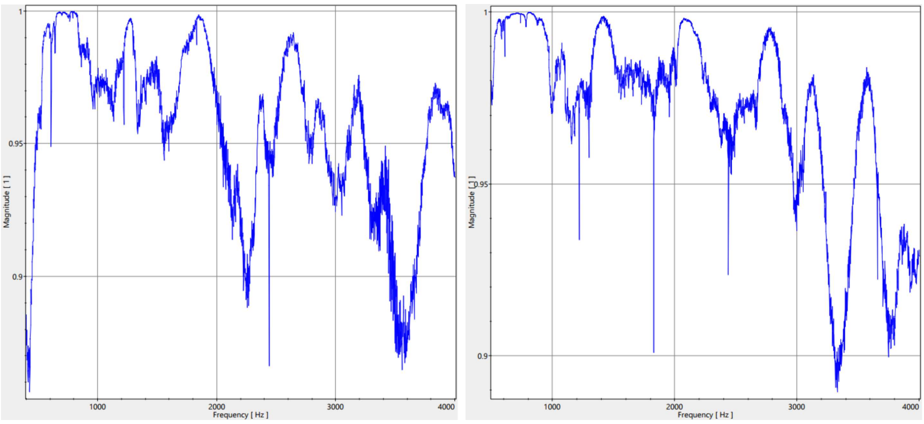

(a) Graph obtained for coherence for beam D01 (b) Graph obtained for coherence for beam D02

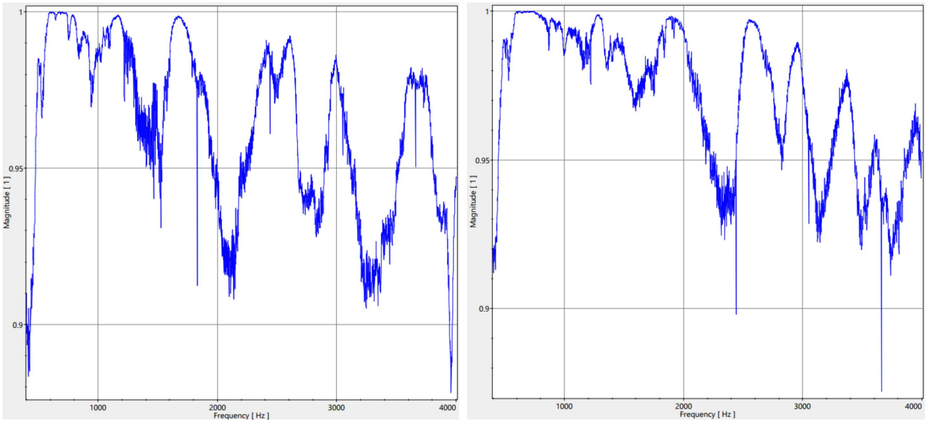

(c) Graph obtained for coherence for beam D03 (d) Graph obtained for coherence for beam D04

Figure 7.1: Graphs obtained for the average coherence of all the experimental tests that will be analysed

As can be observed from the analysis of the graphs in Figure 7.1, all experimental tests exhibited good coherence values. Despite some oscillations, especially at anti-resonance frequencies, the coherence function always assumed values close to 1, and the minimum values were never below 0.85.

Therefore, it can be stated that for none of the tests, the existing noise significantly affected the results obtained. Consequently, the analyses that will be performed next should be a fair representation of the reality under study.

7.3 Analysis of the D01 beam

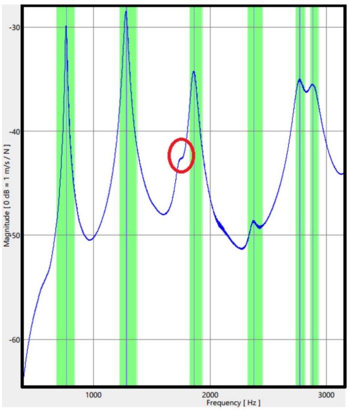

Figure 7.2: Graph showing the frequency peaks for which LDV was able to predict the modal shapes of the D01 beam.

Frequency peaks	Peak values [Hz]	ζ [%]
1^{st}	767.5	0.68
2^{nd}	1280	1.71
3^{rd}	1862.5	1.68
4^{th}	2377.5	1.81
5^{th}	2768.75	1.81
6^{th}	2880	2.19

Table 7.1: Frequency peaks to be analysed and the Damping factor for beam D01.

From the observation of the graph in Figure 7.2, it can be seen that the LDV probably wasn't able to predict a modal shape for a possible frequency peak around 1700 Hz (see the red circle in Figure 7.1). However, in the subsequent analysis of the selected points, it will be studied whether this possible frequency peak corresponds to a modal shape. In Table 7.1, all the frequency peaks recognized by the LDV and for which it was able to predict modal shapes are listed. These graphical representations for modal shapes were extracted from the animations generated by the LDV software and can be seen in Figure 7.3 and each of these peaks will be analysed individually.

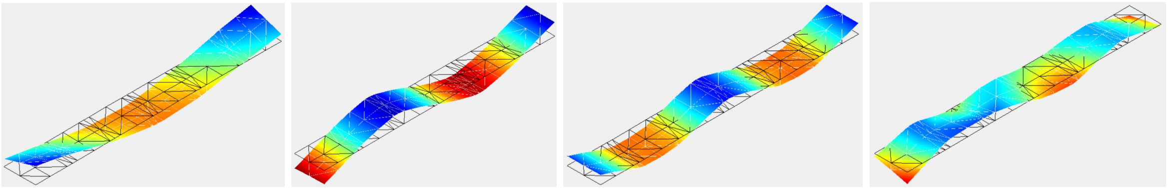

(a) Graphic representation for 767.5 Hz.

(b) Graphic representation for 1280 Hz.

(c) Graphic representation for 1862.5 Hz.

(d) Graphic representation for 2377.5 Hz.

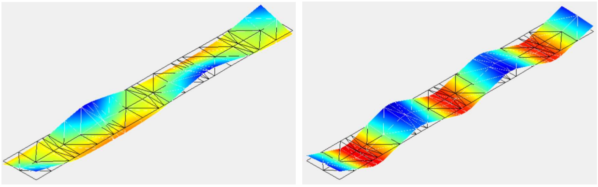

(e) Graphic representation for 2768.75 Hz.

(f) Graphic representation for 2880 Hz.

Figure 7.3: Graphical representations obtained for the modal shapes for beam D01.

- 1^{st} **frequency peak (767.5 Hz)**- By observing Figure 7.3(a), this frequency peak may correspond to a **flexural-torsional mode**, which results from the combination of the 1^{st} flexural and 1^{st} torsional modes. This observation is more evident in the animation produced by the software from which this Figure was taken. Thus, it is noted that numerically, as can be seen in Table 4.3, the 1^{st} torsional and 1^{st} flexural modes are separated by only approximately 10 Hz, a difference that may have been quite difficult to discern experimentally;
- 2^{nd} **frequency peak (1280 Hz)**- From the observation of Figure 7.3(b), it is possible to perceive that this frequency peak may correspond to the 2^{nd} **flexural numerical mode**. Additionally, through the animation, it becomes clearer that this mode may represent a second-order flexural shape;
- 3^{rd} **frequency peak (1862.5 Hz)**- By observing Figure 7.3(c), it is possible to notice that the frequency peak may represent the 3^{rd} **flexural numerical mode**. However, through the observation of the animation, it exhibits some torsion despite being a flexural mode. This may be justified because the 2^{nd} torsional mode may have been suppressed, i.e., it may correspond to the small frequency peak that seems to exist and that the LDV was not able to recognize (see the red circle in Figure 7.2). It should also be noted that the 3^{rd} flexural and 2^{nd} torsional numerical modes are separated by only about 50 Hz (see Figure 4.3), a difference that is also not very significant and therefore may have been difficult to verify experimentally;
- 4^{th} **frequency peak (2377.5 Hz)**- Although Figure 7.3(d) is not very clear, but it can be seen through the animation that it may represent the 4^{th} **flexural numerical mode**. The difficulty in visualizing this mode is likely due to the position of the shaker, a problem that was mentioned previously;
- 5^{th} **frequency peak (2768.75 Hz)**- Although Figure 7.3(e) is not very clear, it may represent the 3^{rd} **torsional numerical mode**. The low clarity of this mode shape (which is quite noticeable when viewing its animation) is related to the fact that this torsional mode has a small fraction of flexion. This can be justified by the fact that both numerically and experimentally this mode shape is very close to the 5^{th} flexural mode;
- 6^{th} **frequency peak (2880 Hz)**- This frequency peak may represent the 5^{th} **flexural numerical mode**. However, it is possible to observe that it also exhibits some torsion, which can once again be justified by the numerical proximity between the 5^{th} flexural mode and the 3^{rd} torsional mode (see Table 4.3).

The following table summarizes all the information and presents the differences between the two analyzed models, namely the numerical model and the experimental model. However, it is important to note that whenever two numerical modal shapes gave rise to a single experimental modal shape, the difference between the models was calculated using the numerical modal shape that best represented the experimental modal shape obtained. For example, for the 1^{st} modal shape obtained for beam D01, which is a flexo-torsional modal shape, it was considered that the numerical modal shape that best represented it was the 1^{st} flexural modal shape, since flexure is more predominant than torsion in this case. This reasoning was applied to all the beams studied.

Table 7.2: Results obtained for the modal forms of beam D01.

numerical modal forms		**experimental modal forms**		**differences between models (%)**
modal shape type	frequency of the modal form [Hz]	modal shape type	frequency of the modal form [Hz]	
1^{st} torsional	704.97	1^{st} flexu-torsional	767.5	6.81
1^{st} flexural	715.22			
2^{nd} flexural	1169.4	2^{nd} flexural	1280	9.46
2^{nd} torsional	1602.4			
3^{rd} flexural	1669.8	3^{rd} flexural	1862.5	11.54
4^{th} flexural	2101.5	4^{th} flexural	2377.5	13.12
3^{rd} torsional	2538.1	3^{rd} torsional	2768.75	9.09
5^{th} flexural	2589.2	5^{th} flexural	2880	11.23

By observing the Table 7.2, it is easy to see that, despite not having verified the modal shape corresponding to the second torsional mode, the experimental modal shapes follow the same order as the numerical ones. It should also be noted that the differences between models are significant but more or less constant, within a range of 6.81% to 13.12%. Also, before moving on to the analysis of the FRF graphs for the selected points, it's important to emphasize that since the LDV did not identify the 2^{nd} torsional mode, it was not possible to obtain a value for ζ of the resonance frequency corresponding to this modal shape. However, given that it is very close to the 3^{rd} flexural mode, it was assumed that the ζ for the 2^{nd} torsional mode is the same as that for the 3^{rd} flexural mode. Furthermore, it is noted that this kind of approximation was made for the other beams in cases similar to the one just described.

7.3.1 Analysis of FRF plots of selected points for beam D01

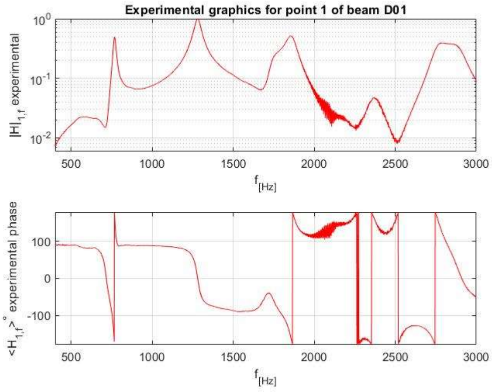

Figure 7.4: Experimental FRF for point 1 of beam D01.

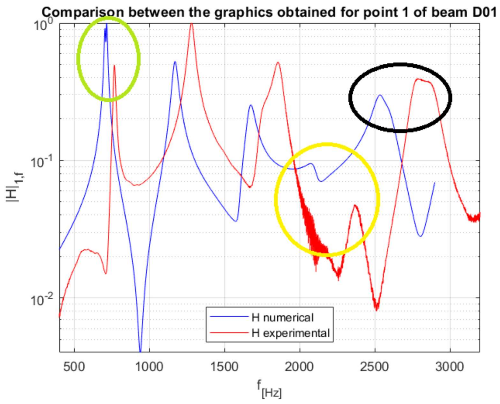

Figure 7.5: Comparison of numerical and experimental FRF for point 1 of beam D01.

Firstly, by analyzing Figures 7.4 and 7.5, it can be seen that Point 1, as expected in Section 7.1, does not correspond to any node for any of the analyzed modal shapes, as all frequency peaks related to them can be seen in the previous graphs. Furthermore, it is important to highlight that, as seen in Figure 7.5, the numerical and experimental FRF plots have a similar trend, with the frequency peaks of the numerical model appearing earlier than those of the experimental model. It is also evident that the 4^{th} flexural modal shape, as suspected, is not significant both numerically and experimentally (see the yellow circle in Figure 7.5). Additionally, the lack of clarity observed in the 3^{rd} torsional modal shape and 5^{th} flexural modal shape may be due to a mixture of these modal shapes in both numerically and experimentally obtained Frequency Response Functions (FRFs) (see the black circle in Figure 7.5).

Regarding the 1^{st} flexural and 1^{st} torsional modal shapes, although two close but distinct frequency peaks can be observed in the numerical FRF, this is not the case in the experimental FRF, which can explain the identification of a 1^{st} flexo-torsional modal shape (see the green circle in Figure 7.5).

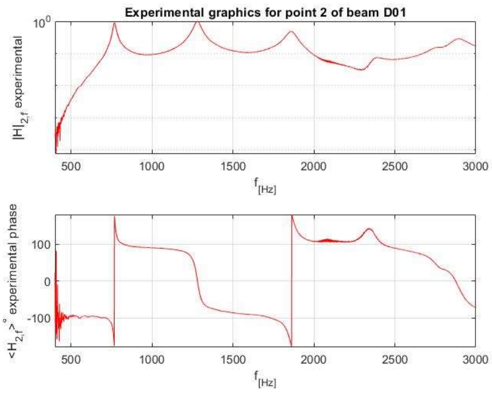

Figure 7.6: Experimental FRF for point 2 of beam D01.

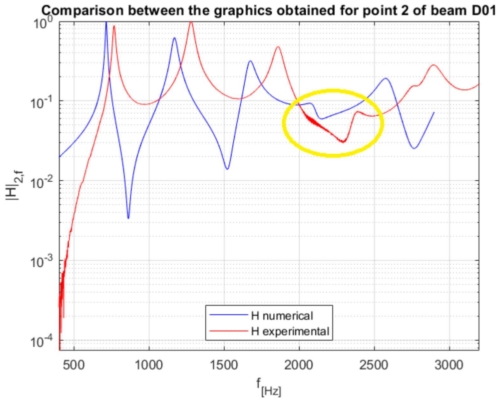

Figure 7.7: Comparison of numerical and experimental FRF for point 2 of beam D01.

Analyzing Figures 7.6 and 7.7, it is possible to verify that, as expected in Section 7.1, point number 2 is a node for all torsional modal forms since all frequency peaks related to these forms have been lost. Similarly, by visualizing these plots, the difficulty of representing the 4^{th} flexural modal form is even more evident (see the yellow circle in Figure 7.7).

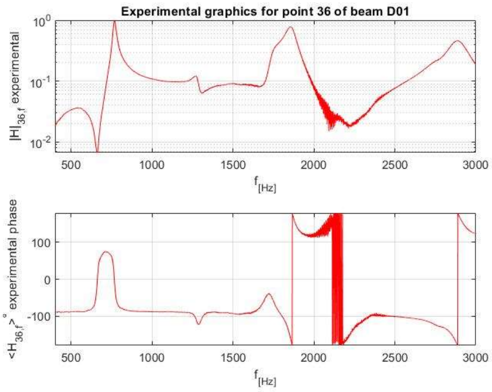

Figure 7.8: Experimental FRF for point 36 of beam D01.

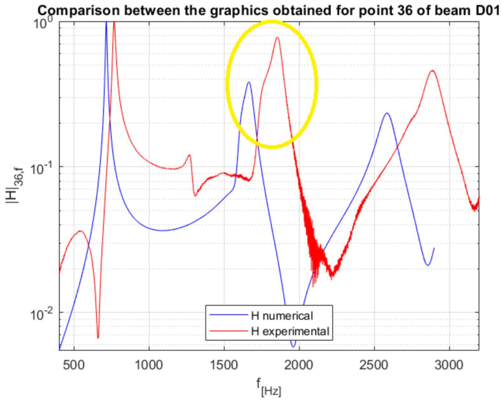

Figure 7.9: Comparison of numerical and experimental FRF for point 36 of beam D01.

Analyzing Figures 7.8 and 7.9, for point 36, as expected in Section 7.1 it can be concluded that this point is a node for all anti-symmetric modal shapes, as the peaks related to these modal shapes are not present. Also, in Figure 7.9, the overlap of the 2^{nd} torsional and the 3^{rd} flexural modes can be observed, as two peaks should have been observed since these are symmetric modal shapes. However, only one narrow peak was observed, but it was quite narrow (see the yellow circle in Figure 7.9). The fact that this mixing of modes is also present in the numerical FRF may indicate that these peaks were too close together, and when considering the ζ, it may be impossible to differentiate these two modes.

7.3.2 MAC analysis for beam D01

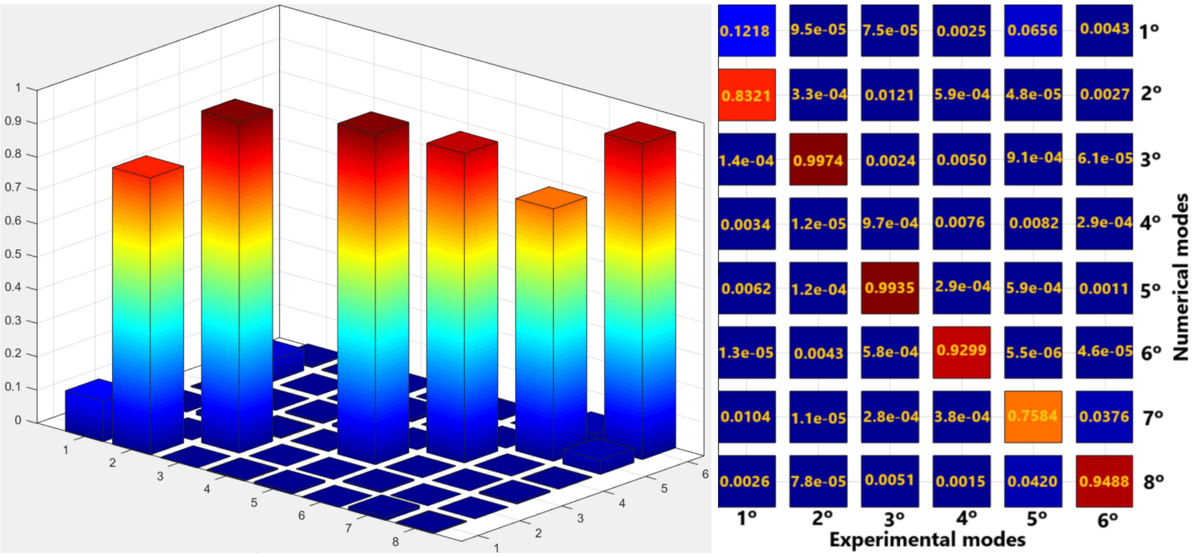

	1°	2°	3°	4°	5°	6°
1°	0.1218	9.5e-05	7.5e-05	0.0025	0.0656	0.0043
2°	0.8321	3.3e-04	0.0121	5.9e-04	4.8e-05	0.0027
3°	1.4e-04	0.9974	0.0024	0.0050	9.1e-04	6.1e-05
4°	0.0034	1.2e-05	9.7e-04	0.0076	0.0082	2.9e-04
5°	0.0062	1.2e-04	0.9935	2.9e-04	5.9e-04	0.0011
6°	1.3e-05	0.0043	5.8e-04	0.9299	5.5e-06	4.6e-05
7°	0.0104	1.1e-05	2.8e-04	3.8e-04	0.7584	0.0376
8°	0.0026	7.8e-05	0.0051	0.0015	0.0420	0.9488

(a) Graphical representation of MAC analysis for beam D01.

(b) MAC analysis results for beam D01.

Figure 7.10: MAC analysis for beam D01.

From the analysis of Figure 7.10, satisfactory results were obtained in the MAC analysis, as all other modes have a high correlation level (above 0.92) with only one numerical mode, except for the 1^{st} and 5^{th} experimental modes.

Furthermore, also from the analysis of Figure 7.10, it is possible to corroborate the statement that was previously made, namely, the fact that the first experimental mode is a 1^{st} flexo-torsional mode. This is because this experimental mode resembles the 1^{st} torsional numerical mode by about 12% and the 1^{st} flexural numerical mode by about 82%. It is also important to note that, despite the 4^{th} and 5^{th} experimental modes showing a significant correlation with their respective numerical modes, these correlations had a slightly lower level of similarity (0.92 and 0.73, respectively), which again indicates the previously mentioned low clarity of these modal shapes.

7.4 Analysis of the D02 beam

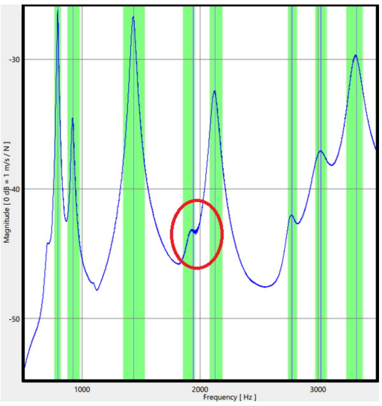

Figure 7.11: Graph used by the software to represent the modal shapes for beam D02.

Frequency peaks	Peak values [Hz]	ζ [%]
1^{st}	795	1.15
2^{nd}	920	1.56
3^{rd}	1436.25	1.66
4^{th}	1940	2.53
5^{th}	2125	1.84
6^{th}	2773.75	1.94
7^{th}	3018.75	2.90
8^{th}	3320	1.92

Table 7.3: Frequency peaks to be analysed and the Damping factor for beam D02.

Analyzing now beam D02, when comparing the graph obtained for this beam (see Figure 7.11) with graph for beam D01 (see Figure 7.2), one can observe that the software was able to reproduce the modal shape related to the small peak, which is for this beam near 2000 Hz (see the red circle in Figure 7.11). Therefore, it is already possible to suspect that, for this beam, the software was able to reproduce the 2^{nd} torsional modal shape. Thus the modal shapes obtained for the frequency peaks presented in Table 7.3 will now be shown and analysed individually.

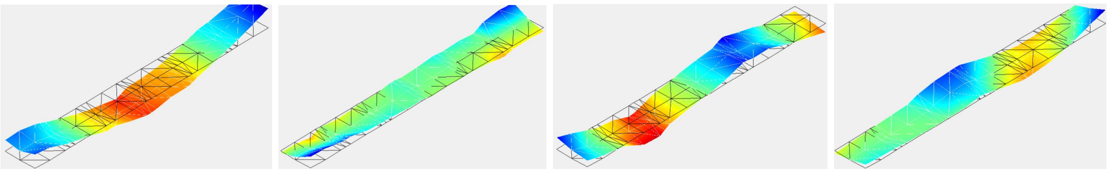

(a) Graphic representation for 795 Hz. (b) Graphic representation for 920 Hz. (c) Graphic representation for 1436.25 Hz. (d) Graphic representation for 1940 Hz.

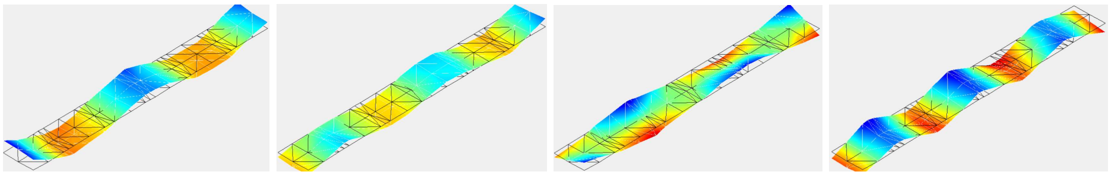

(e) Graphic representation for 2125 Hz. (f) Graphic representation for 2773.75 Hz. (g) Graphic representation for 3018.75 Hz. (h) Graphic representation for 3320 Hz.

Figure 7.12: Graphical representations obtained for the modal shapes for beam D02.

- 1^{st} **frequency peak (795 Hz)**- From the observation of Figure 7.12(a), it is possible to see that this peak may correspond to the 1^{st} **flexural numerical mode**, despite having some torsion;
- 2^{nd} **frequency peak (920 Hz)**- By observing Figure 7.12(b), it is possible to perceive that this peak may represent the 1^{st} **torsional numerical mode.** Thus, as the difference between the 1^{st} flexural and the 1^{st} torsional mode is higher for this beam, the laser was able to differentiate these two modal shapes;

- 3^{th} **frequency peak (1436.25 Hz)**- From the observation of Figure 7.12(c) and the corresponding animation, it is possible to see that this peak may represent the 2^{nd} **flexural numerical mode**, although there is a small amount of torsion present;
- 4^{th} **frequency peak (1940 Hz)**- From the observation of Figure 7.12(d), it appears that this peak may correspond to the 2^{nd} **torsional numerical mode**. However, by observing the animation, it is also clear that the representation of this mode was not very clear, as it had many perturbations;
- 5^{th} **frequency peak (2125 Hz)**- By observing Figure 7.12(e), it can be seen that this peak may represent the 3^{rd} **flexural numerical mode**. Unlike the 3^{rd} flexural mode of beam D01, this modal shape seems to have good clarity. This can be explained by the fact that the laser was able to capture, albeit with some difficulties, the 2^{nd} torsional mode, which may have resulted in less torsion for this flexural mode;
- 6^{th} **frequency peak (2773.75 Hz)**- Although there are not significant displacements, it is possible to notice that this peak may correspond to the 4^{th} **flexural numerical mode**. The difficulty in visualizing this possible mode persisted for this beam; however, the animation of this mode was slightly more informative when compared to the equivalent animation for beam D01;
- 7^{th} **frequency peak (3018.75 Hz)**- This peak may represent the 3^{rd} **torsional numerical mode**, and, unlike what happened for beam D01, this mode proved to be a little more clearer. This can be justified by the greater numerical difference observed between this modal shape and the 5^{th} flexural mode (about 300 Hz);
- 8^{th} **frequency peak (3320 Hz)**- This peak may represent the 5^{th} **flexural numerical mode**, and, unlike what happened in beam D01, it seems to have good clarity.

Table 7.4: Results obtained for the modal forms of beam D02.

numerical modal forms		**experimental modal forms**		**differences between models (%)**
modal shape type	frequency of the modal form [Hz]	modal shape type	frequency of the modal form [Hz]	
1^{st} flexural	753.14	1^{st} flexural	795	5.56
1^{st} torsional	846.32	1^{st} torsional	920	8.71
2^{nd} flexural	1344.4	2^{nd} flexural	1436.25	6.83
2^{nd} torsional	1798.5	2^{nd} torsional	1940	7.87
3^{rd} flexural	1947.3	3^{rd} flexural	2125	9.13
4^{th} flexural	2489.8	4^{th} flexural	2773.75	11.40
3^{rd} torsional	2795.3	3^{rd} torsional	3018.75	7.99
5^{th} flexural	3055.9	5^{th} flexural	3320	8.64

From the Table 7.4, it is clear that all experimental modal shapes have the same order as the numerical modal shapes. As observed for the D01 beam, the differences in frequency values between the numerical and experimental models are also significant for this beam, ranging around 5.56% but never exceeding 11.40%.

7.4.1 Analysis of FRF plots of selected points for beam D02

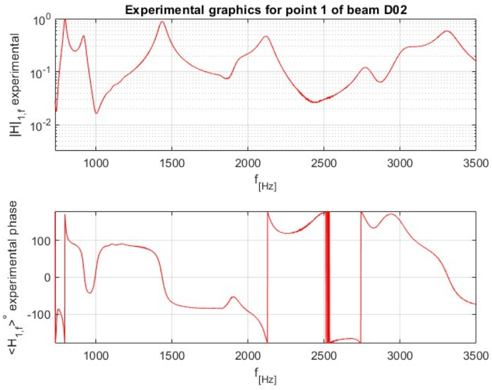

Figure 7.13: Experimental FRF for point 1 of beam D02.

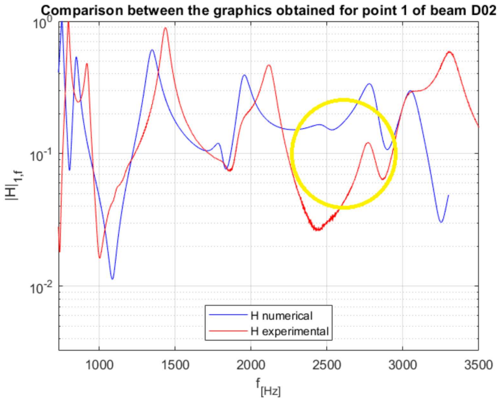

Figure 7.14: Comparison of numerical and experimental FRF for point 1 of beam D02.

The first observation that can be made by analyzing Figures 7.13 and 7.14 is that point 1 does not correspond to any node for any of the analyzed modal shapes, as expected in Section 7.1. Furthermore, it is important to note that, for this beam as well, the numerical and experimental FRFs appear to have a similar trend.

Additionally, it is once again evident that the 4^{th} flexural mode, as suspected, is not significant either numerically or experimentally (see yellow circle in Figure 7.14).

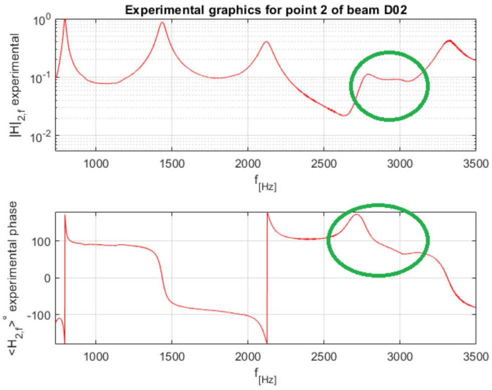

Figure 7.15: Experimental FRF for point 2 of beam D02.

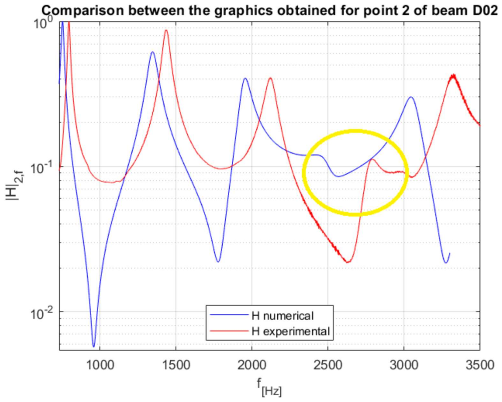

Figure 7.16: Comparison of numerical and experimental FRF for point 2 of beam D02.

In this case, it is also verified that this point corresponds to a node for all torsional modal shapes, as the frequency peaks related to these modal shapes have been lost, as expected. Similarly, by visualizing Figures 7.15 and 7.16, the difficulty of representing the 4^{th} flexural modal shape is evident once again in both the numerical and experimental FRFs (see yellow circle in Figure 7.16). This modal shape has a slight phase shift change, specifically from $170°$ to approximately $90°$ (see green circle in Figure 7.15).

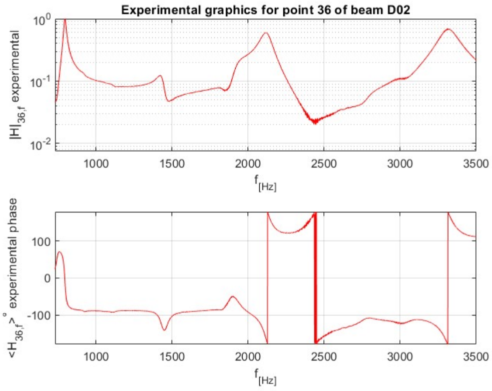

Figure 7.17: Experimental FRF for point 36 of beam D02.

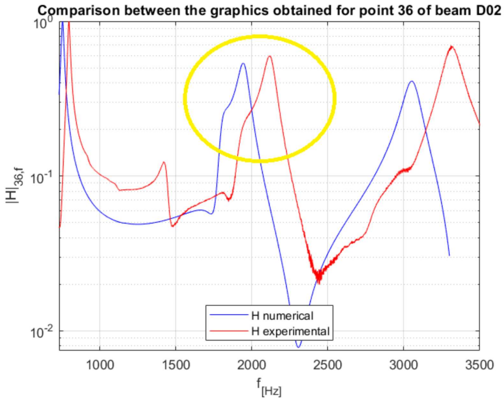

Figure 7.18: Comparison of numerical and experimental FRF for point 36 of beam D02.

Indeed, by observing Figures 7.17 and 7.18, it is possible to see that this point corresponds to a node for all anti-symmetric modal shapes, as all peaks related to these modal shapes have been lost again. Also, by observing these same figures, it is possible to understand why the 2^{nd} torsional modal shape was obtained with little definition. This occurred in both numerical and experimentally FRFs, because the peak related to this modal shape, besides being quite close to the 3^{rd} flexural peak, is almost insignificant, making it impossible to distinguish it completely from the peak related to the aforementioned flexural modal shape (see yellow circle in Figure 7.18).

7.4.2 MAC analysis for beam D02

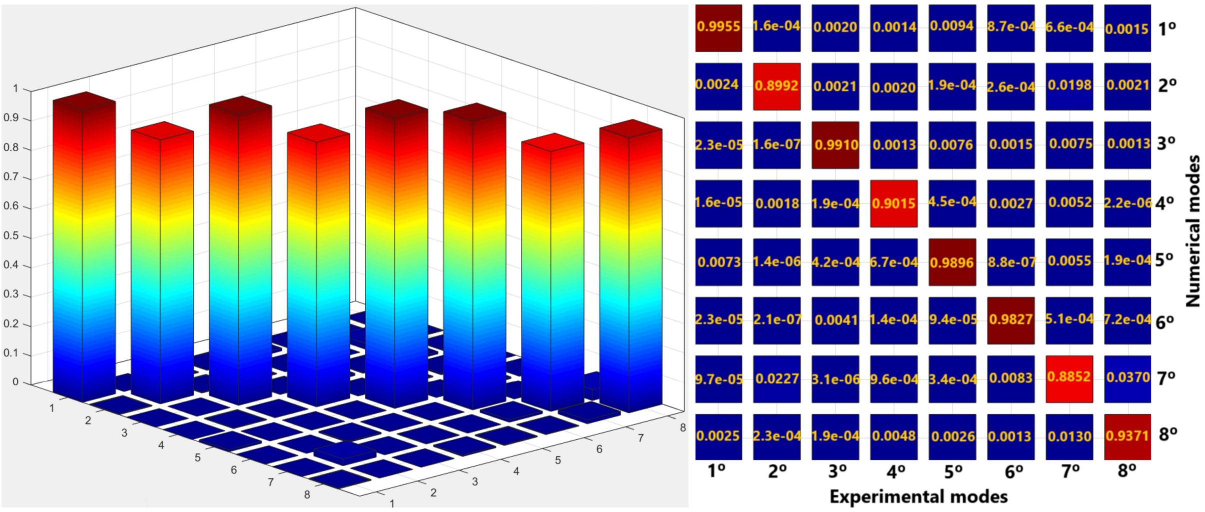

(a) Graphical representation of MAC analysis for beam D02.

Numerical modes	1°	2°	3°	4°	5°	6°	7°	8°
1°	0.9955	1.6e-04	0.0020	0.0014	0.0094	8.7e-04	6.6e-04	0.0015
2°	0.0024	0.8992	0.0021	0.0020	1.9e-04	2.6e-04	0.0198	0.0021
3°	2.3e-05	1.6e-07	0.9910	0.0013	0.0076	0.0015	0.0075	0.0013
4°	1.6e-05	0.0018	1.9e-04	0.9015	4.5e-04	0.0027	0.0052	2.2e-06
5°	0.0073	1.4e-06	4.2e-04	6.7e-04	0.9896	8.8e-07	0.0055	1.9e-04
6°	2.3e-05	2.1e-07	0.0041	1.4e-04	9.4e-05	0.9827	5.1e-04	7.2e-04
7°	9.7e-05	0.0227	3.1e-06	9.6e-04	3.4e-04	0.0083	0.8852	0.0370
8°	0.0025	2.3e-04	1.9e-04	0.0048	0.0026	0.0013	0.0130	0.9371

Experimental modes

(b) MAC analysis results for beam D02.

Figure 7.19: MAC analysis for beam D02.

From the analysis of Figure 7.19, it can be observed that satisfactory results were obtained in the MAC analysis for this particular beam. This is corroborated by the fact that all elements on the diagonal of the matrix in Figure 7.19(b) exhibit a high level of similarity. Thus, it is noted that only the 2^{nd}, 4^{th}, and 7^{th} modes of both models showed a slightly lower level of similarity among themselves, albeit never falling below 88%. Another aspect to consider is that each mode in each of the models only resembles one mode in the other model. In other words, the first experimental mode corresponds to the first numerical mode, and so forth. This indicates, once again, that the numerical model can be considered a good approximation of the reality under study.

7.5 Analysis of the D03 beam

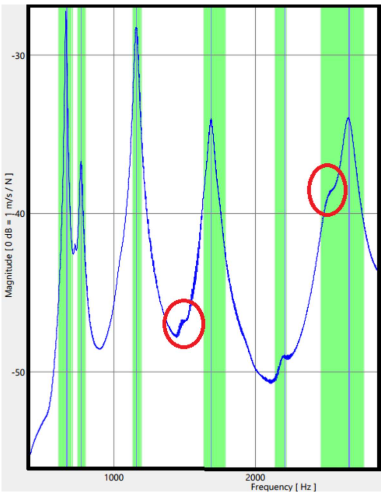

Figure 7.20: Graph used by the software to represent the modal shapes for beam D03.

Frequency peaks	Peak values [Hz]	ζ [%]
1^{st}	662.5	0.84
2^{nd}	770	1.68
3^{rd}	1158.75	1.57
4^{th}	1690	2.08
5^{th}	2210	1.54
6^{th}	2660	1.87

Table 7.5: Frequency peaks to be analysed and the Damping factor for beam D03.

From the observation of Figure 7.20, it can be seen that the laser was not able to detect two possible frequency peaks, one at approximately 1500 Hz and another at approximately 2500 Hz. Therefore, downstream, in the detailed analysis of the selected points, it will be studied whether these possible peaks actually correspond to frequency peaks (see the red circles in Figure 7.20). Thus the graphical representations obtained for the frequency peaks shown in Table 7.5 are shown in Figure 7.21, and each of these peaks will now be analysed individually.

- 1^{st} **frequency peak (662.5 Hz)**- By observing Figure 7.21(a), it is possible to see that the frequency peak could correspond to the 1^{st} **flexural numerical mode**;
- 2^{nd} **frequency peak (770 Hz)**- Upon observation of Figure 7.21(b), it is possible to perceive that the frequency peak could represent the 1^{st} **torsional numerical mode**. Furthermore, by viewing the animation of this LDV prediction, it corroborates this hypothesis;
- 3^{rd} **frequency peak (1158.75 Hz)**- From the observation of Figure 7.21(c), it is possible to perceive that this frequency peak could represent the 2^{nd} **flexural numerical mode**;
- 4^{th} **frequency peak (1690 Hz)**- From the observation of Figure 7.21(d), it is possible to notice

that this frequency peak could represent the 3^{rd} **flexural numerical mode**. However, through the observation of the produced animation, it is evident that this mode, despite being a flexural modal shape, presents some torsion. This could have happened due to the same reason explained for beam D01, that is, the small peak at approximately 1500 Hz (see the first red circle in Figure 7.20), which the software could not recognize, might represent the 2^{nd} torsional mode. Thus, as it is very close to the 3^{rd} flexural mode, the sharpness of this modal shape was compromised;

- 5^{th} **frequency peak (2210 Hz)**- Despite the lack of clarity in the representation of Figure 7.21(e), this frequency peak could represent the 4^{th} **flexural numerical mode**. The low clarity of this modal shape (which is noticeable when viewing its animation) may be related to the previously mentioned fact, namely, the position where the Shaker was placed may not facilitate the visualization of this mode;
- 6^{th} **frequency peak (2660 Hz)**- The frequency peak represented in Figure 7.21(f) could correspond to the 5^{th} **flexural numerical mode**. However, it is possible to observe that, despite being a flexural mode, it has some torsion. This torsion could be related, once again, to the fact that there may be a frequency peak at 2500 Hz, which was not detected by the LDV (see the second red circle in Figure 7.20), and which could correspond to the 3^{rd} torsional mode.

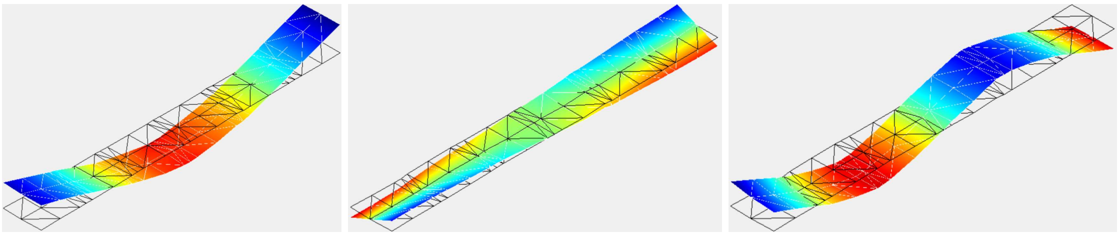

(a) Graphic representation for 662.5 Hz. (b) Graphic representation for 770 Hz. (c) Graphic representation for 1158.75 Hz.

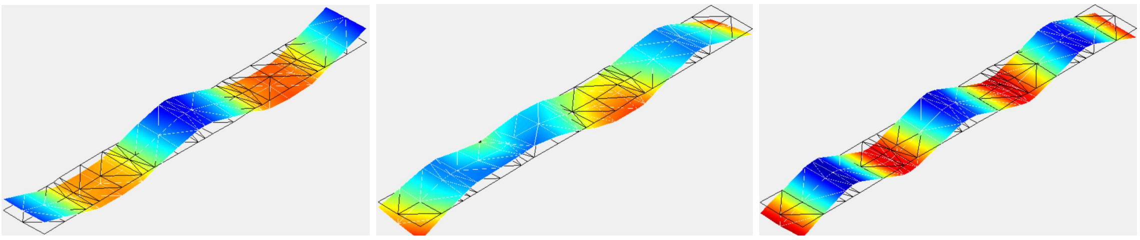

(d) Graphic representation for 1690 Hz. (e) Graphic representation for 2210 Hz. (f) Graphic representation for 2660 Hz.

Figure 7.21: Graphical representations obtained for the modal shapes for beam D03.

After this analysis, it should be mentioned that for this beam, which is significantly thinner than the previous two (see Table 4.2), the LDV was able to represent the low-frequency modal shapes with greater clarity. However, it had more difficulty identifying and representing higher-order modal shapes, as some of them were separated by only a few Hz (the 2^{nd} numerical torsional mode and the 3^{rd} numerical flexural mode have a difference of only approximately 3 Hz, while the 3^{rd} numerical torsional mode and the 5^{th} numerical flexural mode exhibit a difference of approximately 63 Hz, as can be observed in Table 7.6).

Table 7.6: Results obtained for the modal forms of beam D03.

numerical modal forms		experimental modal forms		differences between models (%)
modal shape type	frequency of the modal form [Hz]	modal shape type	frequency of the modal form [Hz]	
1^{st} flexural	620.64	1^{st} flexural	662.5	6.74
1^{st} torsional	693.14	1^{st} torsional	770	11.09
2^{nd} flexural	1052.6	2^{nd} flexural	1158.75	10.08
2^{nd} torsional	1508.7			
3^{rd} flexural	1511.8	3^{rd} flexural	1690	11.79
4^{th} flexural	1925.3	4^{th} flexural	2210	14.78
3^{rd} torsional	2310.5			
5^{th} flexural	2373.5	5^{th} flexural	2660	12.07

Based on Table 7.6, it is clear that, although the 2^{nd} and 3^{rd} torsional modal shapes were not identified, the experimental modal shapes follow the same order as the numerical modal shapes. It is also important to note that the differences between the two models were significant (between 6.74% and 14.78%), particularly for the higher-order modal shapes (above 1500 Hz). This likely occurred because these higher-order modal shapes were very close to modal shapes that the LDV could not identify.

7.5.1 Analysis of FRF plots of selected points for beam D03

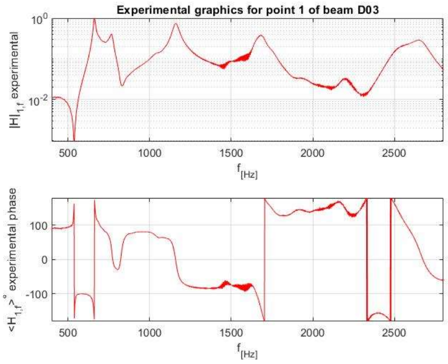

Figure 7.22: Experimental FRF for point 1 of beam D03.

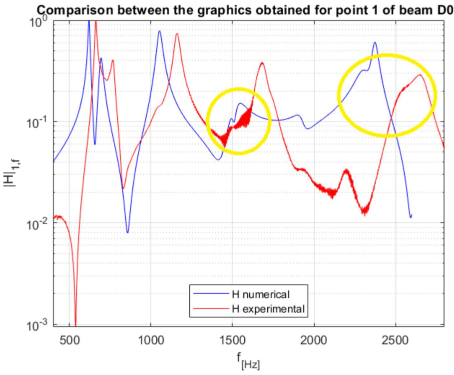

Figure 7.23: Comparison of numerical and experimental FRF for point 1 of beam D03.

By observing Figures 7.22 and 7.23, the first observation that can be made is that point 1 is not a node for any of the analyzed modal shapes, as all the frequency peaks related to them were observed in previous graphs. It is also important to highlight that, as seen in Figure 7.23, the numerical and experimental FRFs show a similar trend. Furthermore, it is also worth noting that from previous plots, it is possible to realize that both the supposed peaks for both models are still quite difficult to observe, especially the peak at 1500 Hz in the experimental model where the LDV was not able to consistently capture it (see yellow circles in Figure 7.23).

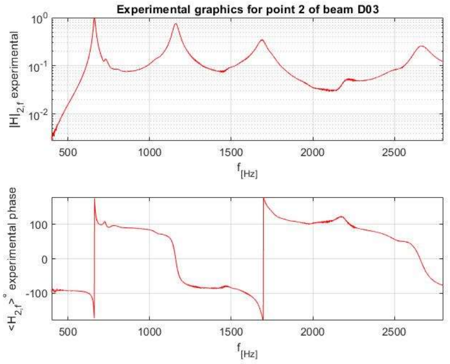

Figure 7.24: Experimental FRF for point 2 of beam D03.

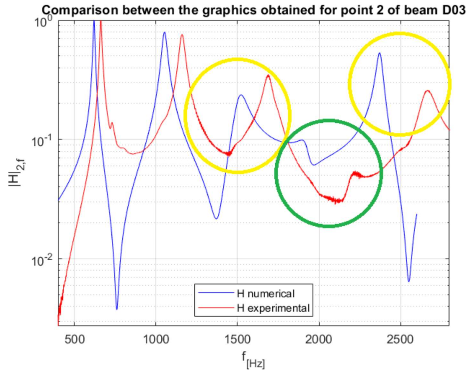

Figure 7.25: Comparison of numerical and experimental FRF for point 2 of beam D03.

In this case, it is also observed in Figures 7.24 and 7.25 that point 2 corresponds, as expected in Section 7.1, to a node for all torsional modal forms, since the frequency peaks for these modes are not present. Similarly, from the visualization of these plots, besides the continuing difficulty in representing the 4^{th} flexural modal form for this beam (see green circle in Figure 7.25), the noise in the experimental model for the frequency of 1500 Hz disappeared, and the peak of the 5^{th} flexural mode became clearer (see yellow circles in Figure 7.16). Thus, these observations support the premise that those two peaks, not identified by the laser, should represent the 2^{nd} and 3^{rd} torsional modal forms, something that probably could not be previously verified due to their proximity to the 3^{rd} and 5^{th} flexural modes.

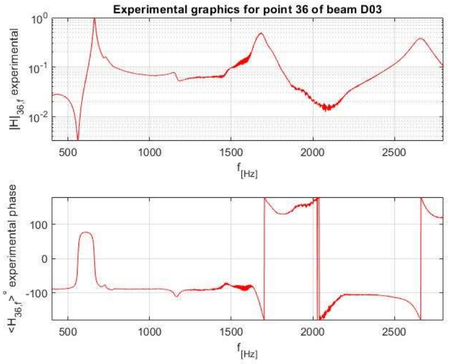

Figure 7.26: Experimental FRF for point 36 of beam D03.

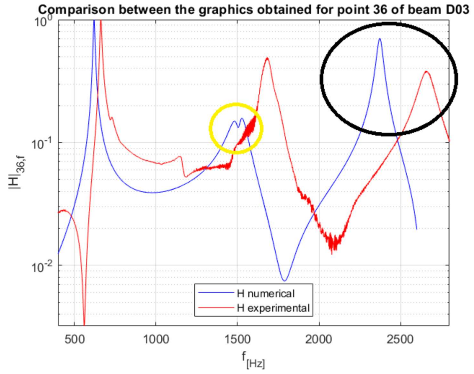

Figure 7.27: Comparison of numerical and experimental FRF for point 36 of beam D03.

Indeed, by observing Figures 7.26 and 7.27, this point corresponds to a node for all anti-symmetric modal shapes, as all the peaks related to these modes have been lost. In these graphs, the difficulty of visualizing the frequency peak related to the 2^{nd} torsional mode is evident again for both models (see yellow circle in Figure 7.27). Additionally, for these FRF plots, the peak related to the 5^{th} flexural mode is much clearer, as the 3^{rd} torsional mode was suppressed (see black circle in Figure 7.27).

7.5.2 MAC analysis for beam D03

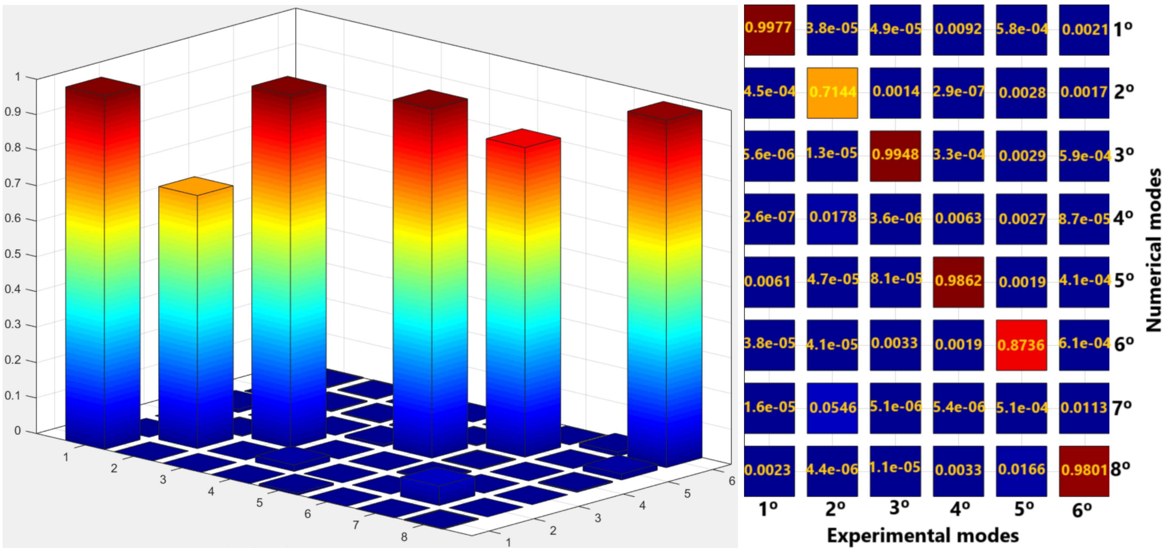

1°	2°	3°	4°	5°	6°	
0.9977	3.8e-05	4.9e-05	0.0092	5.8e-04	0.0021	1°
4.5e-04	0.7144	0.0014	2.9e-07	0.0028	0.0017	2°
5.6e-06	1.3e-05	0.9948	3.3e-04	0.0029	5.9e-04	3°
2.6e-07	0.0178	3.6e-06	0.0063	0.0027	8.7e-05	4°
0.0061	4.7e-05	8.1e-05	0.9862	0.0019	4.1e-04	5°
3.8e-05	4.1e-05	0.0033	0.0019	0.8736	6.1e-04	6°
1.6e-05	0.0546	5.1e-06	5.4e-06	5.1e-04	0.0113	7°
0.0023	4.4e-06	1.1e-05	0.0033	0.0166	0.9801	8°

(a) Graphical representation of MAC analysis for beam D03.

(b) MAC analysis results for beam D03

Figure 7.28: MAC analysis for beam D03.

From the analysis of Figure 7.28, it is evident that except for the 2^{nd} and 5^{th} experimental modes, all other experimental modes have a very high level of similarity with only one numerical mode (with MAC always above 0.98). Therefore, it is noticeable that the two experimental modes that did not exhibit a high MAC value were also the ones where the LDV was unable to represent their modal shape with good clarity. Lastly, it should also be noted that neither the 4^{th} nor the 7^{th} numerical modes correlated with any of the experimental modes, which supports the previously mentioned hypothesis, specifically that the LDV was unable to identify two possible frequency peaks that would likely resemble these numerical modes.

7.6 Analysis of the D04 beam

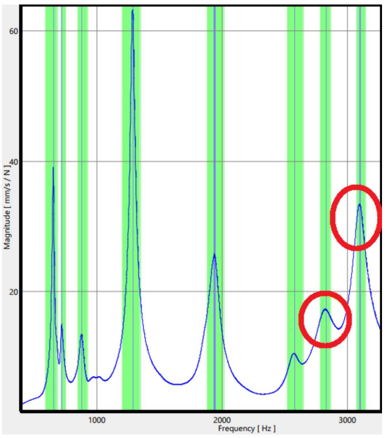

Figure 7.29: Graph used by the software to represent the modal shapes for beam D04.

Frequency peaks	Peak values [Hz]	ζ [%]
1^{st}	653.75	1.52
2^{nd}	722.5	—
3^{rd}	880	2.35
4^{th}	1286.75	1.42
5^{th}	1940	1.79
6^{th}	2575	1.97
7^{th}	2827.5	2.75
8^{th}	3098.75	1.98

Table 7.7: Frequency peaks to be analysed and the Damping factor for beam D04.

By analyzing Figure 7.29, it is evident that the first two peaks are extremely close to each other. This observation is quite unusual since, upon a quick comparison with the numerical analysis (see Figure 4.3), there should only be two frequency peaks below 1000 Hz. Additionally, it's important to note that the two peaks typically associated with the 3^{rd} torsional and 5^{th} flexural modes (see red circles in Figure 7.29) were well-differentiated by the software. With that in mind, the graphical representations obtained for the frequency peaks listed in Table 7.7 are shown in Figure 7.30, and each of these peaks will now be analyzed individually.

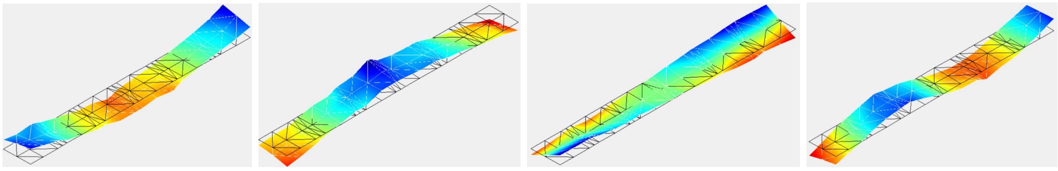

(a) Graphic representation for 653.75 Hz. (b) Graphic representation for 722.5 Hz. (c) Graphic representation for 880 Hz. (d) Graphic representation for 1286.75 Hz.

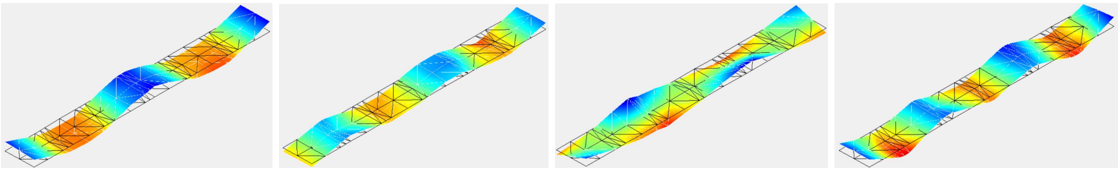

(e) Graphic representation for 1940 Hz. (f) Graphic representation for 2575 Hz. (g) Graphic representation for 2827.5 Hz. (h) Graphic representation for 3098.75 Hz.

Figure 7.30: Graphical representations obtained for the modal shapes for beam D04.

- 1^{st} **frequency peak (653.75 Hz)**- Upon observing Figure 7.30(a), it appears that this frequency peak might correspond to the 1^{st} **flexural numerical mode**. Although it exhibits some little torsion;
- 2^{nd} **frequency peak (722.5 Hz)**- From the observation of Figure 7.30(b), it seems that this frequency peak could also represent the 1^{st} **flexural numerical mode**. However, through the animation produced by LDV, it becomes evident that this modal shape has more torsion compared to the previous one. Additionally, by examining Figure 7.29, it's noticeable that this peak is much less significant than the preceding one. Therefore, considering these reasons, this peak will be disregarded, and in the subsequent analysis of the FRF plots for the selected points, this issue will be revisited;
- 3^{rd} **frequency peak (880 Hz)**- By observing Figure 7.30(c), it appears that this frequency peak might represent the 1^{st} **torsional numerical mode**, and through the animation, this mode can be visualized with good clarity;
- 4^{th} **frequency peak (1286.75Hz)**- From the observation of Figure 7.30(d), it can be noticed that this frequency peak could represent the 2^{nd} **flexural numerical mode**, which exhibits a good level of clarity;
- 5^{th} **frequency peak (1940 Hz)**- By observing Figure 7.30(e), it is possible to notice that the frequency peak could correspond to the 3^{rd} **flexural numerical mode**. Also, by looking at the ani-

mation, it can be seen that this mode is not as clear as the previous ones due to the existence of some torsion;

- 6^{th} **frequency peak (2575 Hz)**- Although Figure 7.30(f) is not very clear, but it can be noticed that this frequency peak might correspond to the 4^{th} **flexural numerical mode**. Once again, this lack of clarity might be explained by the position of the Shaker;
- 7^{th} **frequency peak (2827.5 Hz)**- By observing Figure 7.30(g), this frequency peak could correspond to the 3^{rd} **torsional numerical mode**, and similar to what happened with beam D02, this frequency peak has good clarity;
- 8^{th} **frequency peak (3098.75 Hz)**- By observing Figure 7.30(h), it can be seen that this frequency peak could correspond to the 5^{th} **flexural numerical mode**, and from the animation, it can be seen that this modal shape has good clarity, similar to what was observed for beam D02.

Taking all of this into account, it should be noted that the laser did not identify the second torsional mode. However, by analyzing the graph in Figure 7.29, it can be seen that all existing peaks were identified, indicating that the peak corresponding to this mode must be very insignificant and therefore did not appear in that graph . Further downstream, this fact will be analyzed in more detail.

Table 7.8: Results obtained for the modal forms of beam D04.

numerical modal forms		**experimental modal forms**		**differences between models (%)**
modal shape type	frequency of the modal form [Hz]	modal shape type	frequency of the modal form [Hz]	
1^{st} flexural	647.61	1^{st} flexural	653.75	0.95
1^{st} torsional	827.48	1^{st} torsional	880	6.35
2^{nd} flexural	1208.3	2^{nd} flexural	1286.75	6.49
2^{nd} torsional	1712.7			
3^{rd} flexural	1770.5	3^{rd} flexural	1940	9.57
4^{th} flexural	2289.5	4^{th} flexural	2575	12.47
3^{rd} torsional	2583.7	3^{rd} torsional	2827.5	9.44
5^{th} flexural	2815.7	5^{th} flexural	3098.75	10.05

By observing Table 7.8, it's evident that despite the 2^{nd} torsional mode not being identified, the experimental modal shapes follow the same order as the numerical modal shapes. It's important to note that the differences between the models are significant, especially for modal shapes above 1700 Hz (ranging from 0.95% to 12.47%), but were slightly lower for this beam compared to the other beams studied. It's worth mentioning that the modal shape with the highest difference of frequency was the 4^{th} flexural mode, which again supports the previously mentioned hypothesis that the positioning of the Shaker may have negatively influenced the visualization of this modal shape.

7.6.1 Analysis of FRF plots of selected points for beam D04

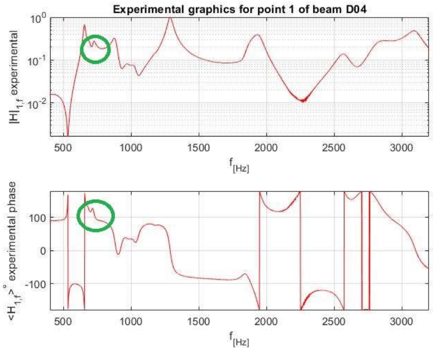

Figure 7.31: Experimental FRF for point 1 of beam D04.

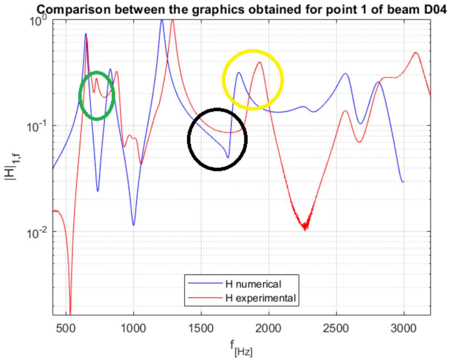

Figure 7.32: Comparison of numerical and experimental FRF for point 1 of beam D04.

By examining Figures 7.31 and 7.32, the first observation to be made is that point 1 is not a node for any of the analyzed modal shapes, as all the frequency peaks related to them were observed in the previous plots. Furthermore, it is important to highlight that, as seen in Figure 7.32, the numerical and experimental FRF plots are somewhat similar, with the frequency peaks of the numerical model appearing before those of the experimental model.

Another important observation to note is that both the experimental and numerical FRF for this point do not show any frequency peak that could correspond to the 2^{nd} torsional mode (see black circle in Figure 7.32). Also, it is noticeable that the peak related to the 3^{rd} flexural mode is slightly broader for both models, suggesting that the 2^{nd} torsional mode may have mixed with this same modal shape (see yellow circle in Figure 7.32).

Furthermore, by analyzing Figure 7.32, it can be confirmed that the frequency peak detected by the laser at 722.5 Hz is only present in the experimental model (see green circle in Figure 7.32). However, this peak may not correspond to a specific modal shape since there is no significant phase change- approximately $125°$ to approximately $100°$ (see green circles in Figure 7.31).

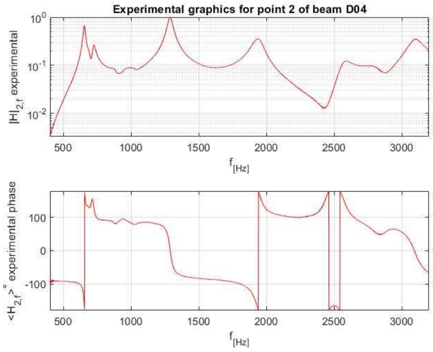

Figure 7.33: Experimental FRF for point 2 of beam D04.

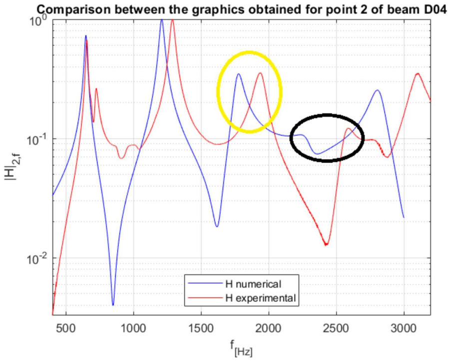

Figure 7.34: Comparison of numerical and experimental FRF for point 2 of beam D04.

Observing Figures 7.33 and 7.34, it is possible to see that the point in question is a node for all torsional modes, as the frequency peaks for these modes are not present. Another important observation to be made is that the peak corresponding to the 3^{rd} flexural mode is more sharper (see yellow circle in Figure 7.34) when compared to the peak corresponding to this modal shape in Figure 7.32. Therefore, since this point is a node for all torsional modes, the hypothesis that the peak corresponding to the 2^{nd} torsional mode has mixed with the peak of this flexural mode is corroborated. Finally, it is also possible to observe that the peak corresponding to the 4^{th} flexural mode is not very significant, which explains why this mode was difficult to visualize (see black circle in Figure 7.34).

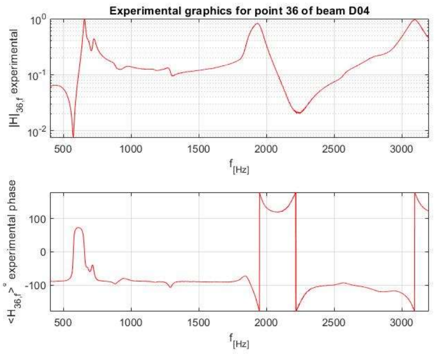

Figure 7.35: Experimental FRF for point 36 of beam D04.

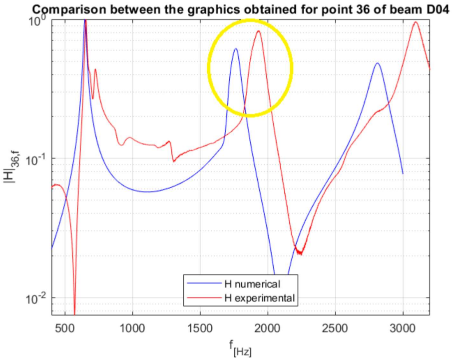

Figure 7.36: Comparison of numerical and experimental FRF for point 36 of beam D04.

By observing Figures 7.35 and 7.36, it is possible to confirm that this point corresponds to a node for all anti-symmetric modal shapes, as all the peaks related to these shapes have been lost. Also, after analyzing these plots, the peak related to the 3^{rd} flexural mode becomes slightly wider again (see yellow circle in Figure 7.36), as the 2^{nd} torsional mode is a symmetric modal form and at this point, only anti-symmetric modal forms are canceled out, as previously mentioned. Therefore, the theory that the 2^{nd} torsional mode mixed with the 3^{rd} flexural mode is once again corroborated.

7.6.2 MAC analysis for beam D04

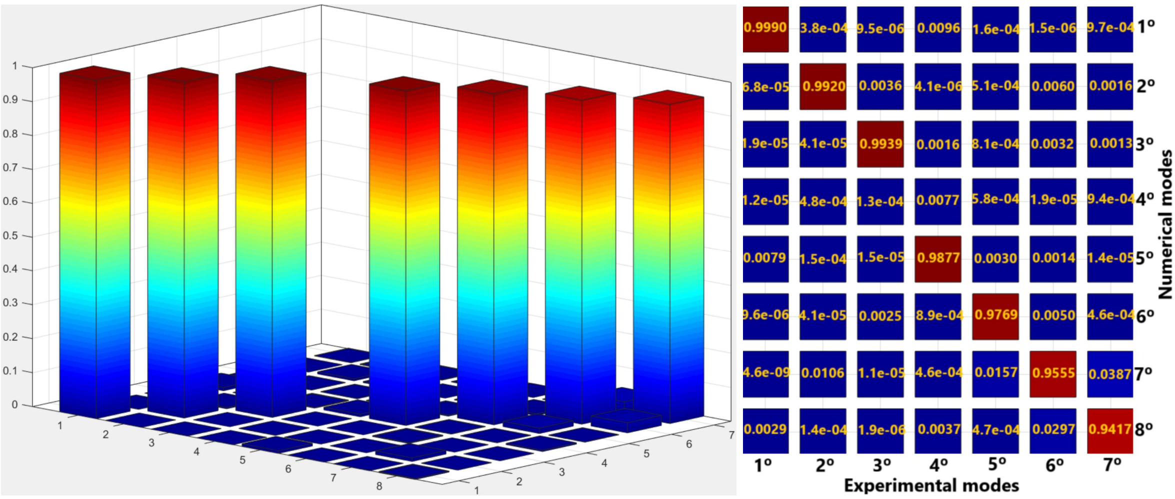

1°	2°	3°	4°	5°	6°	7°	Numerical modes
0.9990	3.8e-04	9.5e-06	0.0096	1.6e-04	1.5e-06	9.7e-04	1°
6.8e-05	0.9920	0.0036	4.1e-06	5.1e-04	0.0060	0.0016	2°
1.9e-05	4.1e-05	0.9939	0.0016	8.1e-04	0.0032	0.0013	3°
1.2e-05	4.8e-04	1.3e-04	0.0077	5.8e-04	1.9e-05	9.4e-04	4°
0.0079	1.5e-04	1.5e-05	0.9877	0.0030	0.0014	1.4e-05	5°
9.6e-06	4.1e-05	0.0025	8.9e-04	0.9769	0.0050	4.6e-04	6°
4.6e-09	0.0106	1.1e-05	4.6e-04	0.0157	0.9555	0.0387	7°
0.0029	1.4e-04	1.9e-06	0.0037	4.7e-04	0.0297	0.9417	8°

Experimental modes

(a) Graphical representation of MAC analysis for beam D04.

(b) MAC analysis results for beam D04.

Figure 7.37: MAC analysis for beam D04.

By examining Figure 7.37, it is evident that each of the experimental modes relates to the corresponding numerical mode, with high similarity values observed in all cases (the lowest value observed was approximately 0.94 for the relationship between the 7^{th} experimental mode and the 8th numerical mode). Additionally, from the analysis of the previous figure, it can be deduced that the 4^{th} numerical mode did not relate to any other experimental mode, which further supports the hypothesis that this mode may have mixed with the 3^{rd} flexural mode, making its identification impossible. Lastly, it is worth mentioning that, except for the numerical mode that did not relate to any of the experimental modes (which did not occur, for example, with beam D02), the MAC analysis values for this beam were higher than those obtained for any of the other beams studied.

7.7 Hammer Test

It was observed that the differences between the numerical and experimental models were on the order of 10%. Therefore, one of the hypotheses raised was that the Shaker introduced significant stiffness at the contact point with the structure, even mitigating the aforementioned bending effect, thus altering the natural frequencies of the experimental model.

In order to investigate this hypothesis, it was decided to disconnect the Shaker from one of the structures under study and excite it with the Impact Hammer. If the obtained frequencies were significantly lower, then it would confirm that this was one of the factors that influenced the differences observed between the two models.

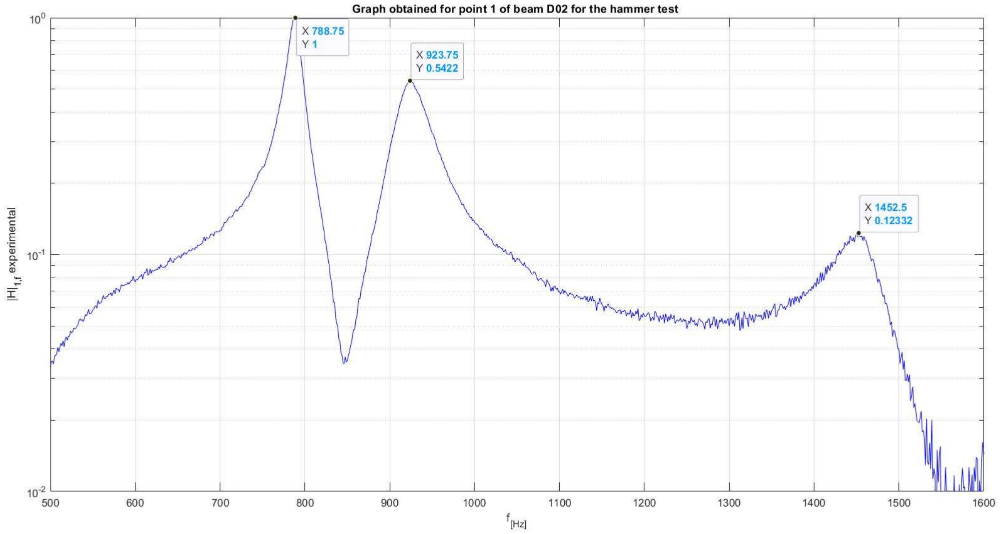

Figure 7.38: Experimental FFR for point 1 of beam D02 for Hammer test.

In addition, it should be noted that beam D02 was selected for this study because it allowed obtaining all the lowest modal shapes, which were crucial for comparing the results of this experiment. Since the method used to connect the Shaker was identical for all the beams under study, it was sufficient to conduct this study on beam D02 only.

Furthermore, it's worth highlighting that this study's effectiveness is quite positive. Even though the higher-frequency modal shapes were not studied, any potential effect of increased stiffness when using the Shaker, if it existed, would likely have a relatively consistent impact across all modal shapes. Additionally, this experimental activity was conducted solely for point 1 of configuration 6.1 to comprehensively analyze all possible natural frequencies obtainable through this type of test.

Having discussed this, Figure 7.38 displays the frequency peaks obtained in this test, and Table 7.9 provides a comprehensive comparison of all the results.

Table 7.9: Comparison of the results obtained for all the experiments for beam D02.

modal shape type	**numerical frequencies [Hz]**	**Shaker Test**		**Hammer Test**	
		Experimental frequencies [Hz]	diferences between models (%)	Experimental frequencies [Hz]	diferences between models (%)
1^{st} flexural	753.14	795	5.56	788.75	4.51
1^{st} torsional	856.32	920	7.44	923.75	7.87
2^{nd} flexural	1344.4	1436.25	6.83	1452.5	8.04

Upon examining Table 7.9, it becomes evident that the results from the experimental test using the Shaker and the Impact Hammer show relatively minor differences. Specifically, only the first natural frequency obtained with the Impact Hammer is slightly lower than that obtained in the Shaker test (by approximately 7 Hz). Consequently, it can be inferred that the issue under investigation is not significant, and therefore, it is unlikely to be the primary cause of the significant discrepancies observed between the numerical and experimental models.

Therefore, the observed frequency differences between both models may be related to various factors, such as defects in the beams themselves, a significant increase in stiffness due to the configuration used, or even the need to recalculate the physical constants of the materials to perform modal updating [18].

Chapter 8

Conclusions

Before proceeding with the conclusions, it's important to provide a concise overview of the entire experimental activity. In this project, four composite beams, located in the Laboratory of the Department of Mechanical and Aerospace Engineering at Politecnico di Torino, were examined. These beams featured 7075 aluminium faces and a WF-110 polymer foam core. However, the thickness of these materials varied from beam to beam, resulting in different results for each of these beams. Also, in this project, it was aimed to perform the **Modal Test** in a **Free Condition**. Thus, different configurations were studied to understand which one better simulated this situation.

In addition, to enable a preliminary estimation of the dynamic behaviour of the structures under study, a **Finite Element Model** was built for each of these structures, and a numerical analysis was performed on each of these **Finite Element Models**. This entire process was carried out using the Patran/Nastran software. The numerical studies were not only very useful for the implementation of the experimental activity but, after the analysis of the results obtained, these numerical studies were validated.

It is also important to note that in this project, unlike the usual modal test practice (where accelerometers are traditionally used for response measurement [3, 10–13]), a **Laser Doppler Vibrometer** was used. This was done because another goal of this project was to understand the feasibility of using this technology for modal testing. Thus, for the correct implementation of this technology, a preliminary study of it was also necessary.

Finally, after the **structural analysis** of the beams under study, where the first **resonance** frequencies and their corresponding vibration modes were obtained, the results for both models were compared and analyzed. To achieve this, two MATLAB programs were developed. One allowed the collection of all the numerical and experimental data needed to create the Frequency Response Analysis plots, and the other program facilitated the Modal Assurance Criterion analysis between the mentioned models.

That said, we will now begin to outline all the relevant conclusions that can be formulated, considering everything discussed in Chapter 7.

First and foremost, it should be noted that the use of the LDV can be considered a good alternative to the use of more conventional devices for conducting this type of experimental activity. This is evident from the good results obtained for the coherence function, never lower than 0.85.

The configuration of points chosen to perform the measurements (6.1) fulfilled the proposed objectives, as expected. With this configuration, whenever the frequency peaks associated with modal shapes were clearly identified, the LDV was able to reproduce all modal shapes quite smoothly, something easily observable through the visualization of the animations produced by this device. In these animations, it was always possible to identify the presence of flection, torsion, or both phenomena, depending on the prediction made by this device for each modal shape.

In addition, another important consideration to make is that the experimental modal shapes, for all beams under study, had the same order as the numerical modal shapes. Furthermore, it's noteworthy that the frequencies of the experimental modal shapes were consistently higher than the frequencies of the numerical modal shapes, with these differences typically hovering around 10% (for the higher-frequency modal shapes, this difference tended to be higher). Therefore, despite the significant differences observed between the two models, the fact that they shared the same modal order and the coherence between the FRF plots obtained for both models, which showed a somewhat similar trend, allows us to conclude that the numerical models can indeed be considered a good approximation of the reality under study.

Furthermore, it is worth mentioning that the only beam in which all the intended numerical modal shapes could be visualized was beam D02. Therefore, as observed, for beams D04, D03, and D01, it was not possible to observe the 2^{nd} torsional mode, with the 3^{rd} torsional mode also not being observed for D03, and a first-order flexural-torsional mode being observed for D01. Considering this, it can be concluded that beams D02 and D04 were the most suitable for experimental analysis. These beams shared the same thickness of the aluminium surfaces (1 mm), and they exhibited significant differences in the frequency values for each of the modal shapes in the numerical analyses. Thus, to obtain satisfactory results in this type of activity, it is important for the beams under study to have significantly different natural frequency values.

Also, it's worth noting that the modal shape with the highest difference of frequency in all beams studied was the 4^{th} flexural mode. This observation supports the earlier suggestion that the Shaker's position may impede the acquisition and visualization of this specific modal shape.

Regarding the MAC analyses conducted, it can be concluded that both models exhibited a hight correlation. Except for a few isolated cases where the frequency difference between modal shapes was not significant, all modal shapes had values above 0.95. Moreover, all modal shapes (except for the 1^{st} flexo-torsional mode of beam D01) correlated only with their corresponding modal shape in the numerical model. This further supports the previous statement that the constructed numerical models can be considered good approximations of the real models under study.

Lastly, regarding the Shaker, it was also found that it does not introduce significant stiffness in the structures under study, and the frequency differences obtained arise due to factors that still need to be studied. However, one of the causes that cannot be ruled out and likely introduced significant stiffness is the configuration itself that was used to approximate the study under Free-free conditions. Although it was believed that this configuration introduced the least stiffness to the beams under study and thus represented the best possible approximation to the Free-free condition (see Chapter 5.1.3), it still introduced some stiffness, which could have been a determining factor in the significant frequency differences observed. Also, the possibility that the beams under study may have their own deformations and their own manufacturing defects cannot be ruled out, and these defects could have negatively influenced the obtained results

8.1 Achievements

The main achievements obtained with the completion of this work were as follows:

- A sufficiently detailed FEM model of the composite beams to be studied was successfully created;
- It was demonstrated that the use of LDV technology can be advantageous for modal testing, especially for lightweight and small-sized structures;
- By conducting experimental activities, it was possible to collect experimental data for the four beams under study;
- With the collected data, it was possible to analyze the dynamic behaviour of all the beams under study;
- The selected configuration of measurement points proved effective in capturing and predicting all modal shapes by the LDV;
- The results of the numerical and experimental models were similar and consistent, as the modal shapes consistently exhibited the same order in both models, and the frequency differences remained relatively constant for all beams studied;
- Highly satisfactory results were obtained for the MAC index for almost all modal shapes of all beams;
- Despite the previously mentioned issues, the structure assembly created allowed for a reasonably satisfactory simulation of the Free-free condition;
- Considering all the experimental results obtained, it is possible to affirm that the previously developed FEM models made good approximations to the structures under study.

8.2 Future Work

Taking into account all the work carried out in this project and all the conclusions that have already been mentioned, it is possible to highlight the following suggestions that could be explored in future work:

- Build and test composite beams of different configurations based on a prior and reliable numerical model that predicts a more significant difference in frequency between all modal shapes. By conducting experimental activities with these beams, it will be possible to verify, with a higher degree of certainty, whether the modal shapes that were not captured by the LDV in this work were due to having an insignificant frequency difference from other modal shapes;

- Utilize SLDV technology to scan the structures under study, thereby enhancing the precision of the numerical models;
- Seek a solution for the Shaker's placement to investigate whether it was the reason for obtaining not only lower resolution of the 4^{th} flexural modes in all beams but also the largest frequency differences between the two models under study;
- Utilize other correlation metrics in addition to the MAC index. This approach will enable the comparison of results obtained from these different correlations with the MAC index, providing more insights into the reliability of the results in this work;
- Employ an LDV equipped with Multipoint measurement technology to increase the number of measurement points without significantly extending the duration of the laboratory activity. This will further enhance the resolution and accuracy of the modal shapes predicted by the LDV;
- Test different structure assembly configurations to discover an alternative setup that not only reduces the stiffness introduced by the current configuration in the beams under study but also enables the examination of flexural modal shapes in the y-axis.

Bibliography

[1] Y. G. Z. Ru-Min Wang, Shui-Rong Zheng, *Polymer Matrix Composites and Technology*, 1st ed. Woodhead Publishing, jul 2011.

[2] V. V. Vasiliev and E. V. Morozov, *Advanced Mechanics of Composite Materials and Structural Elements*, 4th ed. Elsevier, jun 2018.

[3] L. Sá, "Modelling and validation of finite element structural analysis of istsat-1," MSc Thesis in Aerospace Engineering, Instituto Superior Técnico, Lisboa, Portugal, dec 2021.

[4] A. E. Krauklis, C. W. Karl, A. I. Gagani, and J. K. Jørgensen, "Composite material recycling technology—state-of-the-art and sustainable development for the 2020s," *Journal of Composites Science*, vol. 5, no. 1, p. 28, 2021.

[5] K. K. Kar, *Composite materials: processing, applications, characterizations*. Springer, 2017.

[6] S. Rana and R. Fangueiro, *Advanced Composite Materials for Aerospace Engineering*, 1st ed. Woodhead Publishing, 2016.

[7] A. Quilter, "Composites in aerospace applications," *IHS White Paper*, vol. 444, no. 1, p. 264, 2001.

[8] J. Hale, "787 from the ground up," *Aero Magazine*, vol. 4, 09 2006.

[9] M. Mrazova, "Advanced composite materials of the future in aerospace industry," *Incas bulletin*, vol. 5, no. 3, p. 139, 2013.

[10] M. F. Green, "Modal test methods for bridges: a review," in *Proceedings-Spie the International Society for Optical Engineering*. Citeseer, 1995, pp. 552–552.

[11] F. Falcetelli, A. Martini, R. Di Sante, and M. Troncossi, "Strain modal testing with fiber bragg gratings for automotive applications," *Sensors*, vol. 22, no. 3, 2022. [Online]. Available: https://www.mdpi.com/1424-8220/22/3/946

[12] Z. Ibrahim and P. Reynolds, "Modal testing of a cantilever grandstand," in *Proceedings of the International Conference on Construction and Building Technology (ICCBT'08)*, 2008, pp. 271–284.

[13] Y. Govers, J. Sinske, and T. Petzsche, "Latest design trends in modal accelerometers for aircraft ground vibration testing," in *Sensors and Instrumentation, Aircraft/Aerospace, Energy Harvesting*

& Dynamic Environments Testing, Volume 7, C. Walber, P. Walter, and S. Seidlitz, Eds. Cham: Springer International Publishing, 2020, pp. 97–106.

[14] T. N. Y. Times. (1970, nov) Collapse of tacoma bridge 30 years ago recalled. [Accessed 5-6-2023]. [Online]. Available: https://www.nytimes.com/1970/11/08/archives/collapse-of-tacoma-bridge-30-years-ago-recalled.html

[15] A. K. Chopra, *Dynamics of Structures, 4/E*, 4th ed. Prentice Hall/ Pearson, 2011.

[16] B. M. John M. Vance, Fouad Y. Zeidan, *Machinery Vibration and Rotordynamics*, 1st ed. John Wiley Sons, Inc., 2010.

[17] J. M. M. e Silva and N. M. Maia, *Modal analysis and testing*. Springer Science & Business Media, 2012, vol. 363.

[18] D. Ewins, *Modal Testing: Theory, Practice and Application*, 2nd ed. Research Studies Press LTD., 2000.

[19] P. Avitabile, *Modal testing: a practitioner's guide*. John Wiley & Sons, 2017.

[20] J.-C. Chen, "Evaluation of modal testing methods," in *25th Structures, Structural Dynamics and Materials Conference*, 1984, p. 1071.

[21] M. Peeters, G. Kerschen, and J.-C. Golinval, "Modal testing of nonlinear vibrating structures based on nonlinear normal modes: Experimental demonstration," *Mechanical Systems and Signal Processing*, vol. 25, no. 4, pp. 1227–1247, 2011.

[22] P. M. Gherlone, "Lezioni di dinamica delle strutture aerospaziali," 2023, [Slides from the course Dynamics of structures of the aerospace engineering course at PoliTO].

[23] J. F. B. de Meireles, "Analise dinamica de estruturas por modelos de elementos finitos identificados experimentalmente," Ph.D. dissertation, Universidade do Minho, Guimarães, 2007.

[24] B. Vandevelde, M. Gonzalez, P. Limaye, P. Ratchev, J. Vanfleteren, and E. Beyne, "Lead free solder joint reliability estimation by finite element modelling advantages, challenges and limitations," in *7th international conference on Leadfree electronic components and assemblies, Frankfurt, Germany*, 2004.

[25] P. Castellini, M. Martarelli, and E. Tomasini, "Laser doppler vibrometry: Development of advanced solutions answering to technology's needs," *Mechanical Systems and Signal Processing*, vol. 20, no. 6, pp. 1265–1285, 2006, special Issue: Laser Doppler Vibrometry. [Online]. Available: https://www.sciencedirect.com/science/article/pii/S0888327005002220

[26] K. Kroschel, *Laser Doppler Vibrometry for Non-Contact Diagnostics*, 1st ed., ser. Bioanalysis 9. Springer International Publishing;Springer, 2020.

[27] S. Rothberg, M. Allen, P. Castellini, D. Di Maio, J. Dirckx, D. Ewins, B. Halkon, P. Muyshondt, N. Paone, T. Ryan, H. Steger, E. Tomasini, S. Vanlanduit, and J. Vignola, “An international review of laser doppler vibrometry: Making light work of vibration measurement,” *Optics and Lasers in Engineering*, vol. 99, pp. 11–22, 2017, laser Doppler vibrometry. [Online]. Available: https://www.sciencedirect.com/science/article/pii/S0143816616303724

[28] T. Harčarik, J. Bocko, and K. Masláková, “Frequency analysis of acoustic signal using the fast fourier transformation in matlab,” *Procedia Engineering*, vol. 48, pp. 199–204, 2012, modelling of Mechanical and Mechatronics Systems. [Online]. Available: https://www.sciencedirect.com/science/article/pii/S1877705812045687

[29] S. S. Rao, *Mechanical Vibrations*, 5th ed. Prentice Hall, 2010.

[30] S. V. Eliseev and A. V. Eliseev, *Theory of Oscillations*, 1st ed. Springer, 2020.

[31] F. S. Tse, I. E.Morse, and R. T.Hinkle, *Mechanical Vibrations Theory and Applications*, 2nd ed. Boston, MA, United States: Pearson Allyn and Bacon, 1978.

[32] D. d. E. E. Puc-rio. Sistema mola-massa-amortecedor. [Accessed 15-6-2023]. [Online]. Available: https://www.maxwell.vrac.puc-rio.br/20591/sistema_mola_amortecedor1.html?fbclid=IwAR2GkUjiHuCb0JkPfhi2qgOrsf_wEnG4I9EKsGN4nNC-8OX0BVBPZTH5aUA

[33] L. Barreira, *Análise Complexa e Equações Diferenciais*, 1st ed. IST Press, sep 2009.

[34] K. K. Panigrahi. (2022) Difference between laplace transform and fourier transform. [Online]. Available: https://www.tutorialspoint.com/difference-between-laplace-transform-and-fourier-transform

[35] J. Clark. Dirac delta function. [Accessed 9-06-2023]. [Online]. Available: https://jeremyclark.ca/wp/telecom/dirac-delta-function-%CE%B4t/

[36] K. de Souza Oliveira Filho. (2011) Transformadas de fourier. [Accessed 9-6-2023]. [Online]. Available: http://astro.if.ufrgs.br/med/imagens/fourier.htm

[37] B. Peeters, G. Lowet, H. Van der Auweraer, and J. Leuridan, “A new procedure for modal parameter estimation,” *Sound and Vibration*, vol. 38, no. 1, pp. 24–29, 2004.

[38] B. Peeters, H. Van der Auweraer, P. Guillaume, and J. Leuridan, “The polymax frequency-domain method: a new standard for modal parameter estimation?” *Shock and Vibration*, vol. 11, no. 3-4, pp. 395–409, 2004.

[39] F. M. Hemez, C. J. S. (auth.), T. Simmermacher, S. Cogan, B. Moaveni, and C. Papadimitriou, *Topics in Model Validation and Uncertainty Quantification, Volume 5: Proceedings of the 31st IMAC, A Conference on Structural Dynamics, 2013*, 1st ed. Springer-Verlag New, 2013, vol. 5, ch. 13.

[40] W. Liu, S. Li, and H. Park, “Eighty years of the finite element method: Birth, evolution, and future,” *Archives of Computational Methods in Engineering*, vol. 29, 06 2022.

[41] L. Meirovitch, *FUNDAMENTALS OF VIBRATIONS*. McGraw-Hill Book Co, 2001.

[42] A. Leissa, “The historical bases of the rayleigh and ritz methods,” *Journal of Sound and Vibration*, vol. 287, no. 4, pp. 961–978, 2005. [Online]. Available: https://www.sciencedirect.com/science/article/pii/S0022460X05000362

[43] kot. (2020, nov) entenda o método dos elementos finitos. [Accessed 19-8-2023]. [Online]. Available: https://kotengenharia.com.br/para-leigos-entenda-o-metodo-dos-elementos-finitos/

[44] N. Guo, Z. Yang, Y. Jia, and L. Wang, “Model updating using correlation analysis of strain frequency response function,” *Mechanical Systems and Signal Processing*, vol. 70-71, pp. 284–299, 2016. [Online]. Available: https://www.sciencedirect.com/science/article/pii/S0888327015004483

[45] M. Sorrenti, “Refined zigzag models for the response of general multilayered composite and sandwich structures: numerical and experimental investigations,” Ph.D. dissertation, Politecnico di Torino, jul 2023.

[46] A. Technologie, “The fundamentals of modal testing,” Agilent Technologies, Tech. Rep., 2000, application Note 243-3.

[47] A. Brandt, *Noise and Vibration Analysis*, 1st ed. A John Wiley and Sons, 2011.

[48] J. E. M. a. M. I. Friswell, *Finite Element Model Updating in Structural Dynamics*, 1st ed., ser. Solid Mechanics and its Applications 38. Springer Netherlands, 1995.

[49] Introduction to icp accelerometers. [Accessed 18-3-2023]. [Online]. Available: https://www.pcb.com/resources/technical-information/introduction-to-accelerometers

[50] Optimizing time delay feedback for active vibration control of a cantilever beam using a genetic algorithm. [Accessed 18-3-2023]. [Online]. Available: https://journals.sagepub.com/doi/10.1177/1077546315569863

[51] M. Martarelli, “Exploiting the laser scanning facility for vibration measurements,” Ph.D. dissertation, University of London London, UK, 2001.

[52] G. F. Lang. (2023) The coherence function - a brief review. [Accessed 3-05-2023]. [Online]. Available: https://www.crystalinstruments.com/blog/2015/1/12/the-coherence-function-a-brief-review

[53] J. Shaw, “An introduction to the coherence function and its use in eeg signal analysis,” *Journal of medical engineering & technology*, vol. 5, no. 6, pp. 279–288, 1981.

[54] J. He and Z. F. Fu, “10 – multi-input multi-output modal analysis methods,” 2001.

[55] G. Heo, M. Wang, and D. Satpathi, “Optimal transducer placement for health monitoring of long span bridge,” *Soil Dynamics and Earthquake Engineering*, vol. 16, no. 7, pp. 495–502, 1997. [Online]. Available: https://www.sciencedirect.com/science/article/pii/S0267726197000109

[56] P. C. e. Enrico Primo Tomasini (editor), *Laser Doppler Vibrometry: A Multimedia Guide to its Features and Usage*, 1st ed. Springer, 2020.

[57] (2023, mar) Difference between doppler effect and doppler shift. [Accessed 11-3-2023]. [Online]. Available: https://www.geeksforgeeks.org/difference-between-doppler-effect-and-doppler-shift/

[58] M. J. Rudd, “A laser doppler velocimeter employing the laser as a mixer-oscillator,” *Journal of Physics E: Scientific Instruments*, vol. 1, no. 7, p. 723, jul 1968. [Online]. Available: https://dx.doi.org/10.1088/0022-3735/1/7/305

[59] B. Schröder and R. Geick, “The problem of nonlinear phase errors introduced by misalignment of a michelson interferometer,” *Infrared Physics*, vol. 18, no. 5, pp. 595–605, 1978. [Online]. Available: https://www.sciencedirect.com/science/article/pii/0020089178900763

[60] C. Cristalli, N. Paone, and R. Rodríguez, “Mechanical fault detection of electric motors by laser vibrometer and accelerometer measurements,” *Mechanical Systems and Signal Processing*, vol. 20, no. 6, pp. 1350–1361, 2006, special Issue: Laser Doppler Vibrometry. [Online]. Available: https://www.sciencedirect.com/science/article/pii/S0888327005002190

[61] F. Harris, “On the use of windows for harmonic analysis with the discrete fourier transform,” *Proceedings of the IEEE*, vol. 66, no. 1, pp. 51–83, 1978.

[62] Y. Rolain, J. Schoukens, and G. Vandersteen, “Signal reconstruction for non-equidistant finite length sample sets: a ”kis” approach,” *IEEE Transactions on Instrumentation and Measurement*, vol. 47, no. 5, pp. 1046–1052, 1998.

[63] W. Zheng, R. V. Kruzelecky, and R. Changkakoti, “Multichannel laser vibrometer and its applications,” in *Third International Conference on Vibration Measurements by Laser Techniques: Advances and Applications*, ser. Society of Photo-Optical Instrumentation Engineers (SPIE) Conference Series, E. P. Tomasini, Ed., vol. 3411, Jun. 1998, pp. 376–384.

[64] E. Cupido, S. Morel, and D. Smith, “Multipoint laser doppler vibrometer for transient analysis,” *Proceedings of IMAC XXI*, 2003.

[65] Oms corporation products. [Accessed 18-3-2023]. [Online]. Available: https://www.omscorporation.com/products/

[66] P. PIEZOTRONICS. (2023) Model exciter kit, model k2007e01. [Accessed 29-04-2023]. [Online]. Available: https://www.pcb.com/products?m=k2007e01

[67] Polytec, *Operating Instructions Polytec Scanning Vibrometer, PSV-500-3D*.

[68] I. PCB Piezotronics, *Installation and Operating Manual Impact Hammer Model 086C03*, 3425 Walden Ave. Depew, NY14043 USA.

[69] T. Emmert. (2023) Uff file reading and writing. [Accessed 29-04-2023]. [Online]. Available: https://github.com/murmlgrmpf/uff

Appendix A

MatLab code developed for FRF plots

The following MATLAB code was developed to collect all the experimental and numerical data for beam D01, enabling the visualization of all the FRF plots presented in Chapter 7 (it is worth noting that a similar program was developed for each of the other beams):

```

%% FRF Plots for beam D01 %%

clc
clear all
close all

[DS, Info, errmsg] = readuff('D01_prova4_ridotta.unv'); % take experimental data
file_1=fopen('D01_report_forca_freq.txt','r'); % remove frequencies
file_2=fopen('D01_report_forca_z.txt','r'); % draw strength

w=[400:1.25:3000]; % change in frequency of numerical data
H=zeros([length(w) 1]);

dados=input(['What point do you want to assess \n (you can choose one of the',...
             'points indicated: 1,2,18,36) \n','s']);
verification_point= false;

while verification_point == false
    if dados == '1'
        results_point=DS{33}.measData; % experimental data for point 1
        x_points=DS{33}.x; % change in frequency of experimental data
        file_3=fopen('D01_report_extremidade_z.txt','r'); % numeric data from point 1
        title_1='Comparison between the graphics obtained for point 1 of beam D01';
        title_2='Numeric graphics for point 1 of beam D01';
        title_3='Experimental graphics for point 1 of beam D01';
        y_label_1='|H|_{1,f}';
        y_label_2_1= '|H|_{1,f} numerical';
        y_label_2_2= '<H_{1,f}>^{  } numerical phase';
```

```
        y_label_3_1= '|H|_{1,f} experimental';
        y_label_3_2= '<H_{1,f}>^{  } experimental phase';
        verification_point= true;

    elseif dados == '2'
        results_point=DS{32}.measData; % experimental data for point 2
        x_points=DS{32}.x; % change in frequency of experimental data
        file_3=fopen('D01_report_sem_rotacionais_z.txt','r'); % numeric data from point 2
        title_1='Comparison between the graphics obtained for point 2 of beam D01';
        title_2='Numerical graphics for point 2 of beam D01';
        title_3='Experimental graphics for point 2 of beam D01';
        y_label_1='|H|_{2,f}';
        y_label_2_1= '|H|_{2,f} numerical';
        y_label_2_2= '<H_{2,f}>^{  } numerical phase';
        y_label_3_1= '|H|_{2,f} experimental';
        y_label_3_2= '<H_{2,f}>^{  } experimental phase';
        verification_point= true;

    elseif dados == '18'
        results_point=DS{47}.measData; % experimental data for point 18
        x_points=DS{47}.x; % change in frequency of experimental data
        file_3=fopen('D01_report_sem_1_flessionais_z.txt','r'); % numerical data of point 18
        title_1='Comparison between the graphics obtained for point 18 of beam D01';
        title_2='Numerical graphics for point 18 of beam D01';
        title_3='Experimental graphics for point 18 of beam D01';
        y_label_1='|H|_{18,f}';
        y_label_2_1= '|H|_{18,f} numerical';
        y_label_2_2= '<H_{18,f}>^{  } numerical phase';
        y_label_3_1= '|H|_{18,f} experimental';
        y_label_3_2= '<H_{18,f}>^{  } experimental phase';
        verification_point= true;

    elseif dados == '36'
        results_point=DS{25}.measData; % experimental data for point 36
        x_points=DS{25}.x; % change in frequency of experimental data
        file_3=fopen('D01_report_sem_antisimetricas_z.txt','r'); % numerical data of point 36
        title_1='Comparison between the graphics obtained for point 36 of beam D01';
        title_2='Numerical graphics for point 36 of beam D01';
        title_3='Experimental graphics for point 36 of beam D01';
        y_label_1='|H|_{36,f}';
        y_label_2_1= '|H|_{36,f} numerical';
        y_label_2_2= '<H_{36,f}>^{  } numerical phase';
        y_label_3_1= '|H|_{36,f} experimental';
        y_label_3_2= '<H_{36,f}>^{  } experimental phase';
        verification_point= true;

    else
        disp('Choose one of the points indicated: 1,2,18,36')
        dados=input('What point do you want to assess \n ','s')
```

```
    end

end

a=0;
Cond=true;
while Cond==true
    a=a+1;
    aline=fgetl(file_1); % to advance each line of the txt file
    if mod(a+1,4)== 0
        linha=regexp(aline, '\S ' ,'split');
        w_proprio((a+1)/4)=str2double(linha(5)); % to transform the string of
                                                 % the txt file  into a number
    end
    if strcmpi(aline(1:3), 'END')
        Cond = false;
    end
end

a=0;
Cond=true;
while Cond==true
    a=a+1;
    aline=fgetl(file_2);
    if mod(a,2)== 0
        linha=regexp(aline, '\S ' ,'split');
        eig_val_for(a/2)=str2double(linha(4));
    end
    if strcmpi(aline(1:3), 'END')
        Cond = false;
    end
end

a=0;
Cond=true;
while Cond==true
    a=a+1;
    aline=fgetl(file_3);
    if mod(a,2)== 0
        linha=regexp(aline, '\S ' ,'split');
        eig_val_extre(a/2)=str2double(linha(4));
    end
    if strcmpi(aline(1:3), 'END')
        Cond = false;
    end
end


for a=1:length(w_proprio)
```

```
    for i=1:length(w)
         H(i)= H(i)+ 1i*w(i)*(eig_val_extre(a)*eig_val_for(a))/...
             (w_proprio(a)^2-w(i)^2); % Calculation of numerical H
    end
end

H_points=abs(H);
for r=1:length(H)
    if H_points(r)== inf
        H_points(r)=0; % to eliminate the numbers that, due to the transformation
                       % from imaginary to real, are Inf because their imaginary
                       % part is equal to zero
    end
end

figure(1)
semilogy(w,H_points/max(H_points),'b')
hold on
semilogy(x_points,abs(results_point)/max(real(abs(results_point))),'r')
hold on
grid on
title(title_1)
legend('H numerical','H experimental','Location','south')
ylabel(y_label_1)
xlabel('f_{[Hz]}')
axis([w(1),w(length(w)),0,1])

figure(2)
subplot(2,1,1)
semilogy(w,H_points/max(H_points),'b')
title(title_2)
grid on
ylabel(y_label_2_1)
xlabel('f_{[Hz]}')
axis([w(1),w(length(w)),min(H_points/max(H_points)),...
    max(H_points/max(H_points))])
subplot(2,1,2)
plot(w,angle(H)*180/pi,'b')
ylabel(y_label_2_2)
xlabel('f_{[Hz]}')
axis([w(1),w(length(w)),min(angle(H)*180/pi),max(angle(H)*180/pi)])

figure(3)
subplot(2,1,1)
semilogy(x_points,abs(results_point)/max(real(abs(results_point))),'r')
title(title_3)
ylabel(y_label_3_1)
xlabel('f_{[Hz]}')
grid on
```

```
axis([w(1),w(length(w)),min(abs(results_point)/...
    max(real(abs(results_point)))),max(abs(results_point)/...
    max(real(abs(results_point))))])
subplot(2,1,2)
plot(x_points,angle(results_point)*180/pi,'r')
grid on
ylabel(y_label_3_2)
xlabel('f_{[Hz]}')
axis([w(1),w(length(w)),min(angle(results_point)*180/pi),...
    max(angle(results_point)*180/pi)])
```

Appendix B

MatLab code developed to perform MAC analyses

The following code was developed to perform MAC analyses for any of the beams under study:

```

%% MAC Analysis %%

clc
clear all
close all
dados = input(['Which MAC value do you want to access? \n You can access the ', ...
              'MAC values of bar 1,2,3,4 ', ...
              '(type 1,2,3,4, depending on which beam you want to analyze) \n'], 's');
verification_point= false;

while verification_point == false
    if dados == '1'
            % Open the file for reading experimental points
            file_1 = fopen('posicoes_pontos_exp_D01.txt','r');
            numero_freq_proprias_exp=6; %number of experimentally measured frequencies
                                        % for the beam studied

            % Open the file for reading experimental normal vectors
            file_2 = fopen('NormalModesD01_cor.txt','r');
            comp_linha_file_ex=6;

            % Open the file for reading numerical points and numerical normal vectors
            file_3 = fopen('pontos_todos_numericos_D01_cor.txt','r');
            numero_freq_proprias_num=8; %number of numerically studied
                                        %frequencies for the beam studied

            title_1='Modal Assurance Criterion of beam D01';
```

```
            verification_point= true;

    elseif dados == '2'
            % Open the file for reading experimental points
            file_1 = fopen('posicoes_pontos_exp_D02.txt','r');
            numero_freq_proprias_exp=8; %number of experimentally measured
                                        %frequencies for the beam studied
            comp_linha_file_ex=3;

            % Open the file for reading experimental normal vectors
            file_2 = fopen('NormalModesD02_cor.txt','r');

            % Open the file for reading numerical points and numerical normal vectors
            file_3 = fopen('pontos_todos_numericos_D02_cor.txt','r');
            numero_freq_proprias_num=8; %number of numerically studied
                                        %frequencies for the beam studied

            title_1='Modal Assurance Criterion of beam D02';
            verification_point= true;

        elseif dados == '3'
            % Open the file for reading experimental points
            file_1 = fopen('posicoes_pontos_exp_D03.txt','r');
            numero_freq_proprias_exp=6; %number of experimentally measured
                                        %frequencies for the beam studied
            comp_linha_file_ex=3;

            % Open the file for reading experimental normal vectors
            file_2 = fopen('NormalModesD03_cor.txt','r');

            % Open the file for reading numerical points and numerical normal vectors
            file_3 = fopen('pontos_todos_numericos_D03_cor.txt','r');
            numero_freq_proprias_num=8; %number of numerically studied
                                        %frequencies for the beam studied

            title_1='Modal Assurance Criterion of beam D03';
            verification_point= true;

        elseif dados == '4'
            % Open the file for reading experimental points
            file_1 = fopen('posicoes_pontos_exp_D04.txt','r');
            numero_freq_proprias_exp=7; %number of experimentally measured
                                        %frequencies for the beam studied
            comp_linha_file_ex=3;

            % Open the file for reading experimental normal vectors
            file_2 = fopen('NormalModesD04_cor.txt','r');

            % Open the file for reading numerical points and numerical normal vectors
```

```
            file_3 = fopen('pontos_todos_numericos_D04_cor.txt','r');
            numero_freq_proprias_num=8; %number of numerically studied
                                        %frequencies for the beam studied
            title_1='Modal Assurance Criterion of beam D04';
            verification_point= true;

        else
            disp('Choose one of the beams indicated: 1,2,3,4')
            dados=input('Which MAC value do you want to access?','s')
        end
end

% Initialize variables
pontos = zeros(3, 70);
a = 0;
Cond = true;

% Read data from the file and populate the 'pontos' matrix
while Cond == true
    a = a + 1; % Counter for the current line number (goes up to 140)
    aline = fgetl(file_1); % Read the current line from the file

    % Process odd lines (excluding line 140)
    if mod(a, 2) ~= 0 && a < 140
        linha = regexp(aline, '\s ', 'split'); % Split the line by whitespace
        pontos(1, (a + 1) / 2) = str2double(linha(5)); % Convert the 5th element of
                                                        %the line to a number and store it
                                                        %in the 'pontos' matrix
    % Process even lines
    elseif mod(a, 2) == 0
        linha = regexp(aline, '\s ', 'split'); % Split the line by whitespace
        numeros = 0; % Initialize a vector to store numbers
        % Iterate over each element in the line
        for i = 1:numel(linha)
            str = strtrim(linha{i}); % Remove whitespace from the element
            if ~isempty(str) % Check if the element is not empty
                numeros(i) = str2double(str); % Convert the element to a number
                                            %and store it in the 'numeros' vector
            end
        end
        b = 1; % Counter for storing valid coordinates
        c = 0; % Counter for iterating over 'numeros'
        % Filter out zeros and store the non-zero coordinates
        while c < length(numeros)
            c = c + 1;
            if numeros(c) ~= 0
                coordenadas(b) = numeros(c); % Store the non-zero coordinate
                                             % value in the 'coordenadas' vector
                b = b + 1;
```

```
            end
        end
        pontos(2, a / 2) = coordenadas(1); % Store the x-coordinate in the 'pontos' matrix
        pontos(3, a / 2) = coordenadas(2); % Store the y-coordinate in the 'pontos' matrix
    % Check for the end of the file marker
    elseif strcmpi(aline(1:3), 'END')
        Cond = false;
    end
end

pontos(:, end) = []; % Remove the last column corresponding to the force point

linha2 = pontos(2, :); % Get the second row of the matrix
[~, indices] = sort(linha2); % Sort the second row and obtain the sorting indices
pontos = pontos(:, indices); % Sort the matrix based on the indices from the second row

linha3 = pontos(3, :); % Get the third row of the matrix

% Sort groups of three columns in descending order based on the values in the third row
for i = 1:(size(pontos, 2) - 1) / 3
    index = 3 * i; % Calculate the starting index of each group
    cols = [index - 2 index - 1 index]; % Columns corresponding to the group
    values = linha3(cols); % Values in the third row corresponding to the group
    [~, indices] = sort(values, 'descend'); % Sort the values in descending order
                                            %and obtain the sorting indices
    indices = indices + index - 3; % Adjust the indices to match the correct columns
    pontos(:, cols) = pontos(:, indices); % Update the matrix with the sorted columns
end

a=0;
matriz=zeros(2,70,numero_freq_proprias_exp); % Initialize a 3D matrix

% Read data from the file and populate the matrix
for i=1:numero_freq_proprias_exp
    t=0;
    Cond=true;
    while Cond==true
        a=a+1;
        t=t+1;
        aline=fgetl(file_2);
        if mod(a,2)~= 0 && strcmpi(aline(1:3), 'END')==false
            linha=regexp(aline, '\S ' ,'split');
            numeros = 0; % Initialize a vector to store numbers
            for r = 1:numel(linha)
                str = strtrim(linha{r}); % Remove whitespace from the element
                if ~isempty(str) % Check if the element is not empty
                    numeros(r) = str2double(str); % Convert the element to a number
                                                  %and store it in the 'numeros' vector
                end
```

```
            end
            if length(numeros)== comp_linha_file_ex
                matriz(2,t/2,i)=numeros(comp_linha_file_ex); % Store the number in the
                                                             %second row of the corresponding column
            elseif length(numeros)== 1
                matriz(1,(t+1)/2,i)=numeros(1); % Store the number in the first
                                                %row of the corresponding column
            end
        elseif mod(a,2)== 0 && strcmpi(aline(1:3), 'END')==false
            linha=regexp(aline, '\S ' ,'split');
            numeros = 0; % Initialize a vector to store numbers
            for r = 1:numel(linha)
                str = strtrim(linha{r}); % Remove whitespace from the element
                if ~isempty(str) % Check if the element is not empty
                    numeros(r) = str2double(str); % Convert the element to a number
                                                  % and store it in the 'numeros' vector
                end
            end
            if length(numeros)== comp_linha_file_ex
                matriz(2,t/2,i)=numeros(comp_linha_file_ex); % Store the number in the
                                                             % second row of the corresponding column
            elseif length(numeros)== 1
                matriz(1,(t+1)/2,i)=numeros(1); % Store the number in the first row of the
                                                % corresponding column
            end
        else
            Cond = false; % Exit the loop if 'END' is encountered
        end
    end
end

coluna_70 = find(matriz(1,:,1) == 70); % Find the column index where the value 70 is
                                       % in the first matrix
matriz(:,coluna_70,:) = []; % Remove the column with index 'coluna_70' from all matrices

% Sort the first rows of each 2D matrix in ascending order
for i = 1:size(matriz, 3)
    [~, order] = sort(matriz(1,:,i)); % Get the order of the elements in the first row
    matriz(:,:,i) = matriz(:,order,i); % Reorder the columns based on the order of the first row
end


% Get the values from the first row of the 'pontos' matrix
linha1 = pontos(1, :);

% Create a copy of the 'matriz' matrix
matriz_ordenada = matriz;

% Sort the two-dimensional matrices based on the values in the first row of 'pontos'
```

```
for i = 1:size(matriz, 3)
    matriz_ordenada(:, :, i) = matriz(:, linha1, i);
end

% Replace the original 'matriz' with the sorted 'matriz_ordenada'
matriz = matriz_ordenada;

a=0;
matriz_nume=zeros(3,69,numero_freq_proprias_num); % Initialize a 3D matrix

% Read data from the file and populate the matrix
for i=1:numero_freq_proprias_num
    Cond=true;
    t=0;
    while Cond==true
        a=a+1;
        t=t+1;
        aline=fgetl(file_3);
        if strcmpi(aline(1:3), 'END')==false
            linha=regexp(aline, '\S ' ,'split');
            numeros = 0; % Initialize a vector to store numbers
            for r = 1:numel(linha)
                str = strtrim(linha{r}); % Remove whitespace from the element
                if ~isempty(str) % Check if the element is not empty
                    numeros(r) = str2double(str); % Convert the element to a number and
                                                  % store it in the 'numeros' vector
                end
            end
            matriz_nume(1,t,i)=numeros(2);
            matriz_nume(2,t,i)=numeros(3);
            matriz_nume(3,t,i)=numeros(4);
        else
            Cond = false; % Exit the loop if 'END' is encountered
        end
    end
end

for b=1:numero_freq_proprias_num

    linha2_num = matriz_nume(2, :,b); % Get the third row of the matrix of each normal vector

    % Sort groups of three columns in descending order based on the values in the third row
    for i = 1:(size(matriz_nume, 2)) / 3
        index = 3 * i; % Calculate the starting index of each group
        cols = [index - 2 index - 1 index]; % Columns corresponding to the group
        values = linha2_num(cols); % Values in the third row corresponding to the group
        [~, indices] = sort(values, 'descend'); % Sort the values in descending order and
                                               % obtain the sorting indices
        indices = indices + index - 3; % Adjust the indices to match the correct columns
```

```
        matriz_nume(:, cols,b) = matriz_nume(:, indices,b); % Update the matrix with the
                                                            % sorted columns
    end
end

MAC_matrix = calculateMACMatrix(matriz_nume, matriz, title_1);

fclose(file_1); % Close the file 'file_1'
fclose(file_2); % Close the file 'file_2'
fclose(file_3); % Close the file 'file_3'

function MAC_matrix = calculateMACMatrix(matrix1, matrix2, title_1)
    % Check the number of matrices in the third dimension
    n = size(matrix1, 3);
    m = size(matrix2, 3);

    % Initialize the MAC matrix
    MAC_matrix = zeros(n, m);

    % Iterate over all combinations of matrices
    for i = 1:n
        for j = 1:m
            % Get the vectors corresponding to the second row of the matrices
            vector1 = matrix1(3, :, i)';
            vector2 = matrix2(2, :, j)';

            % Check if the sizes of the vectors allow MAC calculation
            if numel(vector1) > 1 && numel(vector2) > 1
                % Normalize the vectors relative to the maximum absolute value
                vector1 = vector1 / max(abs(vector1));
                vector2 = vector2 / max(abs(vector2));

                % Calculate the MAC between the vectors
                MAC_matrix(i, j) = calculateMAC(vector1, vector2);
            end
        end
    end

    % Generate the three-dimensional bar graph with colors
    figure(1)

    % Create a 3D bar graph using the MAC_matrix data
    barMAC = bar3(MAC_matrix);

    % Iterate over each bar in the bar graph
    for k = 1:length(barMAC)
        % Get the ZData (heights) of the current bar
        zdata = barMAC(k).ZData;

```

```
        % Set the color data of the current bar to its ZData
        barMAC(k).CData = zdata;

        % Set the face color of the current bar to interpolated colors based on the ZData
        barMAC(k).FaceColor = 'interp';
    end

    % Set the colormap to 'jet', which maps values to a range of colors
    colormap(jet);

    % Add a colorbar to the figure to represent the mapping of colors
    colorbar;

    % Set the y-axis label
    ylabel('Numerical modes','fontsize',15);

    % Set the x-axis label
    xlabel('Experimental modes','fontsize',15);

    % Set the title of the figure
    title(title_1);%

    % Display a box around the plot
    box on
end

function MAC = calculateMAC(vector1, vector2)
    % Normalize the input vectors relative to the maximum absolute value
    vector1 = vector1 / max(abs(vector1));
    vector2 = vector2 / max(abs(vector2));

    % Calculate the Modal Assurance Criterion (MAC)
    MAC = abs(vector1' * vector2)^2 / ( (vector1' * vector1) * (vector2' * vector2) );
end
```